International Journal Of
Industrial Electronics Control and Optimization
Print ISSN: 3517-2645
Online ISSN: 3568-2645
Homepage: https://ieco.usb.ac.ir/

About Journal

The University of Sistan and Baluchestan entered into strategic partnership with Iranian Association of Electrical and Electronic Engineers (IAEEE) to publish the **International Journal of Industrial Electronics Control and Optimization (IECO)**. The IECO is a refereed international journal which presents to the international scientific community important results of work in these fields, whether in the form of modeling simulation, analysis, fundamental research, development, application, design or real-time implementation. The scope of IECO is broad, encompassing all aspects of Industrial Electronics, Control and Optimization.

Note: International Journal of Industrial Electronics, Control and Optimization (IECO) has qualified to **ACADEMIC RESEARCH JOURNAL (ELMI-PAJOHESHI)** status certified by the ministry of Science, Research and Technology of Iran (No. 231566/3/18 dated 1396/10/09), and is published by the University of Sistan and Baluchestan through a formal partnership (No. 952/2/1500 dated 1395/11/04) with Iranian Association of Electrical and electronic Engineers (IAEEE) in order to develop scientific and research cooperation. **Aims and Scope**

International Journal of Industrial Electronics, Control and Optimization (IECO) is a Peer reviewed journal of advanced and state-of-the-art in the science and engineering of Industrial Electronics, Control and Optimization. Its Scope encompasses the applications of Industrial Electronics, power systems, control, optimization and computational intelligence for the enhancement of industrial and manufacturing system and processes. The scope of the journal include the following:

I. Industrial Electronics

- *Low and high power converters*
- *Renewable energy*
- *Drive control techniques*
- *Techniques for advanced power semiconductor devices*
- *Power quality and utility applications*
- *Communications*
- *Flexible AC Transmission Systems (FACTS)*
- *Control in power electronics*
- *Electromagnetic and thermal performance of electronic power converters*
- *Motion control, robotics, sensors and actuators*
- *Fault detection and diagnosis*
- *Power systems*
- *Factory automation, communication, and computer networks*

II. Control

- *Adaptive control*
- *Control of process systems*
- *Control theory*
- *Data processing*
- *Design of control systems*
- *Hybrid systems*
- *Identification and observation*
- *Intelligent systems*
- *Model-predictive control*
- *Optimal control*
- *Robust control*
- *Fractional order systems*

III. Optimization

- *Ant Colony*
- *Chaos Theory*
- *Evolutionary Computing*
- *Fuzzy Computing*
- *Hybrid Methods*
- *Immunological Computing*
- *Neuro Computing*
- *Particle Swarm*
- *Probabilistic Computing*
- *Rough Sets*
- *Wavelet*

International Journal Of
Industrial Electronics Control and Optimization
Print ISSN: 3517-2645
Online ISSN: 3568-2645
Homepage: https://ieco.usb.ac.ir/

High Impedance Fault Detection in Power Transmission Lines Using Hilbert Transform and Instantaneous Frequency

Hassan Abniki[1, 2] | Mostafa Hajati Samsi[3] | Behrooz Taheri[4] | Seyed Amir Hosseini[5]

Deputy Director General of the Office of Research and Technology Development, Tavanir Co., Tehran, Iran.[1]
ECE School, University of Tehran, Tehran, Iran.[2]
Department of Electrical Engineering, Vebko Amirkabir research and development Co., Tehran, Iran.[3]
Department of Electrical Engineering, Qazvin Branch, Islamic Azad University, Qazvin, Iran.[4]
Electrical and Computer Engineering Group, Golpayegan College of Engineering, Isfahan University of Technology, Golpayegan, Iran.[5]
Corresponding author's email: s.hosseini@iut.ac.ir

Article Info

Article type:
Research Article

Article history:
Received: 2022 July 06
Received in revised form: 2022 Nov 26
Accepted: 2022 Dec 05
Published online: 2023 Jan 22

Keywords:
High Impedance Fault,
Power System Protection,
Power Transmission Lines,
Hilbert Transform.

ABSTRACT

Power transmission lines are vital components of today's power systems. These power lines transmit the electricity produced in power plants in high volume and with very low losses to distant areas so that it can be reached consumers through distribution networks. In fact, these lines are the intermediary between major energy producers and distribution networks. Accordingly, these transmission lines are of great importance and must be protected appropriately with a suitable protection system. Distance relays are widely used to protect these lines due to their convenient coordination characteristics and simplicity. High impedance faults (HIFs) can be a critical challenge for distance relays due to their low current amplitude and similarity to conventional events in power systems, such as capacitive bank switching. Therefore, this paper presents a new approach based on the instantaneous frequency variations obtained from the current RMS to detect HIFs. This method detects HIFs by calculating a detection index (DI) and considering a threshold value. The proposed method was tested using DIgSILENT and MATLAB software in an IEEE standard 39-bus network. The presented results evidently demonstrate that the proposed method is suitable for detecting HIF and low impedance faults (LIFs). In addition, this method has a proper performance during capacitor bank switching and can well distinguish between HIFs and capacitive bank switching. Moreover, the presented method is resistant to noise and is also capable of detecting the faulty phase.

I. Introduction

A. Motivation

Due to random nature and environmental conditions, the probability of fault that occurs is very high in power systems [1]. Therefore, power systems require a proper protection system. An ideal protection system that can operate accurately and timely can reduce damage to network equipment and even humans [2]. Among the various protection designs and relays, distance relays are an integral part of power system protection. Some desirable features of distance relays include simplicity, use of local voltage and current for fault detection, and fault locating capability [3]. Such characteristics have made distance relays a very beneficial means for power transmission line protection. Nevertheless, despite their numerous advantages, these relays also suffer from some shortcomings. One of the problems associated with distance relay algorithms is malfunctioning during high impedance faults (HIFs). Low current values and electric arcs distort the current during HIF. Besides, the current is very asymmetric and unstable during

HIF. In addition, the transient states of this type of fault are very similar to load switching and capacitive bank switching [4]. Failure to detect HIFs promptly may cause severe damage to network equipment and humans [5, 6].

B. Literature review

Despite the importance of HIF detection in power transmission lines, most research in this field has focused on distribution systems in recent years. Although the main purpose of this paper is to detect HIFs on power transmission lines, HIF detection methods in distribution networks have also been explored to have a more thorough evaluation.

Reference [1] employs discrete wavelet transform (DWT) and root mean square (RMS) values to identify and classify HIFs. Methods that use DWT require a high sampling rate for detection. In addition, this reference does not implement its method during signal noise [7]. In reference [8], the time-domain of current waveforms is only analyzed using the Kullback-Leibler divergence similarity measure. Authors in this reference use a time-based criterion to correctly identify HIFs. Reference [9] uses time domain analysis to detect HIF. Reference [10] uses a transient switching method to detect HIFs. Although the performance of this method is suitable, it cannot detect the faulty phase. References [11, 12] use a combination of DWT, fuzzy logic, and artificial neural networks (ANN) to detect HIFs. Although intelligent methods are accurate, they must be trained with a variety of simulations. In addition, these methods may be sensitive to noise. Reference [13] presents an HIF detection scheme based on empirical mode decomposition (EMD) in a DC microgrid. Reference [14] presents a method based on changes in active and reactive power components for HIF detection in DC microgrids.

This method may also respond differently in different networks. Reference [15] presents a method based on measuring the current at both ends of the transmission line and using differential protection. The main shortcoming of this method is its dependency on telecommunication platforms. Implementing telecommunication links will increase the fault detection time due to inheritance delay. Reference [16] uses correlation functions for fault detection. Mathematical morphology is used to identify HIFs in references [17, 18]. To implement such methods, relays suffer from heavy calculations. Reference [19] uses traveling waves to locate HIF. These methods require special equipment that increases the cost of implementing the protection system. In addition, in some studies on power swing detection, such as references [20-22], the ability to detect HIF has been investigated as a case. In these studies, an appropriate HIF model is not implemented. In addition, these studies can only detect faults with impedances below 150 ohms. Studies on HIF diagnosis can be categorized from different perspectives, including method, sampling rate, sampling method, solution method, and so on. Table (1) presents some recent studies on HIF diagnosis and their differences from the present article.

C. Contributions and organization

As mentioned, HIF detection in power systems is an issue of great importance. Besides, speed and accuracy in HIF detection are also crucial. Reference [27] uses instantaneous frequency to detect power swings. This algorithm can detect a variety of faults in power systems with appropriate speed and accuracy at a sampling rate of 10 kHz. Although this article considers HIF as a case and HIF in the power system may have an impedance of more than 1000 [28], the approach presented in this paper cannot detect HIFs with values greater than 100 ohms. In addition, as the transmission lines get longer, this method may face some challenges to detect HIFs that have occurred at a very long distance from the relay. The main objective of this article is to modify the algorithm presented in reference [27] to improve its performance in the event of an HIF. Besides being resistant to noise and not malfunctioning during capacitive bank and load switching, the proposed new algorithm still enjoys a good fault detection speed. The modified algorithm can also detect the faulty phase.

This article is organized as follows. Section II formulates the problem. The simulation results are presented in Section II. Section IV compares the proposed method with similar research. Finally, the conclusion is presented in Section V.

II. Proposed method

To modify the algorithm presented in reference [27], the method of obtaining instantaneous frequency using the Hilbert transform should be investigated. For this purpose, this section describes the required relationships and the modified algorithm.

A. Hilbert Transform and instantaneous frequency

One of the most critical data in monitoring, protecting, and controlling power systems is frequency. Calculating the exact value of frequency for programs that are dependent on a quick response is an issue of great importance [29]. The conventional definition for instantaneous frequency (IF) is that IF is typically associated with the rate of change in phase angle. In this paper, IF is obtained using the Hilbert transform. Hilbert's transformation was first proposed by David Hilbert to characterize integral equations in physics and mathematics [30]. The Hilbert transform can be defined for a function as (1) [31-33].

$$H[X(t)] = \tilde{x}(t) = \pi^{-1} \int_{-\infty}^{+\infty} \frac{x(\tau)}{t-\tau} d\tau \quad (1)$$

The Hilbert transform is a mathematical transformation function that shifts the phase of a signal by 90 degrees without changing the amplitude of the signal. In fact, in the Hilbert transformation, the phase of positive frequency components is shifted by $+\ \pi/2$ and the phase of negative frequency components is shifted by $-\ \pi/2$. The Hilbert transform is an odd function and an even function.

TABLE I
RECENT STUDIES ON HIF DIAGNOSIS

Ref.	Year	Method	Voltage	Detection / location	Requirement for a telecommunication link	Dependence on network parameters	Consideration of noise	Consideration of load switching	Consideration of capacitor bank switching	Faulty phase detection
[2]	2021	Impedance-based	HV	location	✓	✓	✓	×	×	✓
[23]	2021	Robust faulted phase	UHV	Detection	×	×	×	×	×	×
[24]	2021	Power spectral density	LV	Detection	×	×	✓	✓	✓	×
[25]	2020	Wavelet Transform	HV	Detection	×	×	×	×	×	×
[26]	2020	Wavelet transform	LV	Detection	×	×	✓	✓	✓	×
This paper	-	instantaneous frequency	HV	Detection	×	×	✓	✓	✓	✓

For the Hilbert transform, it is enough to obtain the Fourier transform of the function and multiply it with the $j.\text{sgn}(f)$ function in the Fourier domain. Subsequently, the inverse Fourier transform of the function is calculated. The resulting function is the Hilbert transform. $j.\text{sgn}(f)$ is the transfer function in the Hilbert transform (in (2)).

$$H(jw) = -j.\text{sgn}(w) \tag{2}$$

$$\text{sgn}(w) = \begin{cases} 1 & \text{w}>0 \\ 0 & \text{w}=0 \\ -1 & \text{w}<0 \end{cases} \tag{3}$$

The Hilbert transform is a linear operator, which consists of an input signal $f(r)$ and an output signal $f_1(r)$. If the frequency spectrum of an input and output signal were $f(w)$ and $f_1(w)$, respectively, the relationship between the frequency spectrum of the input and output signals would be similar to (4).

$$\begin{cases} F_1(w) = H(jw).F(w) \\ F_1(w) = -jF(w) \quad \text{for} \quad \text{w} \geq 0, \\ F_1(w) = -jF(w) \quad \text{for} \quad \text{w}<0 \end{cases} \tag{4}$$

In the space domain, the relationship between the input and output signals is expressed as a $g(r)$ composite function. $g(r)$ is an analytic function whose imaginary part is equal to the Hilbert transform of its real part.

$$g(r) = f(r) + jf_1(r), r = x + jz, \tag{5}$$

in which the Hilbert transform between the input and output signal in the space domain is defined as the mixture of the function in the input signal.

$$h(x) = F^{-1}(-j.\text{sgn}(w)), \tag{6}$$

$$h(x) = \frac{1}{\pi x}, \tag{7}$$

$$f_1(r) = h(x) * f(r), \tag{8}$$

$$f_1(r) = \frac{1}{\pi}\int_{-\infty}^{\infty} \frac{f(\theta)}{x-\theta} dv \tag{9}$$

Also, the phase angle can be achieved from (10) by the Hilbert transform.

$$z(t) = x(t) + jy(t) \tag{10}$$

where $z(t)$ is a function of time with instantaneous magnitude. The values of $a(t)$ and $\theta(t)$ can also be achieved using (11) and (12).

$$a(t) = \sqrt{x^2(t) + y^2(t)} \tag{11}$$

$$\theta(t) = \arctan\left(\frac{y(t)}{x(t)}\right) \tag{12}$$

Although the definition provided is the most conventional and basic definition for IF, there are also other definitions. The IF obtained using the analytical signal and the Hilbert conversion provides a meaningful physical concept of the signal, which is the phase angle change rate.

$$\omega(t) = \frac{d\theta}{dt} \tag{13}$$

Equation (14) is used to obtain IF after applying the Hilbert conversion to the input signal [27].

$$F = \frac{F_S}{2\pi} \times diff\left(angle\left(\bar{X}(t)\right)\right) \tag{14}$$

B. HIF detection algorithm

In the first stage, the algorithm samples the current signal and forms a signal window according to (15) [34].

$$\text{window length} = \frac{F_S}{F} \tag{15}$$

where F_S is the sampling frequency and is equal to 10 kHz and F is the base frequency of the power system which is considered to be 60 Hz. It should be noted that since the proposed algorithm can detect the faulty phase, the sampling and all the steps described below are separately executed in all three phases. In the next step, by obtaining samples from the main current signal, the effective value of available data will be calculated using (16) [35].

$$I_{rms} = \sqrt{\frac{\sum_{k=1}^{N} I_k^2}{N}} \quad (16)$$

Subsequently, according to the items mentioned in Section (II-A), IF is calculated along the signal window. After calculating the Hilbert transform and IF, a detection index (DI) should be calculated to detect the fault. Moving window averaging (MWA) is used to calculate the DI value. MWA is a low-pass filter applied to power system protection that is used for fault detection, fault direction detection, and faulty phase identification. This technique is less sensitive to noise in the signal. In MWA, the time domain of the continuous signal $x(t)$, for the T_0 length of the window is written as (17) [36].

$$\bar{x}(t) = \frac{1}{T_0} \int_{t-T_0}^{t} x(t)dt \quad (17)$$

The frequency response of the filter is the Fourier transform of the impulse response.

$$\bar{X}(j\omega) = e^{\frac{-j\omega T_0}{2}} \sin c\left(\frac{\omega T_0}{2}\right) \quad (18)$$

where $\sin c(\theta) = \sin(\theta)/\theta$.

Equation (19) indicates how to calculate DI.

$$\bar{X}(j\omega) = e^{\frac{-j\omega T_0}{2}} \sin c\left(\frac{\omega T_0}{2}\right) \quad (19)$$

The fault detection condition can be written based on (20).

$$DI > K \Rightarrow \text{HIF is detected} \quad (20)$$

where K is the threshold value obtained using various computer simulations. It is assumed to be 1.5 in this paper. The threshold value detection method used in this paper has already been discussed in references [3, 34].

With respect to the items expressed, the algorithm of the proposed method is provided in Fig. 1.

III. Simulation results

To simulate and test the method presented in different modes, the power system studied is simulated in Digsilent software. After analyzing the network in different cases, information is transferred from Digsilent software to MATLAB software to analyze and implement the proposed method. The protection algorithm presented in the previous section is implemented in the MATLAB m file and the desired outputs are received.

A. The network study

To test the proposed approach, an IEEE 39-bus system is implemented in this article. This network is a complex network with 10 synchronous generators. The specifications have made it very suitable for dynamic studies and the protection of power systems. Fig. 2 shows a single-line diagram of this network. The protection relay is installed on bus 26 to protect lines 29-26. The length of the protected line is 247.9688 km. This line is also parallel to lines 26-28 and 28-29. The length of the line, as well as the effects of the parallel lines, has made it very suitable for testing the proposed method.

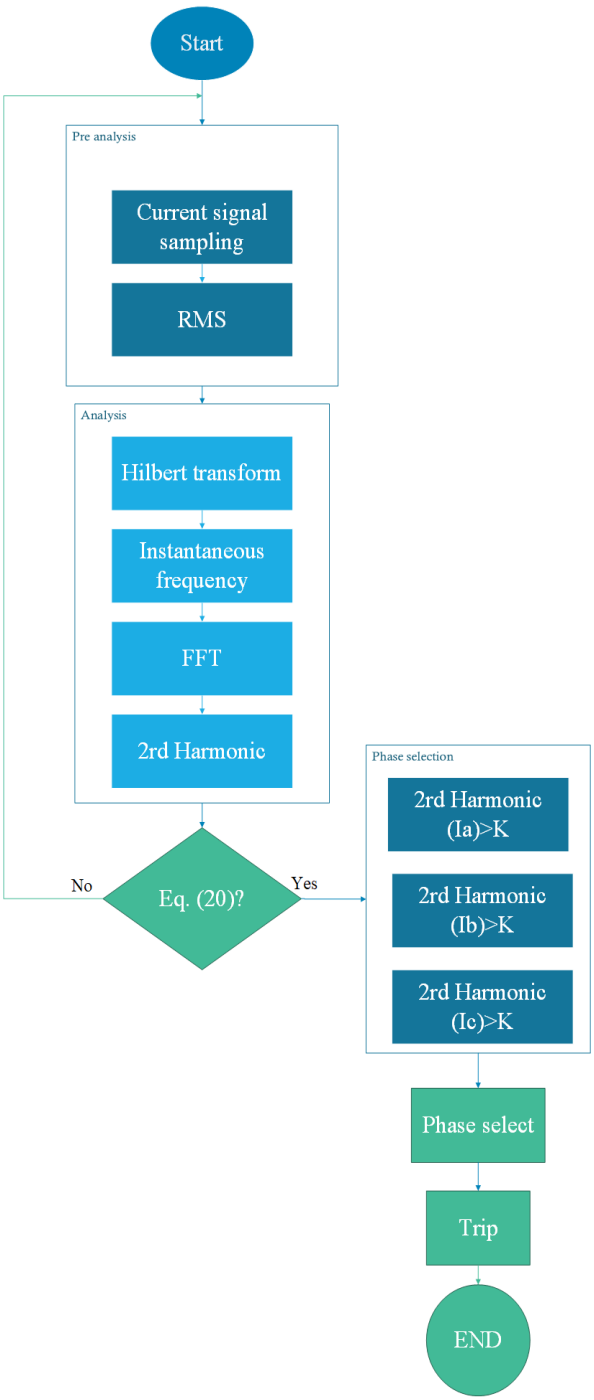

Fig. 1. The algorithm proposed for detecting HIF and determining the faulty phase.

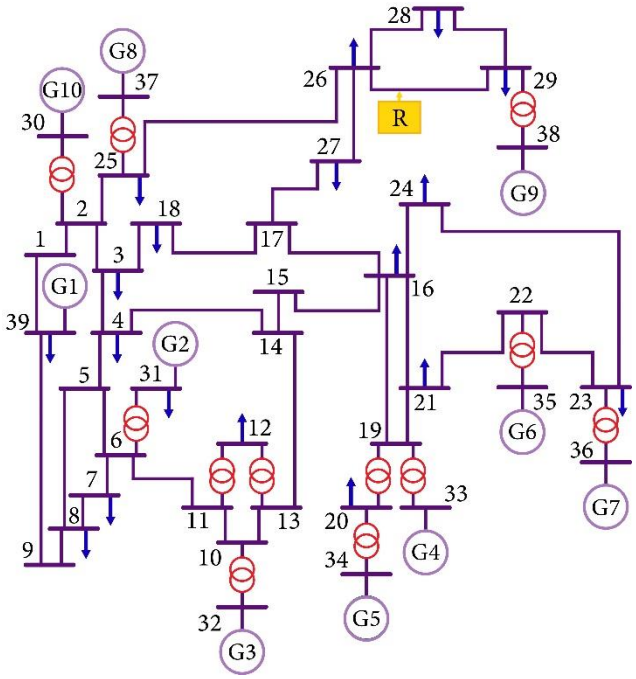

Fig. 2. The single-line diagram of the network.

B. *Case1: HIF detection*

Generally, power systems are exposed to various disturbances and anomalies that will highly affect their proper functioning. Among various faults, HIFs can be very challenging for power systems. During an HIF, the fault current is so limited; this amplitude can be very close to the capacitive bank switching current. Therefore, regular protection schemes cannot correctly detect this type of fault [37, 38]. For this reason, some other approaches are required to detect HIF and distinguish it from other regular power system events. The operation of the proposed method during HIF is described in this section and its performance during capacitive bank switching is presented in Section (III-D).

To evaluate the performance of the proposed method during a variety of HIFs, a single-phase HIF (the fault is applied to phase A) with R = 500 Ω and X = 50 Ω is first applied on 50% of the protected line. Fig. 3 shows the performance of the proposed method during this type of fault. According to this figure, after applying the fault, DI obtained in the final stage of the algorithm (Fig. 1) exceeded the threshold value, and the proposed algorithm sent the trip command within 9.72 ms. The algorithm also detected the faulty phase and sent the trip command only for phase A.

As mentioned earlier, HIF impedance may sometimes reach up to 1000 ohms. For this reason, an HIF with the same fault specifications and with the only difference that its fault impedance is 1000 ohms is implemented in the network. Fig. 4 shows the performance of the proposed algorithm during the HIF fault with R = 1000 Ω and X = 100 Ω. According to this figure, the algorithm could detect the fault in about 8 ms. The algorithm also detected the faulty phase, and the trip command was sent only to phase A.

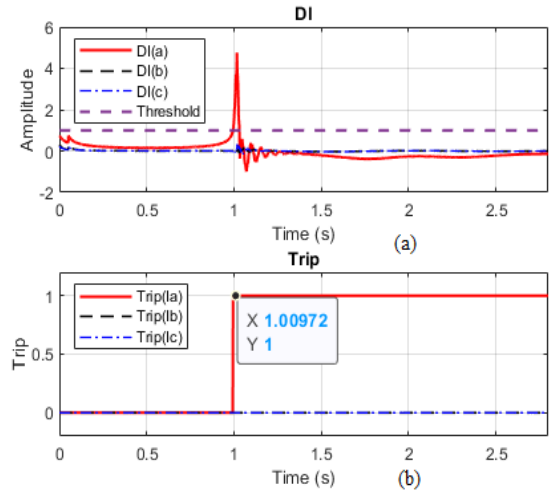

Fig. 3. Performance of the proposed method during a single-phase HIF fault with R = 500 Ω and X = 50 Ω, a) DI, b) Trip signal.

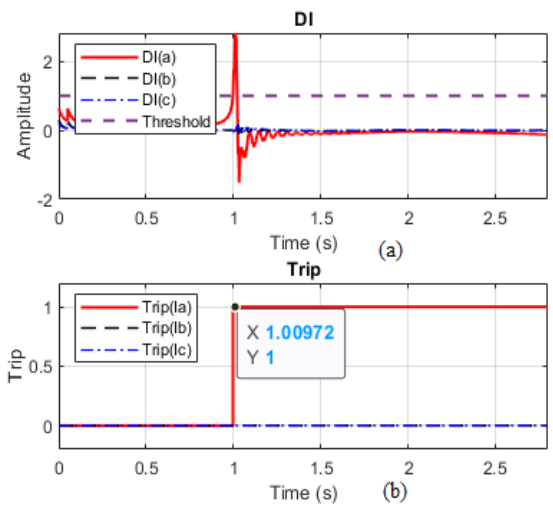

Fig. 4. Performance of the proposed method during a single-phase HIF with R = 1000 Ω and X = 100 Ω, a) DI, b) Trip signal.

As mentioned, the proposed algorithm can detect different HIF types. To validate this issue, a three-phase HIF with R = 500 Ω and X = 50 Ω was applied to the protected line in 1.5 s (Fig. 5). In another case, to investigate a fault with 1000 ohm impedance, a three-phase HIF with R = 1000 Ω and X = 100 Ω was applied to the protected line (Fig. 6). Evidently, the proposed method could detect the three-phase HIF. As can be seen, at this stage, the trip signal was sent to all three phases. According to Fig. 5, the trip command was sent within 11.9 ms, but in the three-phase HIF case with R = 1000 ohm and X = 100 ohms, the trip time was increased to 11.9 ms. Although the detection time of the algorithm was increased in this case, the detection time was still appropriate.

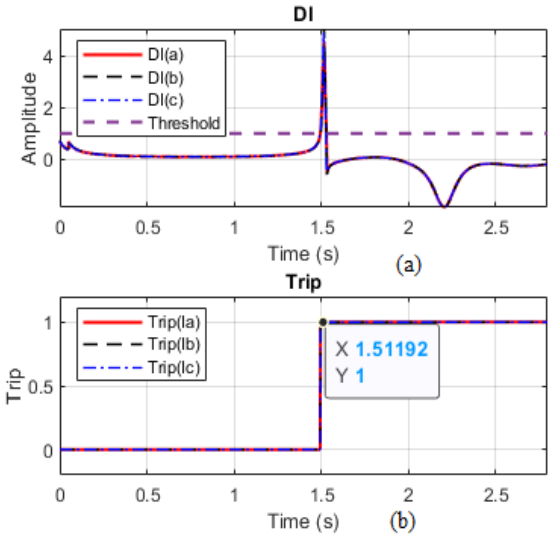

Fig. 5. Performance of the proposed method at the time of a three-phase HIF fault with R = 500 Ω and X = 50 Ω, a) DI, b) Trip signal.

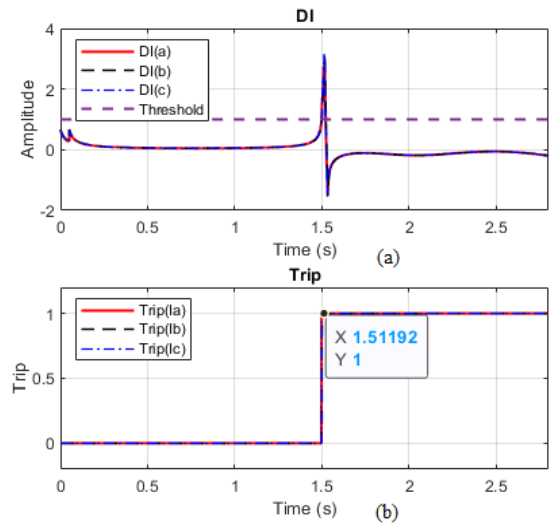

Fig. 6. Performance of the proposed method at the time of a three-phase HIF fault with R = 1000 Ω and X = 100 Ω, a) DI, b) Trip signal.

Figure 7 shows the performance of the proposed algorithm during various types of fault impedance angles. As it is clear from this figure, by changing the fault impedance angle, the performance of the proposed method has been appropriate.

A reverse fault current condition will occur when a fault occurs on one of the lines adjacent to the protected line. It should be mentioned that the presented method should only detect faults on the protected line and not other lines (detection of faults on adjacent lines may cause malfunction of the protection coordination, cascading outage of the transmission lines and even the network blackout). To further analyze this issue, a high impedance fault with R=500 Ω and X=50 Ω is placed on 50% of line 26-27. This causes the protection relay of line 26-29 to see a reverse current. Figure 8 shows the result of this test. As it is clear from this figure, since the fault is in the adjacent line, the relay did not operate. In fact, it can be said that the presented method works in a directional manner, which is considered as a positive feature for distance relays.

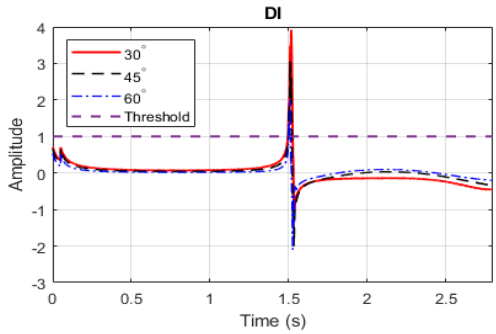

Fig. 7. The performance of the proposed method during different angles of fault impedance.

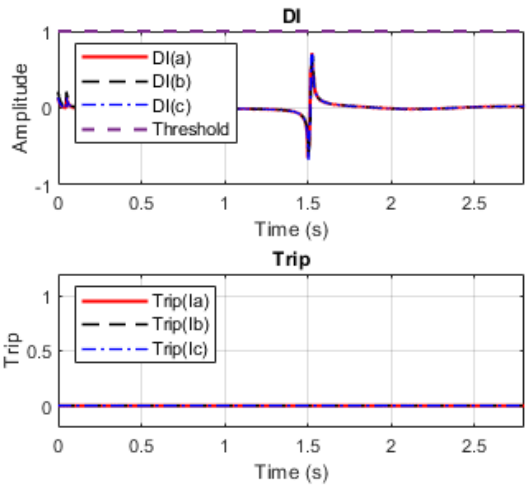

Fig. 8. Performance of the proposed method during a fault in adjacent lines

The impedance of a fault measured in the distance relay may become negative (i.e., a capacitator fault) in the compensated serial lines. Therefore, fault detection methods must be able to identify this type of fault, which was analyzed in this section. The fault was applied to 50% of the protected line at 1 s with different impedance angles. Figure 9 reports the test results. Accordingly, DI exceeded the threshold in all four cases, and the fault was detected correctly.

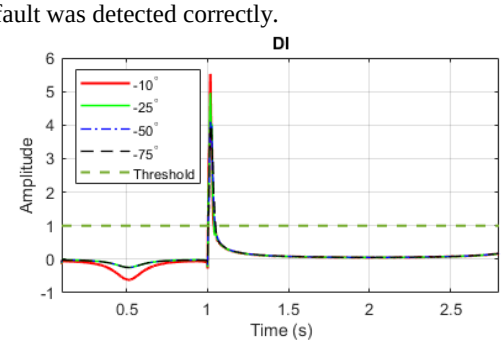

Fig. 9. The performance of the proposed method during different negative angles of fault impedance.

Fault angles can also affect the performance of HIF detection methods to some extent. For this reason, the effect of fault types and fault angles was also investigated. The results of this study are presented in Table 2. According to this table, the proposed method has a good performance for fault angles of 0, 30, and 90 degrees for different types of faults.

TABLE 2
PERFORMANCE OF THE PRESENTED METHOD IN DIFFERENT ANGLES OF HIF.

Fault type	Impedance	Fault angle	Detection time (ms)
A-G	R=100 Ω, X=10 Ω	0	9.7
	R=100 Ω, X=10 Ω	30	9.8
	R=100 Ω, X=10 Ω	90	9.7
B-G	R=200 Ω, X=20 Ω	0	9.7
	R=200 Ω, X=20 Ω	30	9.7
	R=200 Ω, X=20 Ω	90	9.9
C-G	R=300 Ω, X=30 Ω	0	9.7
	R=300 Ω, X=30 Ω	30	9.8
	R=300 Ω, X=30 Ω	90	9.7
A-B-G	R=400 Ω, X=40 Ω	0	11.9
	R=400 Ω, X=40 Ω	30	11.9
	R=400 Ω, X=40 Ω	90	11.9
A-C-G	R=500 Ω, X=50 Ω	0	11.7
	R=500 Ω, X=50 Ω	30	11.9
	R=500 Ω, X=50 Ω	90	11.9
B-C-G	R=1000 Ω, X=100 Ω	0	11.9
	R=1000 Ω, X=100 Ω	30	11.8
	R=1000 Ω, X=100 Ω	90	11.9
A-B-C	R=1000 Ω, X=100 Ω	0	11.9
	R=1000 Ω, X=100 Ω	30	11.8
	R=1000 Ω, X=100 Ω	90	11.9

C. *Case 2: LIF detection*

As was previously observed, the proposed algorithm can properly detect HIF. But to have a comprehensive protection algorithm, it should be able to detect low impedance fault (LIF) as well. To evaluate the performance of the proposed method in the LIF situation, a single-phase fault and a three-phase fault were applied to the protected line after 1.5 s. Figs. 10 and 11 illustrate the test results of the method provided during LIF faults. Obviously, the proposed algorithm correctly detected LIF. The only shortcoming of this algorithm is the lack of faulty phase detection and therefore the trip command was sent for all three phases (Fig. 10). Tackling this problem can be a suitable topic for further studies in this field.

As mentioned before, fault angle variations can significantly affect fault detection algorithms. Thus, the effects of different types of LIF and fault angles were also investigated. The results of this study are presented in Table 3 according to which the proposed method has a good performance for fault angles of 0, 30, and 90 degrees for different faults.

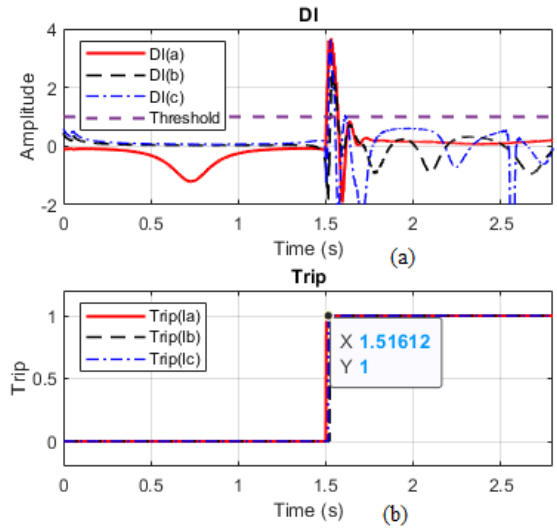

Fig. 10. Performance of the proposed method during a single-phase LIF, a) DI, b) Trip signal.

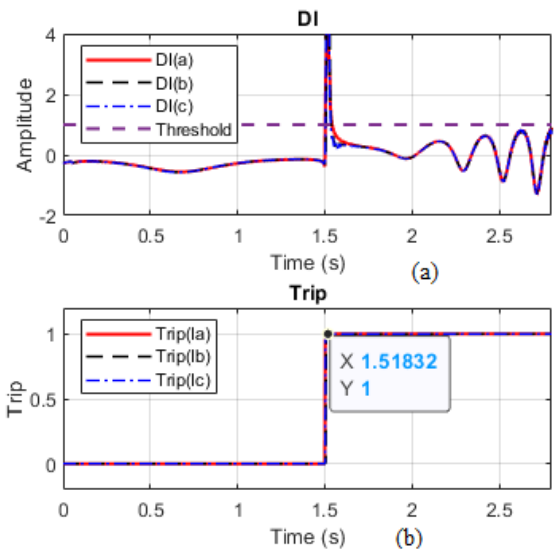

Fig. 11. Performance of the proposed method during a three-phase LIF, a) DI, b) Trip signal.

D. *Case 3: Capacitive bank switching*

As described earlier, current amplitude variations during HIF can be very similar to capacitive bank switching. For this reason, this section analyzes the performance of the proposed method during a capacitive bank switching. First, the performance of the proposed method during capacitive bank switching with RRP = 1 Mvar is investigated, and the results are illustrated in Fig. 12. The performance of the method during capacitive bank switching with RRP = 10 Mvar is also investigated and presented in Fig. 13. According to Figs. 12 and 10, during capacitive bank switching (1.5 seconds from the start of the simulation), the DI value has not exceeded the threshold value and the trip command is not issued. These two figures and the results obtained from previous tests prove that the proposed algorithm can appropriately distinguish between

capacitive bank switching, HIF, and LIF. Table 3 shows the performance of the presented method during all types of low-impedance faults. As it is clear from this table, the presented method has been able to quickly detect different types of low impedance faults.

TABLE 3
PERFORMANCE OF THE PRESENTED METHOD FOR DIFFERENT LIF ANGLES.

Fault type	Impedance	Fault angle	Detection time (ms)
A-G	R=0 Ω, X=0 Ω	0	16.1
	R=0 Ω, X=0 Ω	30	16.2
	R=0 Ω, X=0 Ω	90	16.1
B-G	R=0 Ω, X=0 Ω	0	16.1
	R=0 Ω, X=0 Ω	30	16.3
	R=0 Ω, X=0 Ω	90	16.1
C-G	R=0 Ω, X=0 Ω	0	16.2
	R=0 Ω, X=0 Ω	30	16.1
	R=0 Ω, X=0 Ω	90	16.1
A-B-G	R=0 Ω, X=0 Ω	0	18.2
	R=0 Ω, X=0 Ω	30	18.3
	R=0 Ω, X=0 Ω	90	18.4
A-C-G	R=0 Ω, X=0 Ω	0	18.3
	R=0 Ω, X=0 Ω	30	18.3
	R=0 Ω, X=0 Ω	90	18.1
B-C-G	R=0 Ω, X=0 Ω	0	18.3
	R=0 Ω, X=0 Ω	30	18.3
	R=0 Ω, X=0 Ω	90	18.3
A-B-C	R=0 Ω, X=0 Ω	0	18.2
	R=0 Ω, X=0 Ω	30	18.3
	R=0 Ω, X=0 Ω	90	18.3

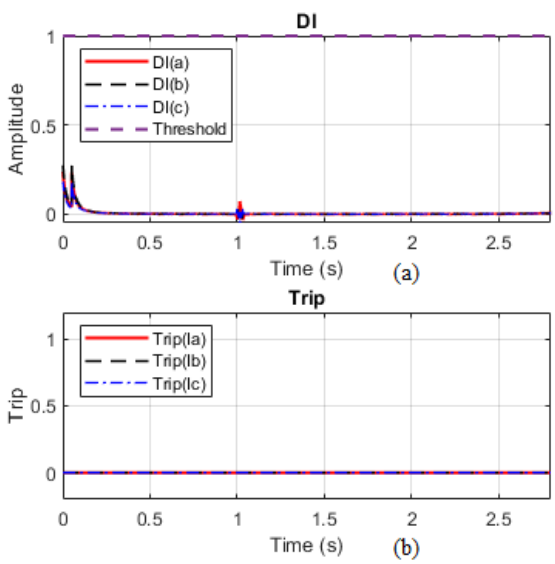

Fig. 12. Performance of the proposed method during capacitive bank switching with RRP = 1 MVar, a) DI, b) Trip signal.

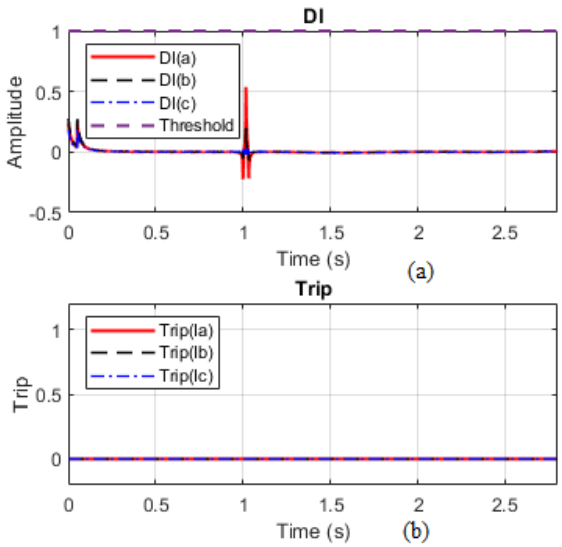

Fig. 13. Performance of the proposed method during capacitive bank switching with RRP = 10 MVar, a) DI, b) Trip signal.

E. Case 4: Noisy signal

In the real world, it is impossible to build a system without noise. Of course, it is possible to reduce the noise in the system by using solutions, but this noise will never reach zero. For this reason, it is best to design protection algorithms that are noise-resistant. White Gaussian noise is one of the types of noise that is widely used to investigate the effect of noise on protection algorithms [39]. White noise is generally referred to as a signal whose power is evenly distributed across all frequencies. White noise is inherently a Stochastic process. It is, therefore, a statistical model for signals and signal sources, not a specific signal. White Gaussian noise is any discrete signal at a time whose samples are a sequence of uncorrelated random variables with a mean of zero and finite variance. In this paper, white Gaussian noise with SNR = 10, 20, and 30 dB and Variance = 0.05 is used to test the proposed method. Figure 14 shows the performance of the method presented in different conditions when the signal is noisy. As it is clear from this figure, the proposed method has been able to detect different events simultaneously with noise.

F. Case 5: Wind turbine

To investigate the performance of the proposed method in a wind turbine case in an IEEE 39 bus network, two 500 and 400-MVA wind farms with a power factor of 0.8 are connected to bus 26 and two wind farms with similar specifications are connected to bus 29. The employed wind energy conversion system is a doubly-fed induction generator (DFIG). Subsequently, a three-phase fault with R=1000 Ω and X=100 Ω is placed in 50% of lines 26-29 in 1.5 seconds. Fig. 15 shows the test results of this fault in the network and in the presence of a wind turbine. As it is clear from this figure, the proposed method has been able to detect the high impedance fault in the presence of the wind turbine.

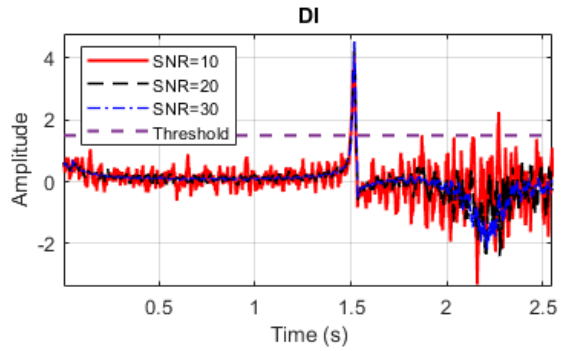

(a)

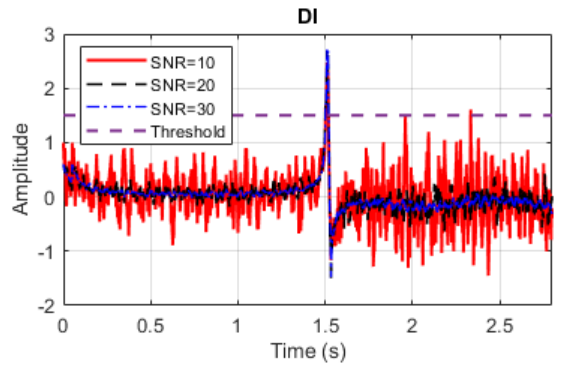

(b)

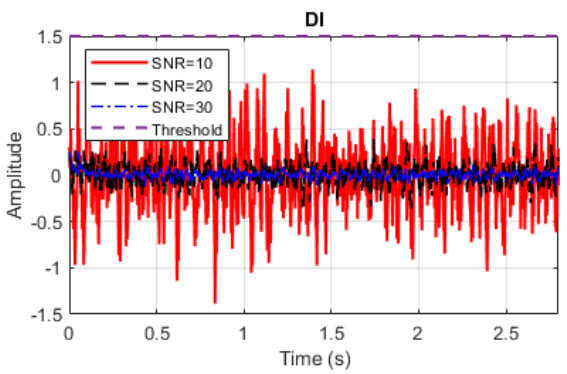

(c)

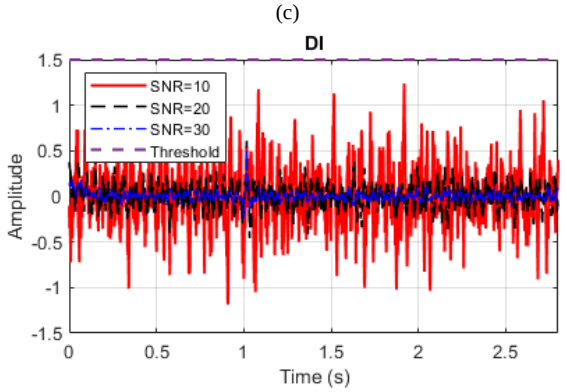

(d)

Fig. 14. Performance of the proposed method when the signal is noisy a) HIF with R = 500 Ω and X = 50 Ω b) HIF with R = 1000 Ω and X = 100 Ω c) capacitor bank switching with RRP = 1 Mvar d) capacitor bank switching with RRP = 10 Mvar.

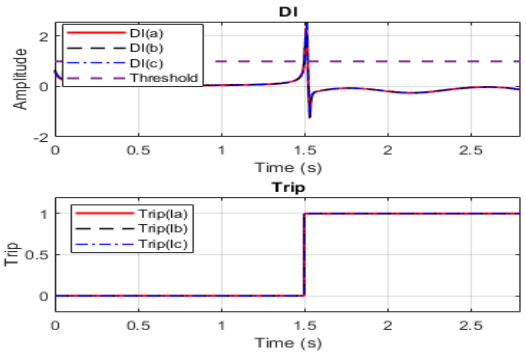

Fig. 15. The performance of the proposed method in the existence of a wind turbine in the studied network, a) DI, b) Trip signal.

G. *Case 6: Two-area network*

The single-line diagram of the two-area network is presented in Fig. 16. Accordingly, to protect line 1, the protection relay is connected to bus 7. To investigate the performance of this network during faults, a variety of HIFs are placed on 50% of line 1. The results of the HIF tests are presented in Table 4.

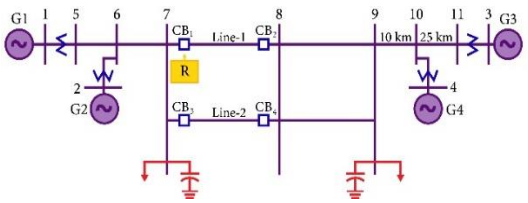

Fig. 16. The single-line diagram of the standard two-area network.

TABLE 4
PERFORMANCE OF THE PRESENTED METHOD IN DIFFERENT ANGLES OF HIF IN THE TWO-AREA NETWORK.

Fault type	Impedance	Fault angle	Detection time (ms)
A-G	R=100 Ω, X=10 Ω	0	9.8
	R=100 Ω, X=10 Ω	30	9.7
	R=100 Ω, X=10 Ω	90	9.8
B-G	R=200 Ω, X=20 Ω	0	9.7
	R=200 Ω, X=20 Ω	30	9.8
	R=200 Ω, X=20 Ω	90	9.7
C-G	R=300 Ω, X=30 Ω	0	9.7
	R=300 Ω, X=30 Ω	30	9.7
	R=300 Ω, X=30 Ω	90	9.8
A-B-G	R=400 Ω, X=40 Ω	0	12.1
	R=400 Ω, X=40 Ω	30	12.1
	R=400 Ω, X=40 Ω	90	12.2
A-C-G	R=500 Ω, X=50 Ω	0	12.1
	R=500 Ω, X=50 Ω	30	12.1
	R=500 Ω, X=50 Ω	90	122
B-C-G	R=1000 Ω, X=100 Ω	0	12.1
	R=1000 Ω, X=100 Ω	30	12.1
	R=1000 Ω, X=100 Ω	90	12.3
A-B-C	R=1000 Ω, X=100 Ω	0	12.1
	R=1000 Ω, X=100 Ω	30	12.3
	R=1000 Ω, X=100 Ω	90	12.1

IV. Conclusions

Faults are very likely to happen in power systems due to their accidental nature and environmental conditions. Therefore, power systems are in dire need of a proper protection system. A proper protection system with proper and timely operation can reduce damage to network equipment and even humans. Among the various protection designs and relays, distance relays are an integral part of the protection of power systems. These relays have desirable features such as simplicity, use of local voltage and current for fault detection, and fault locating capability. The distance relay features make it very suitable for protecting power transmission lines. But, despite the many advantages they provide, distance relays protection algorithms also have some shortcomings. For instance, they may malfunction during HIF.

For this reason, this paper presents a new method based on the Hilbert conversion and instantaneous frequency for HIF detection. The proposed method has been tested in an IEEE standard 39 bus network in different conditions of HIF, LIF, and capacitive bank switching. The results prove the applicability of the proposed method. Furthermore, the proposed method is resistant to white Gaussian noise and operates appropriately during signal noise.

REFERENCES

[1] J. Doria-Garcia, C. Orozco-Henao, L. Iurinic, and J. D. Pulgarín-Rivera, "High impedance fault location: Generalized exten-sion for ground faults," International Journal of Electrical Power & Energy Systems, vol. 114, p. 105387, 2020.

[2] J. Doria-García, C. Orozco-Henao, R. Leborgne, O. D. Montoya, and W. Gil-González, "High impedance fault modeling and location for transmission line," Electric Power Systems Research, vol. 196, p. 107202, 2021.

[3] B. Taheri, S. A. Hosseini, H. Askarian-Abyaneh, and F. Razavi, "Power swing detection and blocking of the third zone of distance relays by the combined use of empirical-mode decomposition and Hilbert transform," IET Generation, Transmission & Distribution, vol. 14, no. 6, pp. 1062-1076, 2019.

[4] S. Vlahinić, D. Franković, B. Juriša, and Z. Zbunjak, "Back up protection scheme for high impedance faults detection in transmission systems based on synchrophasor measurements," IEEE Transactions on Smart Grid, vol. 12, no. 2, pp. 1736-1746, 2020.

[5] B. Taheri and S. A. Hosseini, "Detection of High Impedance Fault in DC Microgrid Using Impedance Prediction Technique," in 2020 15th International Conference on Protection and Automation of Power Systems (IPAPS), 2020, pp. 68-73: IEEE.

[6] B. Taheri, S. A. Hosseini, S. Salehimehr, and F. Razavi, "A Novel Approach for Detection High Impedance Fault in DC Mi-crogrid," in 2019 International Power System Conference (PSC), 2020, pp. 287-292: IEEE.

[7] T. Lai, L. Snider, E. Lo, and D. Sutanto, "High-impedance fault detection using discrete wavelet transform and frequency range and RMS conversion," IEEE Transactions on Power Delivery, vol. 20, no. 1, pp. 397-407, 2005.

[8] S. Nezamzadeh-Ejieh and I. Sadeghkhani, "HIF detection in distribution networks based on Kullback–Leibler divergence," IET Generation, Transmission & Distribution, vol. 14, no. 1, pp. 29-36, 2020.

[9] R. Bhandia, J. de Jesus Chavez, M. Cvetković, and P. Palensky, "High impedance fault detection using advanced distortion detection technique," IEEE Transactions on Power Delivery, vol. 35, no. 6, pp. 2598-2611, 2020.

[10] W. Santos, F. Lopes, N. Brito, and B. Souza, "High-impedance fault identification on distribution networks," IEEE Transactions on Power Delivery, vol. 32, no. 1, pp. 23-32, 2016.

[11] M. S. Tonelli-Neto, J. G. M. Decanini, A. D. P. Lotufo, and C. R. Minussi, "Fuzzy based methodologies comparison for high-impedance fault diagnosis in radial distribution feeders," IET Generation, Transmission & Distribution, vol. 11, no. 6, pp. 1557-1565, 2017.

[12] I. Baqui, I. Zamora, J. Mazón, and G. Buigues, "High impedance fault detection methodology using wavelet transform and artificial neural networks," Electric Power Systems Research, vol. 81, no. 7, pp. 1325-1333, 2011.

[13] X. Wang et al., "High impedance fault detection method based on improved complete ensemble empirical mode decompo-sition for DC distribution network," International Journal of Electrical Power & Energy Systems, vol. 107, pp. 538-556, 2019.

[14] M. Faghihlou, B. Taheri, and S. Salehimehr, "High Impedance Fault Detection in DC Microgrid using Real and Imaginary Components of Power," in 2020 28th Iranian Conference on Electrical Engineering (ICEE), 2020.

[15] E. Sortomme, S. Venkata, and J. Mitra, "Microgrid protection using communication-assisted digital relays," IEEE Transac-tions on Power Delivery, vol. 25, no. 4, pp. 2789-2796, 2009.

[16] N. Faridnia, H. Samet, and B. D. Dezfuli, "A new approach to high impedance fault detection based on correlation func-tions," in IFIP International Conference on Artificial Intelligence Applications and Innovations, 2012, pp. 453-462: Springer.

[17] M. Kavi, Y. Mishra, and M. D. Vilathgamuwa, "High-impedance fault detection and classification in power system distribu-tion networks using morphological fault detector algorithm," IET Generation, Transmission & Distribution, vol. 12, no. 15, pp. 3699-3710, 2018.

[18] S. Gautam and S. M. Brahma, "Detection of high impedance fault in power distribution systems using mathematical mor-phology," IEEE Transactions on Power Systems, vol. 28, no. 2, pp. 1226-1234, 2012.

[19] H. Livani and C. Y. Evrenosoglu, "A machine learning and wavelet-based fault location method for hybrid transmission lines," IEEE Transactions on Smart Grid, vol. 5, no. 1, pp. 51-59, 2013.

[20] M. M. Ghalesefidi and N. Ghaffarzadeh, "A new phaselet-based method for detecting the power swing in order to prevent the malfunction of distance relays in transmission lines," Energy Systems, pp. 1-25, 2019.

[21] S. Salehimehr, B. Taheri, F. Razavi, M. Parpaei, and M. Faghihlou, "A new power swing detection method based on chaos theory," Electrical Engineering, pp. 1-19, 2019.

[22] B. Taheri and M. Sedighizadeh, "Detection of power swing and prevention of mal-operation of distance relay using com-pressed sensing theory," IET Generation, Transmission & Distribution, vol. 14, no. 23, pp. 5558-5570, 2020.

[23] R. F. Espinoza, O. Dias, M. C. Tavares, and Y. P. Molina, "Application of a robust faulted phase selector to high-

resistance and weak-infeed fault conditions on a 1000-kV UHV transmission line," Electric Power Systems Research, vol. 197, p. 107244, 2021.
[24] S. Roy and S. Debnath, "PSD based high impedance fault detection and classification in distribution system," Measure-ment, vol. 169, p. 108366, 2021.
[25] M. Paul and S. Debnath, "Wavelet based single Ended scheme for high impedance fault classification in transmission lines," in 2020 International Conference on Smart Technologies in Computing, Electrical and Electronics (ICSTCEE), 2020, pp. 157-162: IEEE.
[26] V. Ashok and A. Yadav, "Fault diagnosis scheme for cross-country faults in dual-circuit line with emphasis on high-impedance fault syndrome," IEEE Systems Journal, 2020.
[27] B. Taheri, S. Salehimehr, F. Razavi, and M. Parpaei, "Detection of power swing and fault occurring simultaneously with power swing using instantaneous frequency," Energy Systems, vol. 11, no. 2, pp. 491-514, 2020.
[28] H. Teimourzadeh, A. Moradzadeh, M. Shoaran, B. Mohammadi-Ivatloo, and R. Razzaghi, "High Impedance Single-Phase Faults Diagnosis in Transmission Lines via Deep Reinforcement Learning of Transfer Functions," IEEE Access, vol. 9, pp. 15796-15809, 2021.
[29] C. Rahmann and A. Castillo, "Fast frequency response capability of photovoltaic power plants: The necessity of new grid requirements and definitions," Energies, vol. 7, no. 10, pp. 6306-6322, 2014.
[30] A. Korpel, "Gabor: frequency, time, and memory," Applied optics, vol. 21, no. 20, pp. 3624-3632, 1982.
[31] S. Salehimehr, B. Taheri, S. A. Hosseini, H. Askarian Abyaneh, and F. Razavi, "A new power swing detection method based on hilbert transform," International Journal of Industrial Electronics, Control and Optimization, 2020.
[32] S. L. Hahn, Hilbert transforms in signal processing. Artech House Signal Processing, 1996.
[33] M. Feldman, "Hilbert transform in vibration analysis," Mechanical systems and signal processing, vol. 25, no. 3, pp. 735-802, 2011.
[34] S. Salehimehr, B. Taheri, and M. Faghihlou, "Detection of power swing and blocking the distance relay using the variance calculation of the current sampled data," Electrical Engineering, pp. 1-15, 2021.
[35] N. Kagan et al., "Influence of rms variation measurement protocols on electrical system performance indices for voltage sags and swells," in Ninth International Conference on Harmonics and Quality of Power. Proceedings (Cat. No. 00EX441), 2000, vol. 3, pp. 790-795: IEEE.
[36] Taheri, Behrooz, and Mostafa Sedighizadeh. "A moving window average method for internal fault detection of power transformers." Cleaner Engineering and Technology 4 (2021): 100195.
[37] R. B. Grimaldi, T. S. Chagas, J. Montalvao, N. S. Brito, W. C. dos Santos, and T. V. Ferreira, "High impedance fault detec-tion based on linear prediction," Electric Power Systems Research, vol. 190, p. 106846, 2021.
[38] J. C. García, V. V. García, and N. Kagan, "Detection of high impedance faults in overhead multi grounded networks," in 2014 11th IEEE/IAS International Conference on Industry Applications, 2014, pp. 1-6: IEEE.
[39] S. A. Hosseini, B. Taheri, H. A. Abyaneh, and F. Razavi, "Comprehensive power swing detection by current signal modeling and prediction using the GMDH method," Protection and Control of Modern Power Systems, vol. 6, no. 1, pp. 1-11, 2021.

Hassan Abniki is a power system engineer at the University of Tehran and Tavanir Co. His main research interests include power system protection, power system transient, and smart grid.

Mostafa Hajati Samsi power system engineer at the Qazvin Islamic Azad University and Vebko Co. His main research interests include power system protection.

Behrooz Taheri was born in Qazvin, Iran, in 1993. He received the B.S. degree in electrical power engineering in 2015. He is received his MSc degree in Electrical Engineering with high honors from Qazvin Islamic Azad University (QIAU), Qazvin, Iran, 2018. He is currently doing his Ph.D. at QIAU. First researcher among all university students in the Qazvin province in 2020, and 2022. He has also been a Member of young researchers and elite club since 2018. His research interests include Power system protection, Non-intrusive load monitoring, Microgrid, and Smart grid.

Seyed Amir Hosseini received his B.S. degree from Islamic Azad University of Najafabad, Isfahan, Iran, in 2008, M.S. degree from Tafresh University, Markazi, Iran, in 2011, and Ph.D. degree from Amirkabir University of Technology, Tehran, Iran, in 2017, all in electrical engineering. He was a Research Assistant for Niroo Research Institute (NRI), from 2014 to 2015. He is currently an Assistant Professor of Electrical and Computer Engineering Group, Golpayegan College of Engineering, Isfahan University of Technology, Golpayegan , Iran. His research interests include power system protection, power system analysis, and smart grids.

IECO

This page intentionally left blank.

International Journal Of
Industrial Electronics Control and Optimization
Print ISSN: 3517-2645
Online ISSN: 3568-2645
Homepage: https://ieco.usb.ac.ir/

Dynamic Multi-Level Generation and Transmission Expansion Planning Model of Multi-Carrier Energy System to Improve Resilience of Power System

Mahnaz Rezaei[1] | Mohammad Tolou Askari[2] | Meysam Amirahmahdi[3] | Vahid Ghods[4]

Department of Electrical Engineering, Semnan Branch, Islamic Azad University, Semnan, Iran.[1,2,3,4]
Corresponding author's email: m.askari@semnaniau.ac.ir

Article Info

Article type:
Research Article

Article history:
Received: 2022-May-13
Received in revised form: 2022-Nov-11
Accepted: 2023-Jan-08
Published online: 2023-Feb-19

Keywords:
Corrective actions,
Coordinated GEP & TEP,
Multi-Carrier energy system,
Resilience improvement

ABSTRACT

Recently, natural disasters such as earthquakes have threatened the power system resilience. On the other hand, the effect of sudden disruptions on equipment, demand growth, shortage of energy resources and high cost of power system expansion have necessitated special attention to demand response programs (DR) and considering uncertainties. Since the presence of an energy hub (EH) leads to change the expansion planning problem of electrical power system. Therefore, in this study, the nature of optimal generation and transmission expansion planning in the presence of EH is studied. Also, the effect of applying the proposed hub with and without considering energy storages (ESs) as well as the short and long-term corrective actions to reduce the losses and costs are investigated. In addition, demand response and line transmission switching are considered as effective approaches to improve resilience in the proposed dynamic multi-level model. This nonlinear problem is solved sequentially considering the random approach and using differential evolution algorithm (DEA) and the symphony orchestra search algorithm (SOSA). In this paper, the proposed objective functions are studied in five-level and the results show the efficiency of this model in solving the planning problem. The findings show that the proposed planning model decreased capital costs of transmission switches as much as 26%, the capital cost of the transmission as much as 2.29%, the congestion cost as much as 1.8%, The capital cost of generation units as much as 3.75%, the payment capacity paid to generation units as much as 1.8%. Also, the expected profit of the generation units has increased as much as 3.75%. To show the competence of the proposed algorithms, the 400-kV test system with 52 buses in Iran is simulated in MATLAB environment

NOMENCLATURE

Sets:

x. *X*	decision making variables of the corrective actions.
t, T	Time (hour).
a, A	Installed generating units.
d, D	Existing generating units.
i, I	Suppliers.
j, J	Consumers.
p, P	Patterns.
r, R	Earthquakes scenarios.
c, C	Attacks scenarios.
n, N	Intensities of event.
w, W	Scenarios for ruining the GenCos and transmission lines in *r* with severity *n*.
h, H	Earthquake –prone geographical regions.
e, E	Load sectors on each load bus.
b, B	Buses.
gu, GU	Decision making variables of the GEP problem.
z, Z	Decision making variables of the events problem.

NOMENCLATURE -CONTINUED

tl, TL	Corridors.
Constant Parameters:	
$D_{t,p,u,e}^{max}$	Maximum annual load demand at sector e of bus u.
FCC_{TL}	Construction cost for a transmission line.
FCC_{TS}	Construction cost for a transmission switch.
$G_{t,p,i}^{min} G_{t,p,i}^{ma}$	Lower and upper bounds of production of GenCo i.
FIC_{t,i_a}^{nG}	Fixed investment cost for the installed generating unit.
π_E^{WIND}	Operation cost wind turbine.
L_{tl}	Length of corridor.
$EENS^{max}$	Maximum value of the expected energy not supplied.
$\mathrm{IC}^{\mathrm{EENS}}$	Cost of expected energy not supplied.
RM_t^{max} ,	Lower and upper limits for reserve margin.
t_0	Base year.
TL^{max}	Maximum number of transmission lines augmented in corridor.
CF^g	Corrective factor related to the reliability.
σ_{t,p,i_a}^{nG}	Constant coefficients of the apparent production cost.
$\Gamma^{r(n):w(h)}$	Outage duration events.
$D_{t,p,j}^{min}$, $D_t^{}$	Lower and upper limits consumption of DisCo.
$\omega_{t,p,u,e}^{r(n):w(h)}$	Weight coefficient of load curtailment at sector e.
Decision Variables:	
$EENS_t$	Expected energy not supplied.
TL	Transmission lines augmented in corridor.
TS	Transmission switches augmented in corridor.
$D_{t,p,j}^{r(n):w(h)}$	Consumption of DisCo.
CC_{total}	Total congestion cost.
$CAP_{t,i}^{Gu}$	Capacity payment the generation units.
CAP_{t,p,i_d}^{eG}	Capacity of existing generating unit.
$EB_{t,i}^{Gu}$	Expected profit the generation units.
EB_{t,i_a}^{nGu}	Expected profit the candidate installed generation unit.
IC_{t,i_a}^{nGu}	Capital cost the candidate installed generating units.
$F_{t,tl}$	Active power flow in corridor.
P_H^{ch}, P_H^{dis}	Amount charging and discharging thermal storage.
$G_{t,p,i}^{r(n):w(h)}$	Production of GenCo i.
D_{peak}	Average peak demand.
CAP_{t,i_a}^{nG}	Installed Capacity of the new generating units.
IC_t^{TL}	Capital cost candidate installed transmission lines.
$IC_{t,tl}^{TS}$	Capital cost candidate installed transmission switch.
VIC_{t,i_a}^{nG}	Variable investment cost the installed generating unit.
$\chi_{t,p,u,e}^{r(n):w(h)}$	Amount of curtailed load at sector e of bus u.
$\vartheta_{t,p,u,i_a}^{nG}$	Predicted market price the candidate installed generating unit.
$\theta_{t,p,v}^{r(n):w(h)}$	Phase angle on the receiving bus of corridor.
$\theta_{t,p,u}^{r(n):w(h)}$	Phase angle on the sending bus of corridor.
θ_α , θ_β	Voltage angles of the node α , β.
δ_{t,p,i_a}	Expected power not supplied before installation of new generating unit.
$Y_{t,p,tl}^{r(n):w(h)}$	Element at the u row and v column in the admittance matrix.

I. Introduction

Power network is one of the most complex networks of the world, and recently has the study of the term "resilience" is one of the main keywords of the power system among industry and academic sectors. Resilience, indicates the capability of an entity or system to recover its normal condition in the shortest time after a failure that changes the system state. In order to guarantee the security plus reliability of the power system, research related to GTEP with the integration of renewable energy systems (RESs) is of great significance. On the other hand, energy hub systems (EHSs) are fully in line with the

future policies of sustainable cities and society [1]. Therefore, with the coordinated use of different infrastructures to meet the needs of customers with increased efficiency, reducing losses, reducing emissions and operating costs, we can see the improvement of this criteria [2]. Considering that climate changes increasing in recent years, natural disasters such as earthquakes and etc can lead to significant losses. Power outages affected more than 710,000 customers in 2015 due to Canada's windstorm, and 1.7 million customers in 2016 due to a massive flood in Australia [3]. The failure of Beijing's transportation system in 2016 due to heavy rains canceled hundreds of flights and trains [4]. Hurricanes cut off more than 7 million customers in Florida, Georgia and South Carolina in 2017, and Hurricane Harvey, which occurred at the same year, resulted in power outage of more than 2 million customers [5]. Since natural disasters affect devices, especially worn-out devices, and constructing more powerful devices is not cost-effective, an efficient planning to heighten power system resilience might be useful. Various studies have discussed the certain and random expansion planning models either in static form or in multiple steps [6]. In [7], expansion planning has been presented to increase resilience in the presence of hybrid micro grids, and a strategy has been formulated to minimize load curtailment and a resilience index has been presented to evaluate performance of the proposed strategy during emergency operations.

In [8], the optimization of integrated generation and transmission expansion is dealt with in the US in a time frame extending to 2050. In [9], a stochastic optimal transmission switching (SOTS) model is developed considering the uncertainty of load, wind power and photovoltaic generation, while minimizing the grid vulnerability. Scenario reduction technique is used for alleviating computational burden of the developed SOTS model. The authors of [10], have solved the GTEP problem considering a random approach that only considers uncertainties. This problem is applied to a power system that is similar to a real system and considers renewable energy resources (wind energy farms) for probabilistic integration. In [11], CGTEP has been presented considering environmental pollution and reliability in the presence of wind turbine and FACTS. In [12], presents a multi-objective bi-level model for planning and operation of integrated energy systems considering the DR program.

In [13], presents a multi-objective optimization framework for long-term planning of EH, in which equipment degradation and integrated demand response (IDR) programs are considered. In [14], proposes a coordinated planning method of power systems and energy transportation networks (ETNs) for resilience enhancement. The uncertainty that occurred due to extreme events such as the use of conventional state-attack has been considered. In [15], a vulnerability-constrained model has been given for the CGTEP considering seismic- and terrorist-induced events. In [16], a plan consisting of investment and operation method has been proposed for controlling the resilience of coupled power distribution and transportation systems. In [17], a model has been proposed that integrates the arranging of the repair sequence of injured components. In [18], a three-level model has been proposed for the sizing problem of networked MGs.

This model solves the problem optimally and considered resilience and cost. In [19], the scenario-based technique has been used to incorporate three dissimilar conditions i.e. daytime with clear-sky and no-fault, daytime with abnormal events, and nighttime into the stochastic dynamic optimization problem for co-existence of PV plants and the load in a service area. Furthermore, the risk-constrained stochastic dynamic SEP problem and Mixed Integer Linear Programming (MILP) framework for one roof has been combined in this reference. In [20], a fragile model is established for investigating the nodal SCF probability.

In this model, the insulation aging of equipment and extreme weather events has been considered. Then, to show the cascading effects of expected SCFs, a response framework for extreme weather conditions is established for a transmission system. In [21], an all-inclusive process has been suggested that helps the system operators to take good decisions for controlling power system resilience and economic value when a severe weather event occurs. In [22], with the help of ensemble numerical weather forecasts a decision-making model for unit scheduling has been suggested. Since the determining the best transmission line to switch by an appropriate time is the main problem for the applicability of TS in wider range. In [23], a heuristic transmission switching (TS) algorithm has been given for increasing resilience by decreasing the load shed in electricity networks affected by extreme weather events (EWEs).

This presented algorithm is fast and scalable. In [24], a transmission resilience planning solution has been suggested by defining the lines to be placed underground for minimizing load shedding in the most cost-efficient method considering historical EWEs (HEWEs). This phenomenon has been considered as a stochastic robust optimization problem and the worst damage situation by the objective function of maximizing load shedding. In [25], a probabilistic proactive generation redispatch strategy has been presented to improve the operational resilience of power grids through wildfires. In [26], a proactive generation redispatch strategy has been proposed to improve the operational resilience of power grids through hurricanes regarding inaccessibility and forced disconnection of renewable energy sources (RESs). The presented results confirm the proactive and dynamic

generation redispatch is effective in improving power system resilience and capability.

This generation redispatch decreases the load curtailments with restricted generation resources through hurricanes by at least 40%. In [27], a two-stage stochastic planning model has been proposed for transmission systems and distributed energy resources (DERs). In this model, the resiliency of the power system has been considered. Furthermore, the normal and emergency situations and their event time has been taken into account. In [28], to determine the probability of failure events, the failure rates of transmission lines due to extreme weather conditions have been modeled.

Then, to schedule generators, optimally and flexible loads while meeting the frequency security restrictions under transmission line failure events, a two-stage stochastic frequency constrained unit commitment (FCUC) model is presented. In [29], a resiliency investment optimization model has been suggested that defines optimal investments in the transmission grid for protecting against extreme weather events. This model consists of OTS and generator dispatch decisions for minimizing unserved load through an extreme weather event. In [30], a static model for coordinated generation and transmission expansion planning (CGTEP) has been presented. This model alleviate the vulnerability of power system in contrast to physical deliberate attacks in the horizon of planning. In addition, the physical deliberate attacks and their subsequent influences are evaluated through the process of scenario building. In [31], the capacity expansion and switch installation in electric systems has been combined which results in optimum performance during nominal operations and attacks. This model provides bridges long-term system planning for transmission development and short-term switching operations response to attacks. In [32], the vulnerability of the power system exposed to physical deliberate attacks (PDAs) has been investigated while the power system and communication network are geographic-cyber codependents. The attacker applies a PDA on transmission lines and the communication network to injure the power system, and on the other side, the system operator (SO) reacts as a defender by doing essential actions against them.

The following gaps are reported base on the literature review.

- The coordination GEP and TEP to improve the resilience was ignored.
- Effects of multi-carrier energy system in CGTEP was ignored.
- The natural disaster such as earthquake was not considered in the previous studies.
- Finally, a dynamic and comprehensive model by considering DR, ES, uncertainties, RES, and corrective actions were not given in the previous researches.

The novelties of this paper are compared with recent works and is shown in Table 1.

The main contributions of this paper are as follows:

- To provide an improved dynamic model, coordinated GTEP by applying the proposed hub, wind turbine, and electrical and thermal storage.
- To develop a new five-level architecture using short and long-term corrective actions on three scales by considering DR programs, uncertainties, social welfare, reliability to improve the resilience in the power system.
- To develop the model by considering the proposed EH.
- To investigate random scenarios to reach an overall optimal point and to solve the proposed large-scale mixed integer nonlinear five-level model with the aim of strengthening the resilience of power systems, which has been considered in limited studies in the field of generation and transmission expansion planning.

The rest of this article is organized as follows: Section 2 formulates the proposed model, objective function and constraints of different levels. Section 3 describes the proposed model solution using mathematical algorithms. Section 4 presents the numerical results and the calculation on the 52-bus network in Iran. Finally, conclusions are explained in Section 5.

TABLE 1
COMPARISON OF THIS PAPER WITH RECENT PUBLISHED PAPERS

Ref	Objective function	CGTEP	Implementation approach	Muiti-level model	Type event	Vulnerability assessment	transmission switching	Renewable	Uncertainty	ES	DR program	Resilience
[2]	Cost & Loss & Emission	×	MILP CPLEX solver	×	Seasonal variation	×	×	✓	✓	✓	✓	✓
[9]	Cost	×	MINLP	×	×	✓	✓	✓	✓	×	×	×
[10]	Cost	×	MILP	×	×	×	✓	✓	✓	×	×	×
[11]	Cost & Profit & Emission	✓	MINLP	×	×	×	×	✓	✓	×	×	×
[12]	Cost & Profit & Emission	×	NSGA-II algorithm	Bi-level	×	×	×	✓	✓	✓	✓	×
[13]	Cost & Loss & Emission	×	Max-min fuzzy method	×	×	×	×	✓	✓	✓	✓	×
[14]	Cost	×	Two stage robust programming	Tri-level	×	×	×	✓	✓	×	×	✓
[15]	Cost & Profit & Loss	✓	MINLP&SOS algorithm	Quad-level	Seismic-terrorist	✓	✓	×	✓	×	✓	✓
[16]	Cost	×	Benders decomposition and C&CG algorithms	Tri-level	Natural disaster	×	✓	×	✓	×	×	✓
[17]	Cost	×	p-robust & scenario-based decomposition	×	attack	×	×	×	✓	×	×	✓
[18]	Cost	×	AG algorithm	Tri-level	Damage system	×	×	✓	✓	×	×	✓
[19]	Cost	×	MILP	×	×	×	×	✓	✓	×	✓	✓
[20]	Cost	×	MINLP	×	×	×	✓	×	✓	×	×	✓
[21]	Cost & Profit	×	Decision analysis	×	Typhoon	×	×	✓	✓	×	×	✓
[22]	Cost	×	Decision making	×	Typhoon	×	×	✓	✓	×	×	✓
[23]	Cost	×	MIP TS algorithm	×	Typhoon	×	✓	×	×	×	×	✓
[24]	Cost	×	Decomposition-based algorithm & Monte Carlo	×	Natural disaster	✓	×	×	✓	×	×	✓
[25]	Cost	×	Markov decision CPLEX solver	×	wildfires	×	×	×	✓	×	×	✓
[26]	Cost	×	MILP	×	Typhoon	×	×	✓	✓	×	×	✓
[27]	Cost	×	MILP Benders decomposition technique	Bi-level	Emergency condition	✓	×	×	✓	×	×	✓
[28]	Cost	×	regularized L-shape algorithm	×	extreme weather	×	×	×	✓	×	×	✓
[29]	Cost	×	SOCP programming	×	Typhoon	×	✓	✓	✓	×	×	✓
[30]	Cost	✓	MILP CPLEX solver	Bi-level	attack	✓	×	×	✓	×	×	×
[31]	Cost	×	MIP decomposition via two-layer cutting plane algorithm	Tri-level	attack	×	✓	✓	✓	×	×	✓
[32]	Cost	×	MILP-genetic algorithm	Bi-level	attack	✓	×	×	✓	×	×	×
This paper	Cost & Profit & Loss	✓	CPLEX solver MINLP DE algorithm &SOSA	Five-level	Earthquake	✓	✓	✓	✓	✓	✓	✓

II. Proposed model of multi period CGTEP problem

Recently, various challenges in the context of power system resilience have concerned the researchers [33]. On the other hand, simultaneous operation of different generation and transmission infrastructures like artificial electricity and gas network has been presented under the concept of EH, which is cost-effective to be employed for heightening resilience. In this study, the EH includes boiler, CHP, transformer, converters, and wind turbine. The network inputs include gas, electricity and heat, that enter the network, and the network outputs include electricity and heat. The schematic of a multi-carrier energy system that operates as an interface between input and output energy carriers is shown in Fig. 1.

A. First Level Planning

The objective function at the first level includes operational costs and input energy transmission costs. In this study, the input carriers include electricity, natural gas, heat, energy storage systems, and wind turbine, which are described in Equ. (1) [34].

$$\min F = \sum_{t=1}^{24} IC_E(t)+IC_G(t)+IC_H(t)+IC_{ES}(t)+IC_{HS}(t) \quad (1)$$

In the first level objective function, IC_E is the cost of electricity transmission (including the electricity transmission cost from wind turbines and the electricity transmission cost from the electricity market); IC_G, IC_H, IC_{ES}, and IC_{HS} are the costs of natural gas, heat transmission, electrical and thermal energy storage system which are described using Equs. (2)-(6).

$$IC_E(t)=\left[\pi_E^{NET}(t)P_E^{NET}(t)\right]+\left[\pi_E^{WIND}(t)P_E^{WIND}(t)\right] \quad (2)$$

$$IC_G(t)=\left[\pi_G^{NET}(t)P_G^{NET}(t)\right] \quad (3)$$

$$IC_H(t)=\left[\pi_H^{NET}(t)P_H^{NET}(t)\right] \quad (4)$$

$$IC_{ES}(t)=\left[\pi_E^{op}\left(P_E^{ch}(t)+P_E^{dis}(t)\right)\right]+\left[\pi_E^{NET}(t)\left(P_E^{ch}(t)-P_E^{dis}(t)\right)\right] \quad (5)$$

$$IC_{HS}(t)=\left[\pi_H^{op}\left(P_H^{ch}(t)+P_H^{dis}(t)\right)\right]+\left[\pi_H^{NET}(t)\left(P_H^{ch}(t)-P_H^{dis}(t)\right)\right] \quad (6)$$

where π_E^{NET}, π_E^{WIND}, π_G^{NET}, and π_H^{NET} are the cost of purchasing each kWh of power from the grid, wind turbine, gas and heat network at time *t*, respectively; π_E^{op} and π_H^{op} are the operation cost of electrical and thermal energy, respectively; P_E^{NET}, P_E^{WIND}, P_G^{NET}, and P_H^{NET} represent the electrical power of the grid, wind turbine, natural gas power taken from the network and the input thermal power of the network, respectively; P_E^{ch}, P_E^{dis}, P_H^{ch}, and P_H^{dis} are the amount of power (charge-discharge) of the electrical and thermal energy storage systems, respectively.

1) First Level Planning Constraints

All devices of the EHS have constraints like limited output power, and etc. These constraints along with power generation and consumption balance are described in this section. Equ. (7) represents the electrical energy balance in the EH that sets the generated electricity power equal to the demanded electricity power.

$$P_E^D(t)=\left\{\begin{array}{l}\left[\eta_E^T P_E^{NET}(t)\right]+\left[\eta_{GE}^{CHP} P_G^{NET\,CHP}(t)\right]+\\ \left[\eta_{CONV}^{WIND} P_E^{WIND}(t)\right]+\left[P_E^{dis}(t)-P_E^{ch}(t)\right]\end{array}\right\} \quad (7)$$

In Equ. (7), η_E^T, η_{CONV}^{WIND}, and η_{GE}^{CHP} represent the electric transformer coefficient, the wind turbine converter efficiency, the CHP system efficiency to convert the input gas power into electric power respectively; Equ. (8) represents the balance of the input and output gas of the EH [34].

$$P_G^D(t)=P_G^{NET}(t)-P_G^{NET\,CHP}(t)-P_G^{NET\,BOIL}(t) \quad (8)$$

where P_G^{NETCHP} and $P_G^{NETBOIL}$ are the natural gas power received from the CHP and boiler system, respectively; The heat demand is the amount of thermal energy used to heat the consumption water in the central heating system, as given:

$$P_H^D(t)=\left\{\begin{array}{l}\left[\eta_{GH}^{CHP} P_G^{NET\,CHP}(t)\right]+\left[\eta_{GH}^{BOIL} P_G^{NET\,BOIL}(t)\right]\\ +\left[P_H^{dis}(t)-P_H^{ch}(t)\right]+P_{BOIL}^{NET}(t)\end{array}\right\} \quad (9)$$

In Equ. (9), η_{GH}^{BOIL} and η_{GH}^{CHP} represent the efficiency of the boiler and the CHP system for converting gas to heat, respectively. Since the network generation has a certain capacity, and it cannot be operated more than its capacity, the network power limits are expressed in Equs. (10)-(13) [34].

$$0 \le P_E^{NET}(t) \le P_E^{NET\,MAX} \quad (10)$$

$$0 \le P_E^{NET}(t) \le P_{IN}^{T} \quad (11)$$

$$0 \le P_G^{NET\,CHP}(t) \le P_{IN}^{CHP} \quad (12)$$

$$0 \le P_G^{NET\,BOIL}(t) \le P_{IN}^{BOIL} \quad (13)$$

where $P_E^{NET\ MAX}$, P_{IN}^{BOIL}, P_{IN}^{CHP}, and P_{IN}^{T} represent the maximum power capacity received from the network, the maximum capacity of CHP, and the maximum capacity of electrical transformers. The output power of the wind turbine depends on the wind speed, and varies regarding the turbine speed as given in the following equation [34]:

$$P_E^{WIND}(v(t))=\left\{\begin{array}{ll}0 & ;v(t)\le v_{in}\ge v_{out}\\ \dfrac{v(t)-v_{in}}{v_r-v_{in}}P_r^{WIND} & ;v_{in}\le v(t)\le v_r\\ P_r^{WIND} & ;v_r\le v(t)\ge v_{out}\end{array}\right\} \quad (14)$$

2) DS-DOCR Characteristics

In (1), the formula for standard relay tripping time is shown. As seen, the tripping time of DOCRs is a function of the short-circuit current that passes the relays. In addition, the coefficients for standard characteristics are given in Table 2 [4, 12].

$$t_i = TDS_i \frac{A_i}{\left(\frac{I_{F,i}}{I_{p,i}}\right)^{B_i} - 1} \quad (15)$$

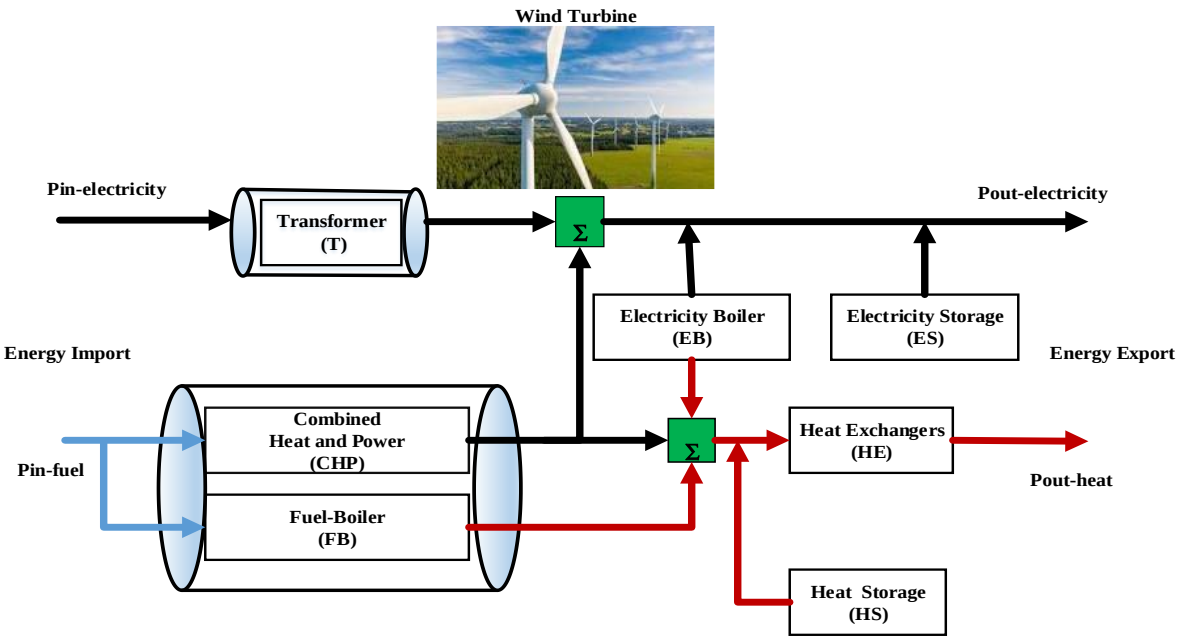

Fig. 1. Structure energy hub system.

In Equ. (14), P_r^{WIND} and v_r represent the rated speed and rated output power of wind turbine respectively; $v(t)$ represent the wind speed at time t and scenario s. v_{in} and v_{out} , represent the cut in and cut out speeds of wind turbine, respectively.

B. Second Level Planning

At this level, first the purpose is to consider corrective actions like network re-generation and reconfiguration to minimize technical and economic losses, maximize social welfare and minimize load curtailment. the second level objective function is described using Equ. (16) [15], [35]:

$$\max_{x\in X} \mathbf{of:}\ OF = \left[\begin{array}{l} \sum_{j\in J} \sigma_{t,p,j}\left(\left(D_{t,p,j}^{r(n):w(h)}\right)^2 + D_{t,p,j}^{r(n):w(h)} + 1\right) - \\ \sum_{i\in I} \sigma_{t,p,i}\left(\left(G_{t,p,i}^{r(n):w(h)}\right)^2 + G_{t,p,i}^{r(n):w(h)} + 1\right) - \\ \sum_{u\in B}\sum_{e\in E} \chi_{t,p,u,e}^{r(n):w(h)} \cdot IC_{t,p,u,e}^{r(n):w(h)}\left(\Gamma^{r(n):w(h)}\right) \omega_{t,p,u,e}^{r(n):w(h)} \end{array}\right] \quad (16)$$

where $\sigma_{t,p,j}$ and $\sigma_{t,p,i}$ are the significant profit coefficients of Disco j consumer and GenCo i generation cost, respectively; $D_{t,p,j}^{r(n):w(h)}$ and $G_{t,p,i}^{r(n):w(h)}$ are the consumption of Disco j and generation of GenCo i, respectively; $\chi_{t,p,u,e}^{r(n):w(h)}$ is the load curtailment rate. $IC_{t,p,u,e}^{r(n):w(h)}(\Gamma^{r(n):w(h)})$ is the load curtailment cost over time resulting from disasters and $\omega_{t,p,u,e}^{r(n):w(h)}$ is the load curtailment weight coefficient.

1) Second Level Planning Constraints

In this section, described network balance in which $D_{t,p,j,u,e}^{max}$ is the maximum annual load demand, $Y_{t,p,tl}^{r(n):w(h)}$ represents the elements of the network admittance matrix, and $\theta_{t,p,v}^{r(n):w(h)}$ represents the received bus phase angle in Equ. (17) [15].

$$G_{t,p,i,u}^{r(n):w(h)} - \sum_{e\in E}\left(D_{t,p,j,u,e}^{max} - \chi_{t,p,u,e}^{r(n):w(h)}\right) = \sum_{tl\in L} Y_{t,p,tl}^{r(n):w(h)}\,\theta_{t,p,v}^{r(n):w(h)} \quad (17)$$

Equ. (17) is the limit of power generated by each GenCo i, and Equ. (18) shows the power purchased by each DisCo j, where $G_{t,p,i}^{max}$ and $G_{t,p,i}^{min}$ are the upper and lower limits of GenCo i generation, also $D_{t,p,j}^{max}$ and $D_{t,p,j}^{min}$ are the upper and lower limits of Disco j consumption [17].

$$G_{t,p,i}^{min} \le G_{t,p,i}^{r(n):w(h)} \le G_{t,p,i}^{max} \quad (18)$$

$$D_{t,p,j}^{min} \le D_{t,p,j}^{r(n):w(h)} \le D_{t,p,j}^{max} \quad (19)$$

Equ. (20) shows the allowed amount of load curtailment at different accident severity scales:

$$\chi_{t,p,u,e}^{r(n):w(h)} \le D_{t,p,u,e}^{max} \quad (20)$$

The power flow relationship of the transmission line and its safety constraints are formulated in Equs. (21)-(23) which the power flow is represented by $F_{t,p,tl}^{r(n):w(h)}$. $F_{t,p,tl}^{max}$ is the maximum active power flow [15].

$$F_{t,p,tl}^{r(n):w(h)} - Y_{t,p,tl}^{r(n):w(h)} \left(\theta_{t,p,u}^{r(n):w(h)} - \theta_{t,p,v}^{r(n):w(h)} \right) = 0 \tag{21}$$

$$-\left| Y_{t,p,tl}^{r(n):w(h)} \cdot \left(\theta_{t,p,u}^{r(n):w(h)} - \theta_{t,p,v}^{r(n):w(h)} \right) \right| \le F_{t,p,tl}^{\max} \tag{22}$$

$$-\left| Y_{t,p,tl}^{r(n):w(h)} \left(\theta_{t,p,v}^{r(n):w(h)} - \theta_{t,p,u}^{r(n):w(h)} \right) \right| \le F_{t,p,tl}^{\max} \tag{23}$$

C. Third level Planning

At this level, the technical and economic loss function is maximized regarding the accidents severity to maximize resilience of the generation and transmission networks [15].

$$\max_{z \in Z} \left[\sum_{b \in B} \sum_{e \in E} \chi_{t,p,u,e}^{r(n):w(h)} . \mathrm{IC}_{t,p,u,e}^{r(n):w(h)} \left(\Gamma^{r(n):w(h)} \right) \right] \tag{24}$$

1) Third Level Planning Constraints:

In this section, Limitations related to the transmission lines and generation units, that can be damaged during earthquake, are defined in Equs. (25)-(28).

$$\sum_{\forall i \in I} \varphi_{t,p,i}^{r(n):w(h)} \le \varphi_{i,\max}^{r(n)} \tag{25}$$

$$\sum_{\forall tl \in L} \varphi_{t,p,tl}^{r(n):w(h)} \le \varphi_{L,\max}^{r(n)} \tag{26}$$

$$\sum_{\forall i \in I} \varphi_{t,p,i}^{c(m):q(k)} \le \varphi_{i,max}^{c(m)} \tag{27}$$

$$\sum_{\forall tl \in L} \varphi_{t,p,tl}^{c(m):q(k)} \le \varphi_{L,\max}^{c(m)} \tag{28}$$

where $\varphi_{t,p,i}^{r(n):w(h)}$ is the number of generation units, and $\varphi_{t,p,tl}^{r(n):w(h)}$ is the number of transmission lines which might be destroyed in *r* with severity *n* under scenario *w* at earthquake-prone geographical area *h*, respectively; $\varphi_{t,p,i}^{c(m):q(k)}$ is the number of generation units, and $\varphi_{t,p,tl}^{c(m):q(k)}$ is the number of transmission lines which might be destroyed in *c* with severity *m* under scenario *q* at attack-prone geographical area *k*, respectively [15], [31], [32].

D. Fourth Level Planning

At this level, generation expansion planning is proposed to heighten resilience. In Equ. (29), $EB^{GU}{}_{t,i}$ represents the expected profit of the GenCo *i*, $IC_{t,i}^{nGU}$ represents the capital cost of the generation units associated with the new installation capacity by GenCo *i*. $CAP_{t,i}^{GU}$ represents the payment capacity paid by the generation units to heighten resilience [15].

$$\max_{gu \in GU} \text{of}: OF = \left[\sum_{t \in T} \frac{EB_{t,i}^{GU}}{(1+d)^{t-t_0}} - \sum_{t \in T} \frac{IC_{t,i}^{nGU}}{(1+d)^{t-t_0}} + \sum_{t \in T} CAP_{t,i}^{GU} \right] \tag{29}$$

The second term in Equ. (29) indicates the fixed and variable investment costs of each generation unit during the planning period, which is described as follows:

$$IC_{t,i_a}^{nGU} = VIC_{t,i_a}^{nG} + FIC_{t,i_a}^{nG} \tag{30}$$

In Equ. (30), the variable investment cost as the product of investment cost associated with each generation unit by the installation capacity of each generation unit, can be calculated using Equ. (31):

$$VIC_{t,i_a}^{nG} = IC_{t,i_a}^{G} \cdot CAP_{t,i_a}^{nG} \tag{31}$$

where IC_{t,i_a}^{G} is capital cost for generating unit; CAP_{t,i_a}^{nG} is installed capacity of candidate generating by Genco *i*. In Equ. (32), the expected profit is obtained using the total expected profit associated with the new and existing installed generation units as given [15]:

$$EB_{t,i}^{GU} = \sum_{a \in A} EB_{t,i_a}^{nGU} + \sum_{d \in D} EB_{t,i_d}^{eGU} \tag{32}$$

Equs. (33) and (34) describe the expected profit associated with each new and existing installed generation unit in which D_p is the period length, $\vartheta_{t,p,u,i_a}^{nG}$ and $\vartheta_{t,p,u,i_a}^{eG}$ are the predicted market price for installing new and existing generation units, respectively; CAP_{t,p,i_a}^{nG} and CAP_{t,p,i_d}^{eG} are the capacity of each new and installed generation unit with GenCo *i*, respectively.

$$EB_{t,i_a}^{nGU} = \sum_{p \in P} \sum_{a \in A} D_p \left[\vartheta_{t,p,u,i_a}^{nG} CAP_{t,p,i_a}^{nG} - \left(\sigma_{t,p,i_a}^{nG} \left(CAP_{t,p,i_a}^{nG} \right)^2 + CAP_{t,p,i_a}^{nG} + 1 \right) \right] \tag{33}$$

$$EB_{t,i_d}^{eGU} = \sum_{p \in P} \sum_{d \in D} D_p \left[\vartheta_{t,p,u,i_d}^{eG} CAP_{t,p,i_d}^{eG} - \left(\sigma_{t,p,i_d}^{eG} \left(CAP_{t,p,i_d}^{eG} \right)^2 + CAP_{t,p,i_d}^{eG} + 1 \right) \right] \tag{34}$$

The payment capacity paid by generation units to heighten resilience is given in Equ. (35). In this equation, δ_{t,p,i_a} and ρ_{t,p,i_a} are the expected power not supplied before and after installing each generation unit by GenCo *i*, respectively; and IC^{EENS} is the expected cost not supplied.

$$CAP_{t,i}^{GU} = \sum_{p \in P} \sum_{a \in A} D_p \left[\left(\delta_{t,p,i_a} - \rho_{t,p,i_a} \right) \left(IC^{EENS} - \vartheta_{t,p,u,i_a}^{nG} \right) \right] \tag{35}$$

1) Fourth Level Planning Constraints

In this section, the limitations associated with generation expansion planning, including the capacity of each installed new generation unit and the investment cost of each generation unit are described in Equs. (36)-(38) [15]:

$$0 \le CAP_{t,i_a}^{nG} \le CAP_{t,i_a}^{nG\max} \tag{36}$$

$$0 \le IC_{t,i_a}^{nG} \le IC_{t,i_a}^{nG\max} \tag{37}$$

$$G_{t,p,i}^{\min} \le CAP_{t,p,i_a}^{nG} + CAP_{t,p,i_d}^{eG} \le G_{t,p,i}^{\max} \tag{38}$$

On the other hand, the storage margin for excess generation capacity is expressed as:

$$\begin{aligned} &\left(1+RM_t^{\min}\right) \sum_{p \in P} \sum_{b \in B} D_{\text{peak}} \le \left(1 \pm CF^r\right) \\ &\left(\sum_{i \in I} \sum_{a \in A} CAP_{t,i_a}^{nG} + \sum_{i \in I} \sum_{d \in D} CAP_{t,i_d}^{eG} \right) \le \left(1+RM_t^{\max}\right) \sum_{p \in P} \sum_{b \in B} D_{\text{peak}} \end{aligned} \tag{39}$$

$$\left(1-CF^{g}\right)EENS_{t} \le EENS^{\max} \quad (40)$$

where in Equs. (39) and (40), RM_t^{min} and RM_t^{max} are the restrictions of the reservation margin, respectively; D_{peak} is the average peak demand, and CF^r is a corrective actions associated with the generation reserve margin [15].

E. *Fifth Level Planning*

At this level, transmission expansion planning considering transmission switching as low-cost corrective actions is proposed. In Equ. (41), ${IC_t}^{TL}$ and ${IC_t}^{TS}$ are the cost of investing in candidate transmission lines and transmission switching, and CC_{total} is the congestion cost [15].

$$\min_{uv \in UV} of: OF = \left[\sum_{t\in T}\frac{{IC_t}^{TL}}{(1+d)^{t-t_0}}+\sum_{t\in T}\frac{{IC_t}^{TS}}{(1+d)^{t-t_0}}+\sum_{t\in T}\frac{CC_{total}}{(1+d)^{t-t_0}}\right] \quad (41)$$

In Equ. (42), the capital cost of installed transmission candidate lines is the product of the capital cost of the installed transmission candidate lines of each corridor by the number of lines augmented in each corridor, and expressed by [31]:

$${IC_t}^{TL} = \sum_{TS\in L} IC_{t,tl}^{TL}.\,TL \quad :\forall tl \in TL \quad (42)$$

where TL is refer to the transmission lines augmented in the corridor, and $IC_{t,tl}^{TL}$ is the capital cost of a candidate installed transmission lines in the corridor [31].

On the other hand, In Equ. (43), the capital cost of the newly installed transmission lines of each corridor is calculated as the product of the transmission line construction cost by the active power flow of each corridor and the length of the corridor, as given:

$$IC_{t,tl}^{TL} = FCC_{TL} L_{tl} F_{t,tl} \quad (43)$$

where FCC_{TL} is the construction cost for a transmission; L_{tl} is the length of the corridor; $F_{t,tl}$ is active power flow in the corridor. The capital cost of a candidate installed transmission switching is the product of the capital cost of the candidate installed transmission switching in each corridor by the transmission switching augmented in corridor and expressed using Equ. (44) [15]:

$${IC_t}^{TS} = \sum_{TS\in L} {IC_{t,tl}}^{TL} TS \quad :\forall tl \in TL \quad (44)$$

where TS is the transmission switches augmented in the corridor. The capital cost of the candidate installed transmission switching is expressed in Equ. (45):

$$IC_{t,tl}^{TS} = FCC_{TS} \cdot F_{t,tl} \quad (45)$$

where FCC_{TS} is the fundamental construction cost for a transmission switch.

1) Fifth Level Planning Constraints

In this section, the limitations associated with transmission expansion planning are presented using Equs. (46)-(49). The maximum number of transmission lines which is augmented is explained in Equ. (46). Equ. (47) demonstrates the maximum transmission switching that can be augmented in each corridor and in each period. Equs. (48) and (49) express the total budget constraints available for the transmission network and switching device, respectively [31].

$$TL \le TL^{\max} \quad (46)$$

$$TS \le TS^{\max} \quad (47)$$

$$IC_{t,tl}^{TL} + IC_{t,tl}^{TS} \le \Phi_t \quad (48)$$

$$IC_{t,tl}^{TL} + IC_{t,tl}^{TS} \le \Phi \quad (49)$$

The weight of each disaster scenario *w* in *r* with severity *n* for ruining the GenCos and TLs in Equs. (50) and (51), respectively [15]:

$$\psi_{t,p,i}(w) = \frac{\chi_{t,p}^{r(n):w(h)}}{\varphi_{t,p,i}^{r(n):w(h)}} \Big/ \sum_{\substack{w'\in W \\ w'\neq w}} \frac{\chi_{t,p}^{r(n):w'(h)}}{\varphi_{t,p,i}^{r(n):w'(h)}} \quad (50)$$

$$\psi_{t,p,tl}(w) = \frac{\chi_{t,p}^{r(n):w(h)}}{\varphi_{t,p,tl}} \Big/ \sum_{\substack{w'\in W \\ w'\neq w}} \frac{\chi_{t,p}^{r(n):w'(h)}}{\varphi_{t,p,tl}^{r(n):w'(h)}} \quad (51)$$

By the same token, the weight of each disaster scenario *q* in *c* with severity *m* for ruining the GenCos and TLs are expressed in Equs. (52) and (53), respectively [15].

$$\psi_i(q) = \frac{\chi_{t,p}^{c(m):q(k)}}{\varphi_{t,p,i}} \Big/ \sum_{\substack{q'\in q \\ q'\neq q}} \frac{\chi_{t,p}^{c(m):q'(k)}}{\varphi_{t,p,i}^{c(m):q'(k)}} \quad (52)$$

$$\psi_{t,p,tl}(q) = \frac{\chi_{t,p}^{c(m):q(k)}}{\varphi_{t,p,tl}} \Big/ \sum_{\substack{q'\in q \\ q'\neq q}} \frac{\chi_{t,p}^{c(m):q'(k)}}{\varphi_{t,p,tl}^{c(m):q'(k)}} \quad (53)$$

III. Solution Methodology

In this paper, in order to solve the nonlinear problem, the differential evolution algorithm (DEA) and the symphony orchestra search algorithm (SOSA) are used. The meta-heuristic methods have attracted attention due to simplicity, resilience, not requiring differentiation, and skipping local optima. In this paper, the meta-heuristic DE algorithm is used, which can be classified as evolutionary algorithms. This algorithm employs a differential operator to generate new solutions, it is population-based, its behavior is stochastic, and starts by a set of suggested responses, and tries to achieve a better result in a set of sequential iterations. The unique method of this algorithm for generating new solutions makes it more efficient compared to other optimization algorithms. Since correct selection of the optimal location prevents capital and time loss, this issue should be considered in particular. Optimization is to satisfy min and max destinations of the objective function by formulating and solving it in terms of cost, efficiency, profit and etc. In the DE algorithm, all members of a population have an equal chance to be selected as a parent. The Details were described in [36]. In the first step, the initial information of the proposed hub, like parameters and inputs are introduced, and the gas used by the boiler and CHP

are allocated based on the algorithm populations at t=1 (Fig. 2).

Step 1: Enter the network load data.

Step 2: Select the required parameters.

Step 3: Initialize the memory of the optimization algorithm of interest.

Step 4: Repeat the optimization algorithm.

Step 5: At time t = 1, Add all selected candidate GTEP for each replacement.

Step 6: Create a new solution vector.

Step 7: Set the planning patterns to p = 1.

Step 8: Execute the first level of this algorithm (includes the corrective actions).

Step 9: Run the second level of this algorithm (includes adjusting the event counter, intensity and number of scenarios for earthquake prone regions, which is saved after identifying the vulnerable levels), solve the catastrophic event problems for earthquake-prone regions Then save the vulnerable levels specified after execution. Finally, save the weights of destructive scenarios, save the worst scenario).

Step 10: Execute the third and fourth levels. Then save generation expansion plans, check reserve margins, and EENS, calculate and send the defects of each constraint, save the final generation expansion plan, and implement. Determine the capital cost of the transmission lines, the capital cost of the transmission switching, and congestion cost, and save the final transmission expansion plan

Step 11: $t = t + 1$, If $t<T$ go to step 5.

Step 12: Find the current objective function.

Step 13: Is the new solution better than the solution stored in memory?

Step 14: Save and update the new solution in memory.

Step 15: The successful solution is finished.

Modeling by the SOSA of the problem is as follows:

First, parameters and initial values are added to the algorithm.

Then, in the next step, the initial values are analyzed and sorted. The next step is to improve the problem. For the mentioned problem, it is done as follows. First, all network and energy hub information is entered into the algorithm. Then, the optimal state of the energy hub is calculated and stored in the memory of the algorithm. The next step is to implement the 5 mentioned steps.

The graphical representation of SOSA parameters is shown in Fig. 3.

IV. Results and Discussions

The proposed model was implemented by a PC with a Intel Core i5 processor and 8 GB RAM. Fig. 4 shows the network diagram on Iran's map. In 5-year planning horizon a five-level expansion plan has been used to maximize social welfare and considering corrective actions and switching capability to heighten resilience and minimize costs. The candidate new substations and transmission corridors are represented with dashed circles and lines, respectively. With extensive studies in this area, the impact of renewables such as wind turbines are used to meet part of consumer demand in the proposed hub [37]-[38]-[39]- [40]. Since the EH can partially operate based on the capacity, this paper evaluates the proposed hub based on changes in its location. Thus, the best location for the hub by implementing wind turbine is demonstrated. The proposed method leads to cost-effective results Earthquake prone regions and attack prone are divided into West, Southeast, North, Northeast and South, which are represented in cream, blue, yellow, purple, and pink. In this paper, three possible intensity of earthquake and attack which are including medium, relatively severe, and severe. List of attacks and threats are provided in [30], [41]. Also, IC^{EENS}, CF^{g}, and CF^{r} are 250 MWh, 25MW, and 0.001, respectively. The interest rates were set at 10%. The system information is given in [36]. The meteorological data is selected based on the International Institute of Seismology and Earthquake Engineering website [42]. In this paper, in order to evaluate the effectiveness of the proposed CGTEP, two simulations with and without considering ESs and corrective actions in a 52-bus 400 kV network in Iran are defined and applied. Also, this study is compared with the previous study that the EH was ignored [15]. The five-level CGTEP by applying the proposed hub with and without of storage devices without considering and evaluating the earthquake-induced events in the first to third scales of earthquake are shown in Tables 2 and 3. Similarly, Tables 4 and 5 shows the results of earthquake-induces events, aiming to heighten resilience. Results of Table 3 and 5 by applying the proposed EH in the absence/presence of ESs show that by applying short and long-term corrective actions, the investment costs are reduced and the profit is increased, significantly. Also comparing Tables 3 and 5 by applying the proposed EH in the absence/presence of electrical and thermal ESs with [15] (without proposed hub) shows the cost reduction. An in-depth look and comparison of the results proposed EH in Table 3 and 5 with absence ESs and comparing it with the results in [15], reduction of transmission switching capital costs (IC^{TS}) in three scales by 73.41%, 76.08%, and 0.66% is obvious. On the other hand, show a reduction of 5.91%, 1.08%, and 1.27% in the capital cost of the transmission lines (IC^{TL}), compared to [15]. The congestion cost (CC_{total}) is also measured in three scales is reduced 1.33% ، 1%, and 3.44% by applying the proposed hub to the levels compared to the study conducted in [15]. In this study, the expected profit of the generation units (EB^{GU}) has increased 3.25%, 1.5%, and 1.56%. To this end, the capital cost of generation units (IC^{nGU}) has reduced 9.93%, 11.33%, and 9.71%. The payment capacity paid to generation units GenCos (CAP^{GU}) so has reduced by 1.5%, 2.02%, and 2.6%, compared to [15]. Similarly to, the comparison of the results proposed EH in Table 3 and 5 with presence ESs and

comparing it with the results in [15], reduction of transmission switching capital costs (IC^{TS}) in all three scales by 73.31%, 2.43%, and 0.67% is obvious. On the other hand, show a reduction of 5.57%, 3.15%, and 3.58% in the capital cost of the transmission lines (IC^{TL}). The congestion cost (CC_{total}) is also measured in three scales considering short and long-term reactions, which is reduced 1.27% ,2.83 %, and 6.91%. In this study, the expected profit of the generation units (EB^{GU}) has increased 1%, 4.64%, and 3.64%. To this end, the capital cost of all generation units (IC^{nGU} has reduced 12.6%, 14.76%, and 14.93%. The payment capacity paid to all generation units GenCos (CAP^{GU}) so has reduced by 1.7%, 3.43%, and 6.7%, which has reduced by 1.6%, 3%, and 7.3% compared to [15]. As can be seen from the results, the implementation of short and long-term reactions also the presence of the proposed hub with ESs in CGTEP is effective to heighten resilience, minimize the costs and maximize profit. In additionally, an in-depth look and comparison of the results presented in Table 3 by ignoring corrective actions and absence/presence ESs show that the capital costs of transmission switches (IC^{TS})

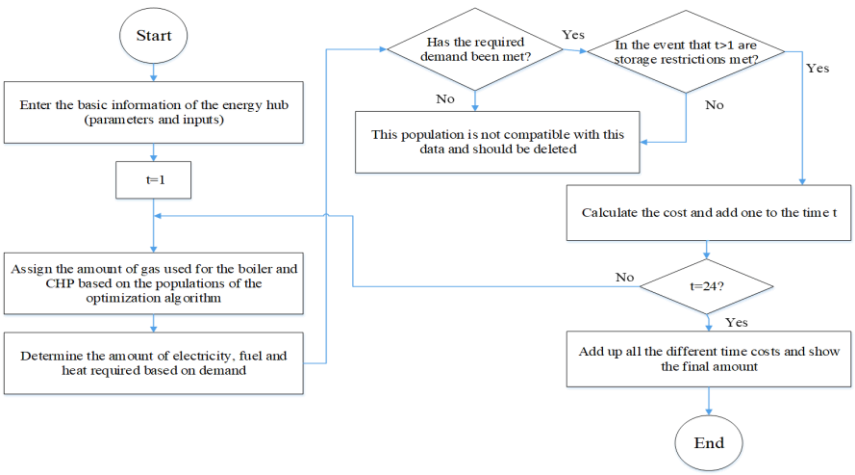

Fig. 2. The proposed energy hub optimization.

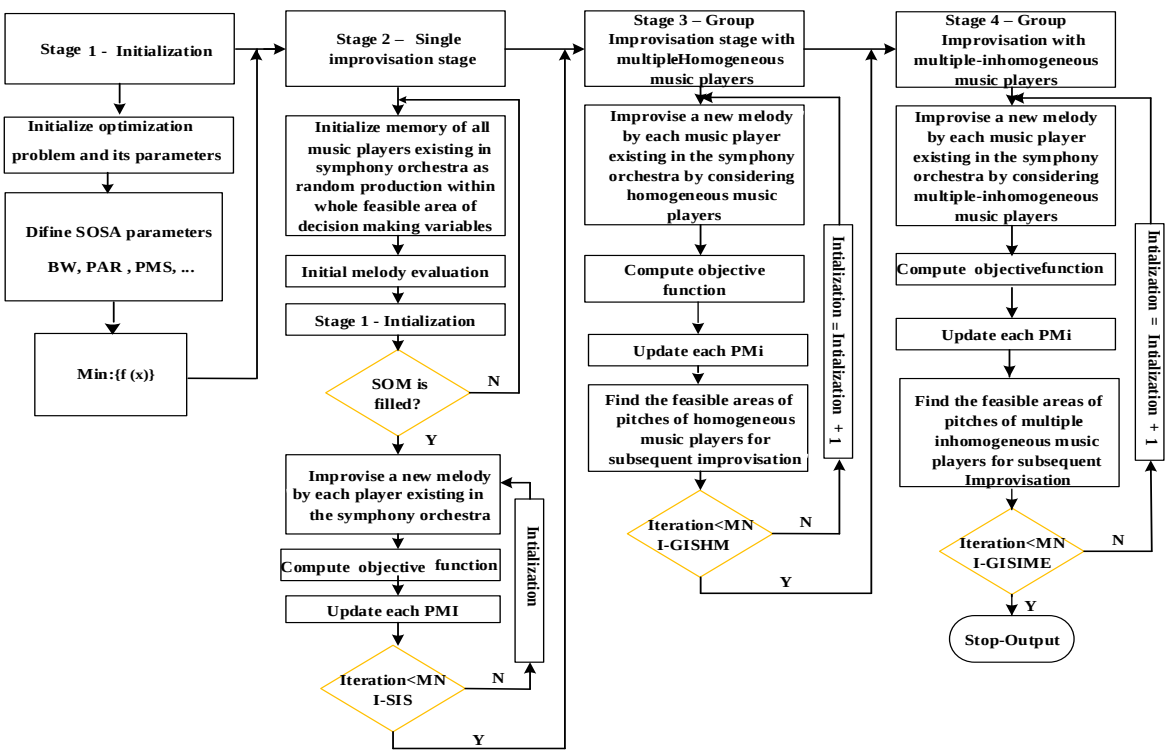

Fig. 3. The graphical representation of SOSA parameters

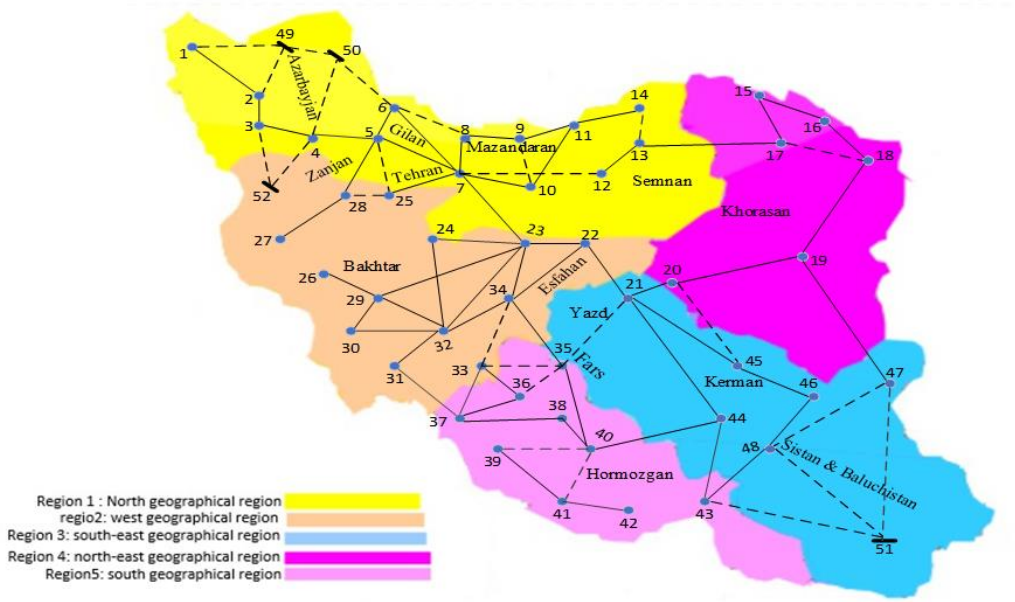

Fig. 4. 400-kV test system with 52 buses in Iran

Considering three scales of the events are reduced by 3.42%, 3.43%, and 1.66%, respectively. On the other hand, a reduction of 2.38%,0.75%, and 5.05%, in the capital cost of the transmission lines (IC^{TL}). The congestion cost (CC_{total}) is reduced by 1.75% ، 2.06%, and 0.41%. In this study, the expected profit of the generation units (EB^{GU}) has increased 0.44%, 3.56%, and 1.79%. The capital cost of all generation units (IC^{nGU}) has reduced 3.57%, 5.75%, and 5.77%. The payment capacity paid to all generation units GenCos (CAP^{GU}) so has reduced by 1.25%, 1.77%, and 3.53%. Similarly to, the comparison of the results presented in Table 5 by considering corrective actions and absence/presence ESs show that the investment costs of all transmission switches (IC^{TS}) considering the three scales of the events are reduced by 1.47%, 0.97% , and 1.17%, respectively. On the other hand, a reduction of 2.95%, 1.71%, and 1.57%, in the investment cost of the transmission lines (IC^{TL}) . The congestion cost (CC_{total}) is reduced by 1.65% ، 5.28%, and 4%. In this study, the expected profit of the generation units (EB^{GU}) has increased 3.5%, 0.48%, and 0.17%. The investment cost of generation units (IC^{nGU}) has reduced 0.55%, 1.86%, and 0.01%. The payment capacity paid to all generation units GenCos (CAP^{GU}) so has reduced by 2.48%, 0.09%, and 1.%. In additionally, depth look and comparison of the results presented in Table 3 and 5 by considering corrective actions and absence ESs show that the capital costs of transmission switches (IC^{TS}) considering three scales of the events are reduced by 91.69%, 88.97%, and 8.81%, respectively. On the other hand, a reduction of 40.87%, 39.21%, and 36.9%, in the capital cost of the transmission lines (IC^{TL}). The congestion cost (CC_{total}) is reduced by 33.61% ، 43.06%, and 47.3%. In this study, the expected profit of the generation units (EB^{GU}) has increased 1.85%, 6.83%, and 7.65%. The capital cost of generation units (IC^{nGU}) has reduced 30.95%, 16.94%, and 15.08%. The payment capacity paid to generation units GenCos (CAP^{GU}) by so has reduced 16.62%, 14.48%, and 13.01%. Similarly to, the comparison of the results presented in Table 5 by considering corrective actions and presence ESs show that the capital costs of transmission switches (IC^{TS}) considering three scales of the events are reduced by 91.52%, 10.46% , and 8.82%, respectively. On the other hand, a reduction of 41.21%,43.44%, and 34.59%, in the capital cost of the transmission lines (IC^{TL}). The congestion cost (CC_{total}) is reduced by 33.55% ، 44.93%, and 50.77%. In this study, the expected profit of the generation units (EB^{GU}) has increased 5.03%, 3.66%, and 5.57%. The capital cost of generation units has reduced 28.28%, 13.51%, and 9.86%. The payment capacity paid generation units GenCos (CAP^{GU}) so has reduced by 16.78%, 15.89%, and 17.06%. According to the results, for all three scales by applying the proposed hub and corrective ctions the expected profit tends to increase, and the installation cost tends to decrease that can improved the grid resilience. The Fig. 5(a) shows the number of generation units, transmission lines and transmission switching with the presence of the proposed EH and without considering short and long-term corrective actions in three scales. In the first scale, 19 generation units, 34 transmission lines, and 4 transmission switches are needed. In the second scale, 34 generation units, 38 transmission lines, and 41 transmission switches are needed. In third scale, 4 generation units, 4 transmission lines and 6 transmission switches are needed. Therefore, the number of elements is reduced compared to [15]. The Fig. 5(b) shows the number of generation units, transmission lines and transmission switching with the

presence of the proposed EH together with considering short and long-term corrective actions in three scales. In the first scale, 14 generation units, 15 transmission lines, and 21 transmission switches are needed. In the second scale, 18 generation units, 22 transmission lines, and 32 transmission switches are needed. In third scale, 3 generation units, 4 transmission lines and 5 transmission switches are needed. Thus, the number of elements is reduced compared to [15]. The Fig. 5(c) shows that with the proposed method, will have a significant reduction in IC^{TL}. The amount of the curtailed load in 400-kV power grid in two case (considering & ignoring corrective actions) in three scales are shown in Figs. 6(a-c).

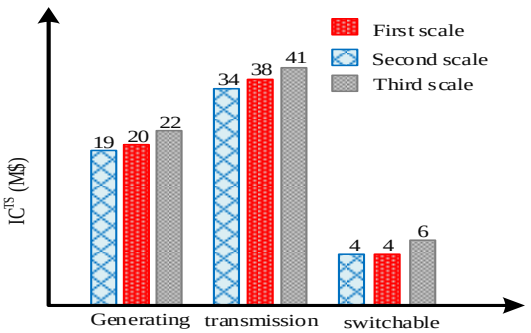

(a): Without considering short and long-term corrective actions

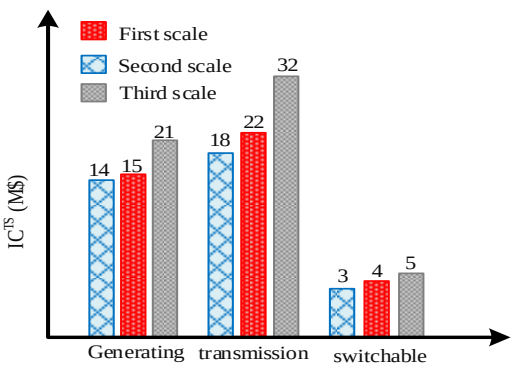

(b): With considering short and long-term corrective actions.

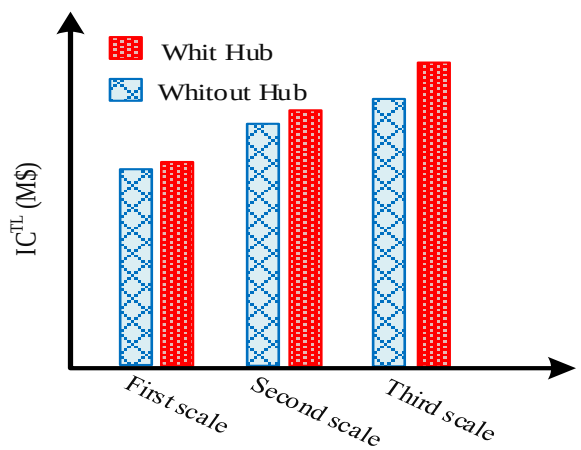

(c): Without & with considering proposed EH.

Fig. 5. Comparison of the number of elements and capital costs of transmission lines in different scales.

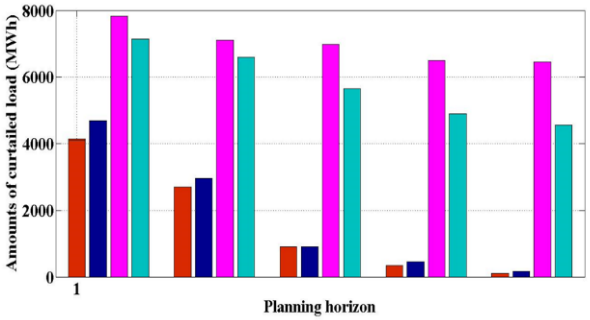

(a): First scale.

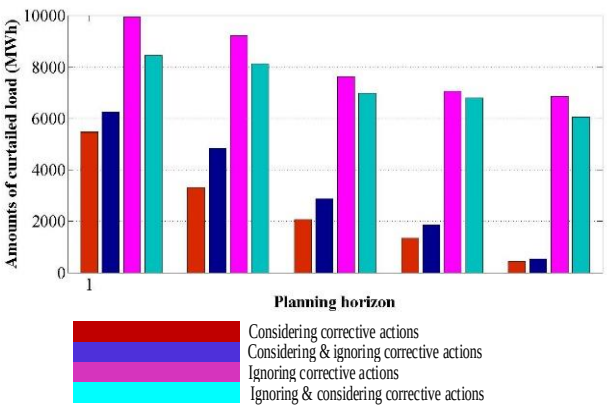

(b) second scale

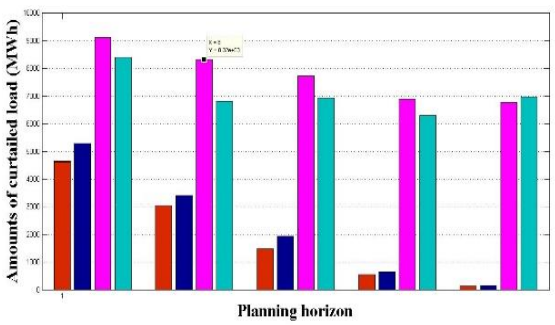

(c): third scale.

Fig. 6. The amounts of the curtailed load in different scales

TABLE 2
THE EXPANSION PLANS FOR THREE SCALES OF EARTHQUAKE BY IGNORING T CORRECTIVE ACTIONS

Planning Periods	Generating units	Transmission lines	Switchable transmission lines	Generating units	Transmission lines	Switchable transmission lines	Generating units	Transmission lines	Switchable transmission lines
period 1	9, C 17, I 43, I	(1-2), I (1-49), C (11-14), I (21-45), I (23-32), I (29-32), I (39-40), C	(35-40), I	14, C 20, C 21, I	(13-14), C (21-22), I (35-40), I (38-40), I (40-41), C (43-48), I (47-48), C	(23-34), I	5, C 9, C 11, I 18, C 48, I	(4-52), C (7-12), C (13-14), C (19-20), I (21-35), C (22-23), I (22-34), I (24-32), I (46-48), I	(31-32), I
period 2	2, I 11, I 44, C 48, I	(5-25), C (16-18), I (21-35), C (23-29), I (29-32), I (30-32), I (41-42), I		5, C 15, I 21, I 33, C 50, C	(7-8), I (10-11), I (17-18), C (23-24), I (31-32), I (35-36), C (37-38), I (46-48), I	(33-37), I	7, I 30, I 50, C 21, I 17, I	(4-50), C (7-10), I (7-23), I (11-14), I (15-17), I (27-28), I (33-34), C (8-9), I (43-48), I	(23-29), I
period 3	19, I 22, I 33, C 42, C 48, I	(4-5), I (23-24), I (31-37) , I (33-37), I (40-41), C (43-44), I (47-51), C	(38-40), I	6, I 16, I 36, C 39, C 43, I	(4-50), C (13-14), C (15-16), I (22-34), I (29-30), I (33-36), I (37-38), I (45-46), I	(18-19), I	20, C 23, C 34, I 48, I	(1-49), C (22-23), I (23-34), I (33-37), I (38-40), I (40-41), C (45-46), I (47-48), C	(31-37), I
period 4	7, I 20, C 32, I 37, I	(3-52), C (5-25), C (9-10), C (22-23), I (40-44), I (41-42), I (9-11), I	(21-44), I	1, I 2, I 20, C 50, C	(1-2), I (5-7), I (5-25), C (8-9), I (10-11), I (21-45), I (32-34), I (45-46), I	(7-25), I	25, C 36, C 39, C 48, I 50, C	(5-6), I (5-28), I (6 -50), C (7-25), I (18-19), I (21-35), C (23-34), I (29-30), I (41-42), I	(12-13), I
period 5	7, I 44, C 47, I	(3-4), I (5-7), I (9 -11), I (13-17), I (29-32), I (34-35), I (49-50), C	(33-37), I	20, C 30, I 42, C 44, C	(6-7), I (8-9), I (13-14), C (24-32), I (31-32), I (34-35), I (39-41), I (43-51), C	(7-23), I	19, I 30, I 51, C 33, C	(6-7), I (7-23), I (15-17), I (18-19), I (20-45), C (21-22), I (25-28), C (33-37), I	(9-11), I (5-7), I

TABLE 3
THE OBTAINED VALUES FOR THREE SCALES OF EARTHQUAKE BY IGNORING CORRECTIVE ACTIONS WITH PROPOSED EH

No.	Objective function	First scale without electrical and thermal storage	First scale with electrical and thermal storage	Second scale without electrical and thermal storage	Second scale with electrical and thermal storage	Third scale without electrical and thermal storage	Third scale with electrical and thermal storage
1	IC^{TL}	893.571	872.241	1105.894	1097.526	1368.182	1299.042
2	IC^{TS}	890.837	860.362	108.628	104.901	131.257	129.727
3	CC_{total}	38.0289	37.362	36.858	36.098	31.087	30.958
4	EB^{GU}	59.972	60.241	68.388	70.827	87.684	89.261
5	IC^{nGU}	450.382	431.274	506.378	477.261	637.056	600.271
6	CAP^{GU}	33.502	33.921	38.574	39.258	43.158	44.685
7	Total number	19 Generating 35 Transmission 4 Switchable	19 Generating 34 Transmission 4 Switchable	21 Generating 39 Transmission 5 Switchable	20 Generating 38 Transmission 4 Switchable	23 Generating 43 Transmission 6 Switchable	22 Generating 41 Transmission 6 Switchable

TABLE 4
THE EXPANSION PLANS FOR THREE SCALES OF EARTHQUAKE BY CONSIDERING CORRECTIVE ACTIONS

Planning Periods	Generating units	Transmission lines	Switchable transmission lines	Generating units	Transmission lines	Switchable transmission lines	Generating units	Transmission lines	Switchable transmission lines
period 1	2, I 19, I 36, C	(7-8), I (12-13), I (22-23), I (23-24), I		11, I 15, I 20, C	(8- 9), I (13-14), C (16-18), I (19-47), I (21-35), C	(21-45), I	6, I 13, C 15, I	(4-52), C (6-7), I (7-12), C (7-25), I (21-22), I (23-29), I (34-35), I (46-48), I	(24-32), I
period 2	26, C 30, I 32, I 37, I	(3-4), I (4-5), I (5-25), C	(20-21), I	11, I 13, C 46, C	(2-3), I (5-7), I (12-13), I (20-21), I (23-34), I (30-32), I	(21-44), I	4, I 14, C 26, C 43, I	(18-19), I (21-44), I (21-45), I (23-29), I (23-32), I (27-28), I	(8-9), I (12-13), I
period 3	21, I 28, I	(5-28), I (8-9), I (12-13), I	(21-45), I	15, I 37, I 41, I 48, I	(2-49), C (3-4), I (13-14), C (33-37), I		3, I 32, I 36, C 45, I	(5-25), C (10-11), I (15-17), I (19-47), I (26-29), I	
period 4	16, I 25, C 30, I	(4-50), C (7-23), I (15-17), I (18-19), I		10, C 17, I 26, C	(3-4), I (4-5), I (4-50), C (9-10), C (11-14), I	(33-35), C	6, I 7, I 27, I 35, C 44, C	(4-5), I (6-8), C (9-10), C (22-23), I (22-34), I (33-35), C (33-36), I	(11-14), I
period 5	27, I 28, I	(36-37), I (37-38), I (40-41), C (48-51), C	(19-47), I	1, I 5, C	(5-25), C (11-14), I (17-18), C (29-32), I	(23-32), I	8, C 15, I 34, I 38, I	(4-5), I (4-50), C (5-25), C (15-17), I (21-44), I (29-32), I (37-38), I	(33-37), I

TABLE 5
THE OBTAINED VALUES FOR THREE SCALES OF EARTHQUAKE BY CONSIDERING CORRECTIVE ACTIONS WITH PROPOSED EH

No	Objective function	First scale without electrical and thermal storage	First scale with electrical and thermal storage	Second scale without electrical and thermal storage	Second scale with electrical and thermal storage	Third scale without electrical and thermal storage	Third scale with electrical and thermal storage
1	IC^{TL}	528.357	512.73	672.252	660.762	863.293	849.701
2	IC^{TS}	73.985	72.893	94.852	93.927	119.682	118.274
3	CC_{total}	25.244	24.826	20.985	19.876	16.381	15.725
4	EB^{GU}	61.083	63.275	73.065	73.421	94.398	94.2376
5	IC^{nGU}	310.982	309.271	420.583	412.749	540.987	541.071
6	CAP^{GU}	27.933	28.628	32.987	33.017	37.542	37.061
7	Total number	14 Generating 18 Transmission 3 Switchable	14 Generating 18 Transmission 3 Switchable	15 Generating 24 Transmission 4 Switchable	15 Generating 22 Transmission 4 Switchable	20 Generating 33 Transmission 5 Switchable	21 Generating 32 Transmission 5 Switchable

V. Conclusions

Considering a dynamic approach enables us to make expansion decisions at different points in time, which increases the resilience of the decision-maker and reduces the investment budget required at the beginning of the planning horizon. Considering the necessity of resilience studies, our purpose is to heighten resilience of power systems by applying the proposed EH using wind turbine, with and without of ESs and employing DE algorithm and SOSA, which can be used for different optimization problems. In this paper, a nonlinear five-level CGTEP approach in large scale is proposed to minimize the capital costs and achieve the optimal solution. Several levels of simultaneous expansion planning have been implemented in this study. At the first level, system Uncertainties were modeled by taking into account the thermal energy market, a DR program, and the use of wind turbines in the proposed hub, with the goal of increasing resilience while minimizing input energy transfer costs and operating costs. The second level depicts the system operator's corrective actions following the accident to reconfigure the network. Third level earthquake events are modeled and evaluated as unknown events. At the fourth level, planning for generation planning is done with the goal of increasing resilience. The fifth level of transmission expansion planning focuses on resilience, and the ability to switch transmission lines is viewed as a low-cost correction factor. In this paper, the costs and modeling uncertainties in the optimal expansion planning in the presence of the proposed hub play an essential role in heightening resilience. The line switching maneuvers, short-term and long-term corrective actions as the resilient sources are considered to increase the power system resilience in response to variable changes of the system demand. This study has presented an optimal strategy to minimize load curtailment. On the other hand, the findings of this study compared with the previous study that the EH was ignored. The ultimate goal is to maintain system performance after events such that the system adapts itself with the events after absorbing the disruptions and reduce the consequences by fast recovery. The numerical simulations indicate the effectiveness of the proposed strategy for heightening resilience. DR programs and storage systems are known as two effective approaches to reduce the impact of uncertainties. The presence of an EH on the bus, results in changes in productive power which is the first impact on the issue. As demonstrated by the results, implementing short and long-term reactions in conjunction with concurrent generation and transmission expansion planning has been effective in strengthening resilience, minimizing costs, and increasing profits.

REFERENCES

[1] X. Luo and Y. Liu, "A multiple-coalition-based energy trading scheme of hierarchical integrated energy systems," *Sustainable Cities and Society*, vol. 64, p. 102518, 2021.

[2] S. Rahgozar, A. Z. G. Seyyedi, and P. Siano, "A resilience-oriented planning of energy hub by considering demand response program and energy storage systems," *Journal of Energy Storage*, vol. 52, p. 104841, 2022.

[3] R. Yan, T. K. Saha, F. Bai, and H. Gu, "The anatomy of the 2016 South Australia blackout: A catastrophic event in a high renewable network," *IEEE Transactions on Power Systems*, vol. 33, no. 5, pp. 5374-5388, 2018.

[4] X. Zhang, S. Mahadevan, S. Sankararaman, and K. Goebel, "Resilience-based network design under uncertainty," *Reliability Engineering & System Safety*, vol. 169, pp. 364-379, 2018.

[5] K. Ramirez-Meyers, W. N. Mann, T. Deetjen, S. Johnson, J. Rhodes, and M. Webber, "How different power plant types contribute to electric grid reliability, resilience, and vulnerability: a comparative analytical framework," *Progress in Energy*, vol. 3, no. 3, p. 033001, 2021.

[6] S. Lumbreras and A. Ramos, "The new challenges to transmission expansion planning. Survey of recent practice and literature review," *Electric Power Systems Research*, vol. 134, pp. 19-29, 2016.

[7] A. Hussain, V. H. Bui, and H. M. Kim, "Optimal operation of hybrid microgrids for enhancing resiliency considering feasible islanding and survivability," *IET Renewable Power Generation*, vol. 11, no. 6, pp. 846-857, 2017.

[8] G. Jayadev, B. D. Leibowicz, and E. Kutanoglu, "US electricity infrastructure of the future: Generation and transmission pathways through 2050," *Applied energy*, vol. 260, p. 114267, 2020.

[9] S. M. Mohseni-Bonab, I. Kamwa, A. Rabiee, and C. Chung, "Stochastic optimal transmission Switching: A novel approach to enhance power grid security margins through

vulnerability mitigation under renewables uncertainties," *Applied Energy*, vol. 305, p. 117851, 2022.

[10] C. A. Sima, M. O. Popescu, C. L. Popescu, M. Alexandru, and G. Lazaroiu, "Increasing RESS share using generation and transmission expansion planning-stochastic approach," in *2019 11th International Symposium on Advanced Topics in Electrical Engineering (ATEE)*, 2019: IEEE, pp. 1-6.

[11] S. A. Eghbali Khob, M. Moazzami, and R. Hemmati, "Advanced model for joint generation and transmission expansion planning including reactive power and security constraints of the network integrated with wind turbine," *International Transactions on Electrical Energy Systems*, vol. 29, no. 4, p. e2799, 2019.

[12] X. Yang, Z. Chen, X. Huang, R. Li, S. Xu, and C. Yang, "Robust capacity optimization methods for integrated energy systems considering demand response and thermal comfort," *Energy*, vol. 221, p. 119727, 2021.

[13] A. Ahmarinejad, "A multi-objective optimization framework for dynamic planning of energy hub considering integrated demand response program," *Sustainable Cities and Society*, vol. 74, p. 103136, 2021.

[14] T. Xu, C. Shao, M. Shahidehpour, and X. Wang, "Coordinated Planning Strategies of Power Systems and Energy Transportation Networks for Resilience Enhancement," *IEEE Transactions on Sustainable Energy*, 2022.

[15] M. Shivaie, M. Kiani-Moghaddam, and P. D. Weinsier, "A vulnerability-constrained quad-level model for coordination of generation and transmission expansion planning under seismic-and terrorist-induced events," *International Journal of Electrical Power & Energy Systems*, vol. 120, p. 105958, 2020.

[16] W. Gan *et al.*, "A tri-level planning approach to resilient expansion and hardening of coupled power distribution and transportation systems," *IEEE Transactions on Power Systems*, vol. 37, no. 2, pp. 1495-1507, 2021.

[17] Y.-P. Fang, C. Fang, E. Zio, and M. Xie, "Resilient critical infrastructure planning under disruptions considering recovery scheduling," *IEEE Transactions on Engineering Management*, vol. 68, no. 2, pp. 452-466, 2019.

[18] Y. Wang, A. O. Rousis, and G. Strbac, "A Three-Level Planning Model for Optimal Sizing of Networked Microgrids Considering a Trade-Off Between Resilience and Cost," *IEEE Transactions on Power Systems*, vol. 36, no. 6, pp. 5657-5669, 2021.

[19] K. Yurtseven and E. Karatepe, "Influence of inherent characteristic of PV plants in risk-based stochastic dynamic substation expansion planning under MILP framework," *IEEE Transactions on Power Systems*, vol. 37, no. 1, pp. 750-763, 2021.

[20] C. Guo, C. Ye, Y. Ding, and P. Wang, "A multi-state model for transmission system resilience enhancement against short-circuit faults caused by extreme weather events," *IEEE Transactions on Power Delivery*, vol. 36, no. 4, pp. 2374-2385, 2020.

[21] Y.-K. Wu, Y.-C. Chen, H.-L. Chang, and J.-S. Hong, "The effect of decision analysis on power system resilience and economic value during a severe weather event," *IEEE Transactions on Industry Applications*, vol. 58, no. 2, pp. 1685-1695, 2022.

[22] Y.-K. Wu, Y.-C. Wu, H.-L. Chang, and J.-S. Hong, "Using Extreme Wind-Speed Probabilistic Forecasts to Optimize Unit Scheduling Decision," *IEEE Transactions on Sustainable Energy*, vol. 13, no. 2, pp. 818-829, 2021.

[23] T. Hussain, S. Suryanarayanan, T. M. Hansen, and S. S. Alam, "A Fast and Scalable Transmission Switching Algorithm for Boosting Resilience of Electric Grids Impacted by Extreme Weather Events," *IEEE Access*, 2022.

[24] D. N. Trakas and N. D. Hatziargyriou, "Strengthening transmission system resilience against extreme weather events by undergrounding selected lines," *IEEE Transactions on Power Systems*, vol. 37, no. 4, pp. 2808-2820, 2021.

[25] M. Abdelmalak and M. Benidris, "Enhancing power system operational resilience against wildfires," *IEEE Transactions on Industry Applications*, vol. 58, no. 2, pp. 1611-1621, 2022.

[26] M. Abdelmalak and M. Benidris, "Proactive Generation Redispatch to Enhance Power System Resilience During Hurricanes Considering Unavailability of Renewable Energy Sources," *IEEE Transactions on Industry Applications*, vol. 58, no. 3, pp. 3044-3053, 2022.

[27] H. Ranjbar, S. H. Hosseini, and H. Zareipour, "Resiliency-oriented planning of transmission systems and distributed energy resources," *IEEE Transactions on Power Systems*, vol. 36, no. 5, pp. 4114-4125, 2021.

[28] Y. Yang, J. C.-H. Peng, C. Ye, Z.-S. Ye, and Y. Ding, "A criterion and stochastic unit commitment towards frequency resilience of power systems," *IEEE transactions on power systems*, vol. 37, no. 1, pp. 640-652, 2021.

[29] K. Garifi, E. S. Johnson, B. Arguello, and B. J. Pierre, "Transmission Grid Resiliency Investment Optimization Model with SOCP Recovery Planning," *IEEE Transactions on Power Systems*, vol. 37, no. 1, pp. 26-37, 2021.

[30] H. Nemati, M. A. Latify, and G. R. Yousefi, "Coordinated generation and transmission expansion planning for a power system under physical deliberate attacks," *International Journal of Electrical Power & Energy Systems*, vol. 96, pp. 208-221, 2018.

[31] Y. Fang and G. Sansavini, "Optimizing power system investments and resilience against attacks," *Reliability Engineering & System Safety*, vol. 159, pp. 161-173, 2017.

[32] M. Zeraati, Z. Aref, and M. A. Latify, "Vulnerability analysis of power systems under physical deliberate attacks considering geographic-cyber interdependence of the power system and communication network," *IEEE Systems Journal*, vol. 12, no. 4, pp. 3181-3190, 2017.

[33] N. M. Tabatabaei, S. N. Ravadanegh, and N. Bizon, *Power Systems Resilience*. Springer, 2018.

[34] M. Vahid-Pakdel, S. Nojavan, B. Mohammadi-Ivatloo, and K. Zare, "Stochastic optimization of energy hub operation with consideration of thermal energy market and demand response," *energy Conversion and Management*, vol. 145, pp. 117-128, 2017.

[35] R. Alvarez, C. Rahmann, R. Palma-Behnke, and P. Estévez, "A novel meta-heuristic model for the multi-year transmission network expansion planning," *International Journal of Electrical Power & Energy Systems*, vol. 107, pp. 523-537, 2019.

[36] M. Kiani-Moghaddam, M. Shivaie, and P. D. Weinsier, *Modern Music-Inspired Optimization Algorithms for Electric Power Systems*. Springer, 2019.

[37] M. T. Askari, M. Z. A. A. Kadir, M. Tahmasebi, and E. Bolandifar, "Modeling optimal long-term investment strategies of hybrid wind-thermal companies in restructured power market," *Journal of Modern Power Systems and Clean Energy*, vol. 7, no. 5, pp. 1267-1279, 2019.

[38] T. Lagos *et al.*, "Identifying optimal portfolios of resilient network investments against natural hazards, with applications to earthquakes," *IEEE Transactions on Power*

Systems, vol. 35, no. 2, pp. 1411-1421, 2019.
[39] M. Askari, M. Ab Kadir, H. Hizam, and J. Jasni, "A new comprehensive model to simulate the restructured power market for seasonal price signals by considering on the wind resources," *Journal of Renewable and Sustainable Energy*, vol. 6, no. 2, p. 023104, 2014.
[40] J. Märkle-Huß, S. Feuerriegel, and D. Neumann, "Cost minimization of large-scale infrastructure for electricity generation and transmission," *Omega*, vol. 96, p. 102071, 2020.
[41] J. Aghaei, N. Amjady, A. Baharvandi, and M.-A. Akbari, "Generation and transmission expansion planning: MILP–based probabilistic model," *IEEE Transactions on Power Systems*, vol. 29, no. 4, pp. 1592-1601, 2014.
[42] M. Hosseini, R. Mirzaei, and S. S. Kourehli, "International Institute of Earthquake Engineering and Seismology."

APPENDIX

Input parameters for simulation.

PARAMETER ADJUSTMENT OF THE OPTIMIZATION

Abbreviation	SOSA parameters	Value
BW	distance bandwidth	$\in \mathrm{R}^{(\mathrm{N})} > 0$
MNI - E	Max. number of iterations for second step	MNI - E ≥ 1
MNI - SIS	Max. number of iterations for third step	MNI - SIS ≥ 1
MNI - GISHMG	Max. number of iterations for fourth step	MNI - GISHMG ≥ 1
MNI - GISIME	Max. number of iterations for fifth step	MNI - GISIME ≥ 1
NHMG	Number of decision-making variables	NHMG ≥ 1
PAR	pitch adjusting rate	$0 \leq PAR \leq 1$
$PMCR$	Player memory considering rate	$0 \leq PMCR \leq 1$
PMS	Player memory size	$PMS \geq 1$
PMN	Player memory number	$PMN \geq 1$
MM	Melody memory	-

THE PROPOSED EH PARAMETERS

EH Parameters	Unit	Value	EH Parameters	Unit	Value
η_{GH}^{B}	-	0.85	$\alpha_{H}^{\min}$	-	0.05
P_{E}^{NETMAX}	KW	2000	$\alpha_{H}^{\max}$	-	0.90
P_{G}^{NET}	KW	1800	$\beta_{E}^{\min}$	-	0.05
P_{H}^{NET}	KW	2000	$\beta_{E}^{\max}$	-	0.18
P_{in}^{T}	KW	2000	$\beta_{H}^{\min}$	-	0.05
P_{in}^{CHP}	KW	800	$\beta_{H}^{\max}$	-	0.09
P_{in}^{B}	KW	800	P_{E}^{CAP}	KW	300
α_{E}^{LOSS}	-	0.05	P_{H}^{CAP}	KW	200
α_{H}^{LOSS}	-	0.05	η_{ES}^{ch}	-	0.90
$\alpha_{E}^{\min}$	-	0.05	η_{ES}^{dis}	-	0.90
$\alpha_{E}^{\max}$	-	0.90	η_{HS}^{ch}	-	0.90
v_{out}	m/s	22	v_{r}	m/s	10
Weilbullscale	-	7.87	$\mathrm{LPF}_{\mathrm{down}}^{H}$	-	0.20
η_{GE}^{CHP}	-	0.40	η_{E}^{T}	-	0.90
v_{in}	m/s	4	P_{r}^{WIND}	KW	400
$\mathrm{LPF}_{\mathrm{up}}^{H}$	-	0.20	*Weilbullscale*	-	1.75
π_{E}^{WIND}	Cent/kWh	0	π_{G}^{NET}	Cent/kWh	7.2
π_{H}^{NET}	Cent/kWh	8	π_{E}^{op}	Cent/kWh	0
π_{H}^{op}	Cent/kWh	2	π_{E}^{D}	Cent/kWh	0
π_{H}^{D}	Cent/kWh	0	η_{CONV}^{WIND}	-	0.90
η_{HS}^{dis}	-	0.90	-	-	-

Mahnaz Rezaei was born in Iran in 1988. She received the B.S. degree in electrical engineering from Zahedan Branch Islamic Azad University, Iran in 2010. In 2015, she received the M.Sc. degree in Power electrical engineering, Zahedan Branch Islamic Azad University. She is currently Ph.D candidate in Power Electrical Engineering from Islamic Azad University (Semnan Branch). Her research interests include smart grids, GEP & TEP.

Mohammad Tolou Askari enrolled at University of Applied Science and Technology of Mashhad and obtained his first degree in Bachelor of Power Electrical Engineering in 2005. He continued his education in Master of Power Electrical Engineering in 2008. He received PhD degree in Power electrical engineering (2014) from University Putra Malaysia. Currently, he is Assistant Professor with Islamic Azad University, Semnan, Iran. His research interests include electrical transformers, Smart grids, Micro grids, GEP & TEP, Distribution systems.

Meysam Amirahmadi received the B.Sc. degree in electrical engineering from Guilan University, Rasht, Iran, in 2006 and M.Sc., and Ph.D. degrees in electrical engineering from Semnan University, Semnan, Iran, in 2009 and 2014, respectively. He is currently an Assistant Professor with Islamic Azad University, Semnan, Iran. His research interests include power system planning and operation, electricity markets and smart grids.

Vahid Ghods was born in Iran in 1981. He received the B.S. degree in electronic engineering from Electrical Engineering Faculty, K. N. Toosi University of technology (KNTU), Tehran, Iran, in 2002. In 2005, he received M.Sc. degree in digital electronic from Electrical Engineering Faculty, Semnan University, Semnan, Iran. He received Ph.D. degree in electronic from Electrical Engineering Faculty, Science and research branch, Islamic Azad University, Tehran, Iran, in 2012. He is an associate professor of Engineering Faculty, Semnan branch, Islamic Azad University, Semnan, Iran. His research fields are signal processing, machine vision, image and speech processing and recognition, artificial intelligence and specially OCR.

International Journal Of
Industrial Electronics Control and Optimization
Print ISSN: 3517-2645
Online ISSN: 3568-2645
Homepage: https://ieco.usb.ac.ir/

On-Line Detection of Harmonic Components in Magnet Defect Fault of Permanent Magnet Synchronous Motor through a Modified Prony's Method

Morteza Ghaseminezhad | Morteza Jadidoleslam

Department of Electrical Engineering, Sirjan University of Technology, Sirjan, Iran [1,2]
Corresponding author's email: mghaseminejad@sirjantech.ac.ir

Article Info

Article type:
Research Article

Article history:
Received: 2022–July-21
Received in revised form 2023-Jan-30
Accepted: 2023-Feb-03
Published online: 2023-Feb-20

Keywords:
Fault detection,
PMS motor,
Magnet defect,

ABSTRACT

The use of permanent magnets in the structure of electric machines, in addition to simplifying design and construction by reducing losses, leads to increased efficiency in the motor. However, the magnetic material can be damaged by failure caused by faults such as short circuits in the electronic driver of the motor. Magnets containing samarium and neodymium are completely brittle and easy to crack. These elements are also very vulnerable due to their crystalline structure and grain texture. Magnet defect fault is one of the most common faults in permanent magnet machines. In this paper, a permanent magnet synchronous motor (PMSM) with a magnet defect fault is simulated using the finite element method. Moreover, Prony's method is modified by the matrix pencil method for the estimation of the component created in the stator current. The frequency spectrum of magnetic flux density and stator current in both faulty and healthy modes are extracted and fault detection is done through a modified Prony's method.

I. Introduction

The removal of the excitation coil and the use of a permanent magnet in synchronous motors increase efficiency and improve dynamic performance. By removing the brushes and slip rings, the copper losses of the field are reduced, which is the most important advantage of these motors. Permanent magnet synchronous motors (PMSM) are highly efficient due to low rotor losses and low magnetizing current. The simplicity of the motor design and construction and the high power-to-volume ratio are the main advantages of these motors [1].

Although due to the high price of permanent magnets, the price of these motors is higher than the dc excitation type, they are used in industrial applications such as pumps, compressors and centrifuges because of their advantages such as high efficiency, good power factor and low sensitivity to changes in voltage and frequency of supply [2]. Other uses for these motors include applications in medicine, aerospace, textile and petrochemical industries, and instrumentation. In addition to industrial applications, PMSMs are also widely employed in the military and telecommunications industries. Permanent magnet propulsion motors are extensively used in submarines [3].

Faults in electrical machines, whether mechanical, electrical, or magnetic, can lead to larger faults and sometimes irreparable damage if not detected in the early stages; therefore, knowing the types of faults and ways to detect them in every electric motor is essential. Electric motor faults sometimes occur due to inherent defects. These inherent defects may be due to impurities in the raw material in the machine, such as magnet impurities in permanent magnet machines. Moreover, structural defects of the machine which occur due to defects in the manufacture and

production of parts, are among the inherent defects of the machine. Other inherent defects include physical asymmetries in the machine structure and winding insulation defects during construction. Each of these inherent defects increases the likelihood of other faults occurring in the machine. The occurrence of any fault in the magnet has significant effects on the output of the machine because the magnet is the most crucial component of the excitation part of the permanent magnet machine [4-6]. Faults in the magnet are considered magnetic faults. The frequency of these faults is less than mechanical and electrical faults, but their significance warrants special attention. The magnetic material can be damaged by failure caused by faults such as short circuits in the electronic driver of the motor. Magnets containing samarium and neodymium are completely brittle and easy to crack. These elements are very vulnerable due to their crystal structure and grain texture. The centrifugal force on the surface magnets and the increase in heat lead to damage and the breakage of these magnets [5].

In recent years, fault detection and preventive maintenance aimed at preventing major faults in motors have been considered by many researchers [7-10]. In general, there are two basic logics for diagnosing defects in electric machines; one is fault detection, which involves finding a fault in the machine, and the other is fault diagnosis, which indicates the type of fault created in the machine and its severity. So far, many destructive and non-destructive detection methods have been proposed to detect faults in electric machines. Non-destructive detection methods are based on simple and inexpensive measurements and do not require changing the structure of the motor. Motor current signature analysis and the analysis of the ac component of power signal are non-destructive fault detection methods [11-15]. Temperature analysis using sensors inside the motor is a destructive method of fault detection.

In [16], for the magnet defect analysis of PMSM, 7% of the magnet has been removed, which is a significant amount and its components have been obtained by using Discrete Fourier Transform (DFT). In practice, the crack created in the magnet is small and will has less effect on the amplitude of the components created in the induced voltage and stator current. To obtain the amplitude of these components, the DFT is not a suitable tool. Many harmonic estimation techniques have been identified and used in the field of signal processing of fault diagnosis.

One of these techniques is classical multiple signal classification (MUSIC)[17]. Although the MUSIC method is a powerful tool for high-resolution frequency detection, it has long computational time constraints from a short noisy data recording signal. It is also difficult to estimate the amplitude. To improve these major issues, a new method is proposed in [18]. This method uses a well-known approach, namely the estimation of signal parameters via rotation invariance technique (ESPRIT). ESPRIT results in more accurate frequency estimates than MUSIC. In this method, the corresponding amplitude of harmonic frequencies is obtained using least squares (LS). Despite the good results of the LS algorithm, amplitude/frequency tracking is still difficult for this method.

Prony analysis (PA) is one of the best interesting techniques to estimate the harmonic frequencies of a signal. Prony's approach provides higher frequency resolution than other approaches due to its confidence in autoregressive analysis. In [19, 20], Prony's method for the estimation of the frequencies of broken rotor faults of the induction motor has been presented. In this approach, the least squares algorithm is used for the estimation of the harmonic frequencies. As previously mentioned, amplitude/frequency tracking is still challenging for this method.

In our paper, to overcome these drawbacks, Prony's method is modified by using the matrix pencil method for the estimation of the component created in the stator current. When there is no fault in the motor, some inherent fault effects can be observed in the signals. By using this method, the possibility of mistaking the components caused by the fault with the components caused by other factors is minimized, because it is possible to estimate all frequency components with very high accuracy.

II. PRONY'S METHOD

A. *Prony's method*

Prony's method is a technique for extracting sinusoidal signals or exponentials from temporal data by solving a set of linear equations. Assuming x (t) and N signals of the complex sample, Prony's method estimates the sampling data with the linear combination of the p complex exponential function [21].

$$x\left[n\right]=\sum_{k=1}^{p}h_k z_k^{n-1}$$

$$z_k=e^{(\alpha_k+j2\pi f_k)T_s}\quad h_k=A_K e^{j\phi_k} \tag{1}$$

where T_s is the sampling time, and $A_K, f_k, \phi_k, \alpha_k$ are amplitude, frequency, angle and the damping factor of the k^{th} components, respectively. The above equation is a complex nonlinear problem that can be solved using Prony's method. In fact, Prony's method converts nonlinear problem estimation parameters into a linear system and calculates polynomial roots. For this objective, Prony's method forms a homogeneous linear differential equation with constant coefficients.

$$\sum_{k=0}^{p}a_k x\left[n-k\right]=0 \tag{2}$$

In the classical Prony's method, the number of the available data samples is considered to be equal to the number of the sample of the unknown model. However, in many practical cases N > 2p and, in this way, equation (2) should be modified. In this paper, the matrix pencil method is used to directly obtain z_k by solving a generalized eigenvalue problem.

B. Matrix pencil method

In this paper, to perform the matrix pencil method, a rectangular Hankel matrix Y is created from the signal x[n].

$$Y = \begin{bmatrix} x[1] & \cdots & x[p] & x[p+1] \\ \vdots & \vdots & \vdots & \vdots \\ \vdots & \vdots & \vdots & \vdots \\ x[N-p] & \cdots & x[N-1] & x[N] \end{bmatrix} \quad (3)$$

This matrix is used to construct matrices Y_2 and Y_1. Y_2 is created by eliminating the first column of Y, while Y_1 is formed by eliminating the last column of Y. It is more effective to obtain the values of z_k from the following phrase:

$$z_k = eigenvalues(Y_1^{+} Y_2) \quad (4)$$

where $Y_1^{+}1$ is the Moore-Penrose pseudoinverse matrix of Y_1, defined as:

$$Y_1^{+} = \left[Y_1^{H} Y_1\right]^{-1} Y_1^{H} \quad (5)$$

A polynomial with roots z_k can be created using the linear prediction parameters as follows:

$$F(z) = \sum_{k=0}^{p} a_k z^{(p-k)} \quad (6)$$

As a result, the frequency and the damping factor can be directly obtained from the roots z_k of (4):

$$a_k = \frac{ln|z_k|}{T_s}$$
$$f_k = \frac{1}{2\pi T_s} tan^{-1}\left[\frac{Im(z_k)}{Re(z_k)}\right] \quad (7)$$

III. SIMULATION RESULTS

There are several methods to model a PMSM, and the finite element method is one of the best. Using this method, first the study area is divided into a large number of smaller areas called meshes. Then the desired electromagnetic equations in each mesh are solved by numerical methods to finally obtain the distributed magnetic vector potential (A) in the whole area. With (A), the flux density distribution can be easily calculated. In order to analyze the fault of the defect magnet, using the two-dimensional finite element method, the model is divided into a number of finite elements and the following Maxwell equations are solved in each element [5]:

$$\nabla \times \left(\frac{1}{\mu}\nabla \times A\right) = J + \nabla \times H_C$$
$$\nabla \times E = -\frac{dB}{dt} \quad (8)$$

In this section, the simulation of a synchronous permanent magnet motor in Maxwell software is investigated. For this purpose, first a healthy motor is analyzed and then by adding cracks on the magnets, the simulation results are compared with the healthy motor results. Figure 1 displays the meshing in the Maxwell 2D model. The parameters of the simulated motor are given in Table 1.

TABLE 1
PERMANENT MAGNET SYNCHRONOUS MOTOR PARAMETERS

Quantity	Name of Unit
Number of poles	4
Speed	1500
Voltage	220
Outer diameter of the stator	120mm
Outer diameter of the rotor	74mm
Rotor length	65mm

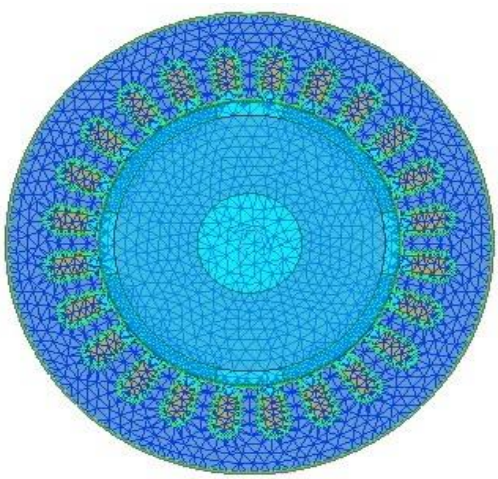

Fig. 1. Synchronous motor meshing in Maxwell.

The finite element (FE) method is used for analyzing the PMSM with a magnet defect. One crack is created, which is 0.049 mm wide along the magnet. (0.25% of the magnet is removed). Electrical and mechanical variables such as current, voltage, flux, and torque, are ideal waveforms for fault detection. Among these signals, stator current is a non-invasive fault detection procedure. In the case of a broken magnet, the unevenness of the air gap flux density causes a number of harmonics to flow through the stator windings. When a fault occurs in the magnet, they have a

significant effect on the flux density. Figure 2 shows the flux density of one point in the air gap in the normal state (a) and the defect of the magnet (b).

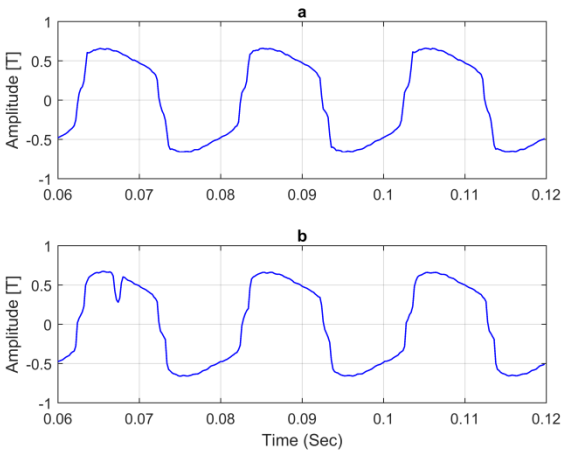

Fig. 2. The flux density of one point in the air gap in the normal state (a) and the defect of the magnet (b).

Using modified Prony's method, the frequency components of the flux density waveform have been estimated. Figure 3 shows the frequency spectrum of the flux density of one point in the air gap in the normal state (a) and the defect of the magnet (b).

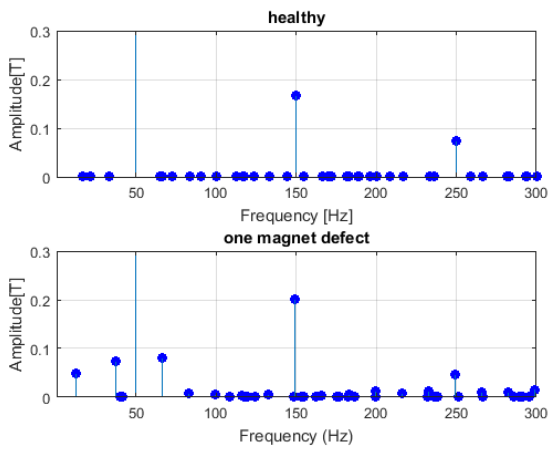

Fig. 3. The frequency spectrum of the flux density of one point in the air gap in the normal state (a) and the defect of the magnet (b).

After several simulations, it was found that the most effective harmonics in the flux density spectrum are the 0.25^{th}, 0.5^{th} and 0.75^{th} harmonics. Other components are also affected, but not as much as these three harmonics. The behavior of these harmonics shows that they are more dependent on speed than torque. But, for these selected harmonics, which are located at the bottom of the main components, the number of slots has a greater impact on the components. As a result of this fault, the fourth and second harmonics had the greatest change compared to other harmonics. The effect of this fault on the sidebands of the second, third, and fourth harmonics is also significant.

Figure 4 depicts the frequency spectrum of the stator current waveform in the normal state (a) and the magnet defect (b).

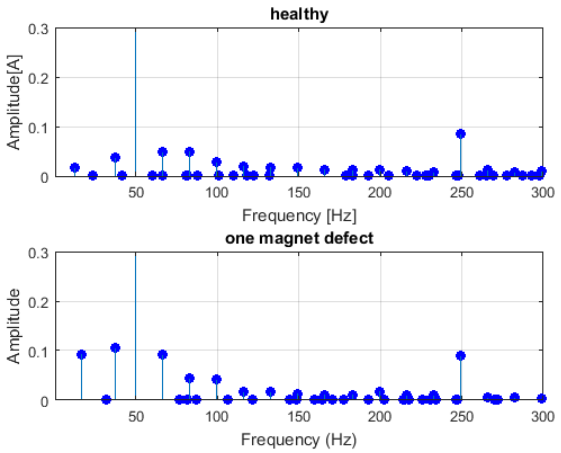

Fig. 4. The frequency spectrum of the the stator current in the normal state (a) and the defect of the magnet (b).

Simulations have been performed in different modes, and the results have shown that in the stator current spectrum, 0.25^{th} and 0.5^{th} harmonics had the most change compared to other harmonics. The effect of this fault on the sidebands of the second, third and fourth harmonics is also significant. Within this frequency range, the left sideband of the third harmonic is affected the most. The fourth and second harmonics can also be introduced as indicators of other faults due to significant changes in their harmonic amplitude during the fault; however these two components show similar behavior in other faults.

The harmonic behavior of the 0.5^{th} harmonic also shows that it is highly dependent on speed. The changes in these two harmonics in the induced voltage are similar to the components in the stator current. The amplitude of these two components increases with increasing the gap and, in all cases, can be identified using these two components. Although the parameters of the motor, the shape of the stator winding, and the change in the load torque affect the current spectrum, according to the simulations performed in this study, the 0.25^{th} and 0.5^{th} harmonics are predominant components in the detection of magnet defect fault, and they are more trustworthy. Other components do not seem as reliable.

To compare Prony's method modified by the matrix pencil approach with the method presented in [21], the least squares and the matrix pencil methods along with the Prony's method have been used to estimate the waveform of the flux density of one point in the air gap under fault conditions. Figure 5 indicates the comparison of these two methods. As it is clear, modified Prony's method results in a considerably better

estimate for the same p-values than the Prony's method based on the least squares algorithm.

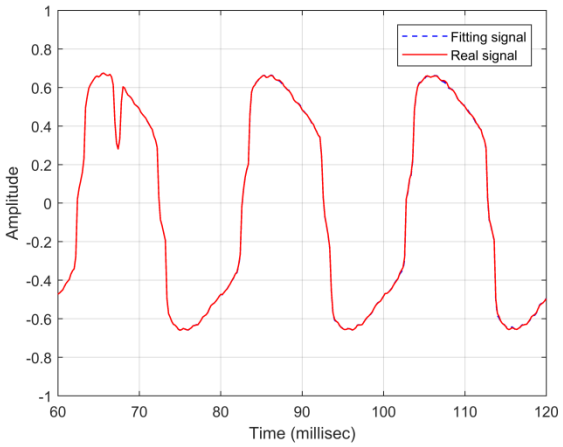

Fig. 5. The flux density of one point in the air gap estimated by modified Prony's method.

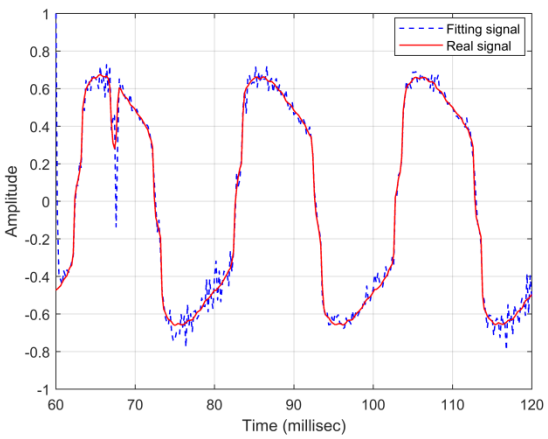

Fig. 6. The flux density of one point in the air gap estimated by the method presented in [21].

IV. Conclusions

According to the results obtained from the simulation in Maxwell software, creating cracks and fissures in the magnet can affect the performance of the motor. Using modified Prony's method, the frequency components of the flux density and stator current have been estimated.

Simulations have been performed in different modes, and the results have shown that in the stator current spectrum, 0.25^{th} and 0.5^{th} harmonics had the greatest change compared to other harmonics. The effect of this fault on the sidebands of the second, third, and fourth harmonics is also significant. Within this frequency range, the left band of the third harmonic is affected the most. The second and fourth harmonics can also be introduced as indicators of other faults due to significant changes in their harmonic amplitude during the fault; however, these two components show similar behavior in other faults. Comparing the healthy model with the defective models, we conclude that although the parameters of the motor, the shape of the stator winding and the change in the load torque affect the current spectrum, according to the simulations performed in this study, the 0.25^{th} and 0.5^{th} harmonics are more dominant and reliable components in the detection of magnetic defect fault. Other components do not seem as reliable.

References

[1] A. U. Ganesan and L. N. Chokkalingam, "Review on the evolution of technology advancements and applications of line - start synchronous machines," IET Electric Power Applications, vol. 13, no. 1, pp. 1-16, 2019.

[2] D. Fonseca, C. M. Santos, and A. J. M. Cardoso, "Stator faults modeling and diagnostics of line-start permanent magnet synchronous motors," IEEE Transactions on Industry Applications, vol. 56, no. 3, pp. 2590-2599, 2020.

[3] M. S. Rafaq et al., "A Simple Method for Identifying Mass Unbalance Using Vibration Measurement in Permanent Magnet Synchronous Motors," IEEE Transactions on Industrial Electronics, vol. 69, no. 6, pp. 6441-6444, 2021.

[4] S. R. Mousavi-Aghdam and A. Kholosi, "Design and Analysis of a New Topology of Rotor Magnets in Brushless DC Motors to Reduce Cogging Torque " International Journal of Industrial Electronics Control and Optimization, vol. 4, no. 1, pp. 77-86, 2021.

[5] M. S. Rafaq et al., "Airgap search coil based identification of pm synchronous motor defects," IEEE Transactions on Industrial Electronics, vol. 69, no. 7, pp. 6551-6560, 2021.

[6] R. Yazdanpanah, "Portable Power Generation System: Axial Flux PM Generator Design " International Journal of Industrial Electronics Control and Optimization, vol. 3, no. 1, pp. 11-18, 2020.

[7] Z. Dogan and K. Tetik, "Diagnosis of inter-turn faults based on fault harmonic component tracking in LSPMSMs working under nonstationary conditions," IEEE Access, vol. 9, pp. 92101-92112, 2021.

[8] K. N. Gyftakis, S. Ab Rasid, G. A. Skarmoutsos, and M. Mueller, "The demagnetization harmonics generation mechanism in permanent magnet machines with concentrated windings," IEEE Transactions on Energy Conversion, vol. 36, no. 4, pp. 2934-2944, 2021.

[9] W. Huang et al., "Current-based open-circuit fault diagnosis for PMSM drives with model predictive control," IEEE Transactions on Power Electronics, vol. 36, no. 9, pp. 10695-10704, 2021.

[10] G. A. Skarmoutsos, K. N. Gyftakis, and M. Mueller, "Analytical Prediction of the MCSA Signatures Under Dynamic Eccentricity in PM Machines With Concentrated Non-Overlapping Windings," IEEE Transactions on Energy Conversion, vol. 37, no. 2, pp. 1011-1019, 2021.

[11] T. Amanuel, A. Ghirmay, H. Ghebremeskel, R. Ghebrehiwet, and W. Bahlibi, "Design of Vibration Frequency Method with Fine-Tuned Factor for Fault Detection of Three Phase Induction Motor," Journal of Innovative Image Processing, vol. 3, no. 01, pp. 52-65, 2021.

[12] P. Gangsar and R. Tiwari, "Signal based condition monitoring techniques for fault detection and diagnosis of

induction motors: A state-of-the-art review," Mechanical systems signal processing, vol. 144, pp. 106-908, 2020.
[13] O. E. Hassan, M. Amer, A. K. Abdelsalam, and B. W. Williams, "Induction motor broken rotor bar fault detection techniques based on fault signature analysis–a review," IET Electric Power Applications, vol. 12, no. 7, pp. 895-907, 2018.
[14] M. Mostafaei and J. Faiz, "An overview of various faults detection methods in synchronous generators," IET Electric Power Applications, vol. 15, no. 4, pp. 391-404, 2021.
[15] H. Wang, S. Lu, G. Qian, J. Ding, Y. Liu, and Q. Wang, "A two-step strategy for online fault detection of high-resistance connection in BLDC motor," IEEE Transactions on Power Electronics, vol. 35, no. 3, pp. 3043-3053, 2019.
[16] M. Zafarani, T. Goktas, and B. Akin, "A comprehensive analysis of magnet defect faults in permanent magnet synchronous motors," in 2015 IEEE Applied Power Electronics Conference and Exposition (APEC), 2015, pp. 2779-2783: IEEE.
[17] Z. Wang et al., "Amplitude-Identifiable MUSIC (Aid-MUSIC) for Asynchronous Frequency in Blade Tip Timing," IEEE Transactions on Industrial Informatics, 2022.
[18] Y.-H. Kim, Y.-W. Youn, D.-H. Hwang, J.-H. Sun, and D.-S. Kang, "High-resolution parameter estimation method to identify broken rotor bar faults in induction motors," IEEE Transactions on Industrial Electronics, vol. 60, no. 9, pp. 4103-4117, 2012.
[19] M. Sahraoui, A. J. M. Cardoso, and A. Ghoggal, "The use of a modified prony method to track the broken rotor bar characteristic frequencies and amplitudes in three-phase induction motors," IEEE Transactions on Industry Applications, vol. 51, no. 3, pp. 2136-2147, 2014.
[20] W. Dehina, M. Boumehraz, and F. Kratz, "On - line detection and estimation of harmonics components in induction motors rotor fault through a modified Prony's method," International Transactions on Electrical Energy Systems, vol. 31, no. 2, p. e12737, 2021.
[21] K. Yahia, M. Sahraoui, A. J. M. Cardoso, and A. Ghoggal, "The use of a modified Prony's method to detect the airgap-eccentricity occurrence in induction motors," IEEE Transactions on Industry Applications, vol. 52, no. 5, pp. 3869-3877, 2016.

Morteza Ghaseminezhad received the B.Sc. degree from Electrical Engineering Department of Shahid Bahonar University, Kerman, Iran, in 2007 and the M.Sc. and the Ph.D. degree in electrical engineering from Shahed University, Tehran, Iran, in 2010, and 2017, respectively. At the present, he is the assistant professor of electrical engineering department in Sirjan University of Technology. His especial fields of interest include transient in power systems, power quality and electrical machines.

Morteza Jadidoleslam received the B.Sc. degree from the Shahid Bahonar University of Kerman, Kerman, Iran, in 2008, the M.Sc. degree from the Isfahan University of Technology, Isfahan, Iran, in 2011, and the Ph.D. degree from the Isfahan University of Technology, Isfahan, Iran, in 2017, all in Electrical Engineering. He is currently an Assistant Professor in the Department of Electrical Engineering, Sirjan University of Technology, Sirjan, Iran. His research interests are power system planing, renewable energy, and micro grids.

International Journal Of
Industrial Electronics Control and Optimization
Print ISSN: 3517-2645
Online ISSN: 3568-2645
Homepage: https://ieco.usb.ac.ir/

A Multiport Isolated Resonant LLC Converter for Grid-Tied Renewable Energy Powered Bidirectional EV Charger

Nasim Bagheri[1]| Hasan Alipour[2]|Leila Mohammadian[3]|Jamal Beiza[4]| Mohsen Ebadpour[5]

Department of Electrical Engineering, Shabestar Branch, Islamic Azad University, Shabestar, Iran.[1,2,3,4,]
Department of Electrical Engineering, Ahar Branch, Islamic Azad University, Ahar, Iran[5].
Corresponding author's email: Hasan.alipour2006@gmail.com

Article Info

Article type:
Research Article

Article history:
Received: 2022-Sep-26
Received in revised form: 2023-Jan-03
Accepted: 2023-Feb-12
Published online: 2023-Feb-12

Keywords:
DC-DC converter,
Multiport,
Photovoltaic (PV) system,
Plug-in electric vehicles (PEVs),
Battery,

ABSTRACT

This paper proposes an integrated bidirectional multiport DC-DC converter for battery charging of plug-in electric vehicles, which can integrate the photovoltaic (PV) system, traction batteries, and the AC grid. The presented converter is more reliable than the conventional topologies because both PV panels and the grid can simultaneously or separately deliver power to high-voltage batteries. In addition, the topology is bidirectional and can transfer power from batteries to the AC grid by employing a half-bridge CLLC converter with fewer switches. Moreover, a unified controller along with optimum maximum power point tracking (MPPT) algorithm is utilized to control the converter. The converter topology, control system, and operating scenarios are analyzed by using state space modeling. The performance of the whole system is evaluated by testing the converter's operation in different conditions using MATLAB/Simulink software. The simulation results demonstrate that the proposed converter can not only control the charge and discharge of the batteries according to the state of the charge, but it can also maintain the DC-link voltage of the grid side to be in constant level.

I. Introduction

Nowadays, two widespread future trends in energy consumption are the rise in distributed renewable resources such as solar energy and the emergence of electric vehicles (EVs) as a green mode of transportation. Meanwhile, the integration of these two technologies faces more challenges in practice [1]. Firstly, EVs are zero-emission as long as the source of power is green. In addition, photovoltaic (PV) energy resources suffer from seasonal changes, so they entail a need for energy storage systems [2]. Furthermore, some voltage issues like overloading can occur in the power grid due to the overuse of distributed power resources and raised power demand of vehicle batteries [3-5]. To solve these problems, charging EVs with solar energy can be a decent solution that leads to net-zero emissions.

Integrating power sources has acquired universality in transportation electrifications. For this integration, the focus has been put on power electronic interfaces to enable the proper usage of energy systems. Plug-in electric vehicles (PEVs) vastly include three-phase battery chargers for their propulsion systems [6]. A typical traction battery charger topology contains an AC-DC power factor correction (PFC) converter, an isolated (transformer-equipped) or non-isolated DC-DC converter, and a power grid or a PV system as its input [7]. Several integrated DC-DC converter topologies have been presented for PEV battery chargers which can also interface renewable energy resources like solar system and the grid. A large number of the integrated converters are presented for single-phase system in which the power level is restricted by the range of the output voltage and current [8].

Different researchers have proposed non-isolated converters [9] that utilize a single switch [10]. In [11],

researchers use a hybrid of buck and boost converters to hybridize PV and battery systems. A soft-switched non-isolated three-port DC-DC topology is presented for a high-voltage gain converter using coupled inductors in [12]. Several previously established topologies are based on half-bridge converters for various applications such as transportation [13]. Other cases have established the hybridization of onboard multiport DC-DC converters for integrated energy systems. In [14], a pulse width modulation (PWM) strategy with a phase shift control method is used to integrate multiport converters. An onboard battery charger for EVs with the possibility of auxiliary feeding mode is presented in [15]. However, these topologies require complex electric circuits with more switching devices that cannot arrange isolations among the power network DC-link, traction batteries, and other energy sources as inputs of the converter [16]. The sliding mode control of LLC resonant DC-DC converter for a vast range of output voltage is presented for battery charging applications in [17]. The proposed controller operates at two switching frequencies for charging the EV batteries. The sliding mode control is a robust strategy for converter output voltage regulation with minimum distortion under a wide variation of input voltage, but it suffers from the chattering phenomenon, which deteriorates the overall system efficiency.

On the other hand, various topologies have been established using isolated DC-DC converters [18-20]. Some authors have focused on controlling the switching devices of the converter by employing different modulation methods such as pulse-frequency modulation [21] or phase-shift modulation with PWM [22]. There are other converter structures, such as half-bridge topologies [23] or coupled inductors controlled by phase-shift modulation [24]. Furthermore, bidirectional multiport resonant DC-DC converters are presented for vehicle-to-grid (V2G) operation and grid-to-vehicle (G2V) mode in PEV applications. However, some of them are unable to raise voltage gain and include circulating current between traction batteries and the power grid which deteriorates the grid current and induces unaccepted harmonic distortions [25]. In this regard, a new bidirectional multiport converter is presented in [26] which can be utilized as a converter that is installed in parking lots of intelligent places to provide power for local DC loads, such as DC home appliances and charge-connected EVs, simultaneously. The presented converter can act in G2H/G2VH/V2H/V2G scenarios. The topology is, however, very complicated and lowly reliable.

Other researchers have studied isolated CLLC topologies for battery chargers that contain discrete inductors, which escalate the size and cost of the converter circuit [27-29].

This paper presents an isolated multiport DC-DC converter for bidirectional EV battery chargers that can operate in PV-to-vehicle (PV2V), PV-to-grid (PV2G), G2V, and V2G modes. The modeling and analysis of the integrated converter for charging PEVs and also the hybridization of the PV system with traction batteries and the grid are the main considerations in this study. To reduce the volume and overall cost of the topology, the proposed resonant converter utilizes leakage inductance at the secondary and tertiary sides of the isolating transformer with no need for additional elements. Based on the presented model, several operation scenarios and modes are analyzed to better understand the converter's performance. PV panels can be mounted on the roof of parking areas as a stand-alone electric parking lot using the proposed converter to charge the vehicle with maximum solar power. The overall properties of the proposed topology and the contributions of this paper can be summarized as follows:

1) Isolation is provided among the PV array, the grid, and vehicle batteries.

2) A multi-output strategy is used for charging the traction batteries to rise the converter's reliability and efficiency.

3) There is no need for discrete inductors resulting in reduced size and cost of the converter circuit.

4) Using a comprehensive MIMO controller along with a proper maximum power point tracking (MPPT) control method to expand the voltage range.

5) A bidirectional battery charger that is capable of PV2G and V2G operation is designed and developed.

This manuscript is organized into six sections. Section II introduces the whole structure and operation modes of the converter. Operation principles and mathematical equations are expressed in detail in Section III. Section IV deals with the proposed control system. The complete simulation results considering the proposed control topology are given in Section V. Section VI summarizes the system performance, verifies the results, and provides some conclusions.

II. The Proposed Topology and Operation Scenarios

Conventional PEVs include a DC-AC inverter to feed the traction motor drive while the battery charger contains an AC-DC rectifier. The proposed converter improves them as an integrated bidirectional AC-DC and DC-DC converter, which can deliver power to the vehicle battery from a DC energy source, such as PV panels and the grid. The overall topology of the proposed converter is displayed in Fig. 1. As depicted in Fig. 1, a CLLC converter interfaces the battery port and the grid with a minimum number of switching devices, which can convey current using its symmetrical structure and the leakage inductance of three-winding integrated transformer [30]. Furthermore, the presented topology operates more stable than similar proposed multiport converters [30] since in the absence of the grid, PV arrays can charge the battery without any interruption (PV2V scenario). Hence, the AC grid can deliver power to the vehicle (G2V scenario) and also receive power from both PV panels (PV2V scenario) as an axillary power source and traction battery (V2G scenario) as an energy storage. Based on the proposed converter topology, the

isolated converter splits the DC-link capacitors into two center points connected to the transformer for reducing the stress of current and decreasing the differential mode conduction losses.

One of the attractive characteristics of the multiport boost converter is its simplicity. In essence, the proposed topology operates as a conventional boost converter that can swap its inputs and outputs. In comparison with conventional isolated converters, such as phase-shifted and LLC converters, the presented converter includes most advantages of the LLC converter such as soft switching at small loads and no need for an inductor of the output filter. Furthermore, the presented isolated topology enables intertwining an LLC resonant structure with the CLLLC converter by employing the tertiary winding of the isolated transformer when the vehicle charger operates in V2G modes. According to Fig. 1, the primary winding of the transformer is connected to the PV port while the secondary winding is coupled to the battery port. The third winding is connected to the AC grid. To properly obtain the converter parameters, it is necessary to correctly choose the turns ratio of the integrated transformer [30]. The core size of the transformer in practical applications is determined according to the switching frequency, voltage, and current level. This integrated converter rises the usage of the transformer, capacitors, and switching devices. Employing an electromagnetic integrated transformer with high inductance can (1) eliminate the external inductors, (2) decrease the converter volume, and (iii) reduce magnetic component losses. Modifications of the magnetic-core shapes and winding topologies have been studied in recent years, but this study is the first movement toward the integration of two leakage inductances in a three-winding transformer.

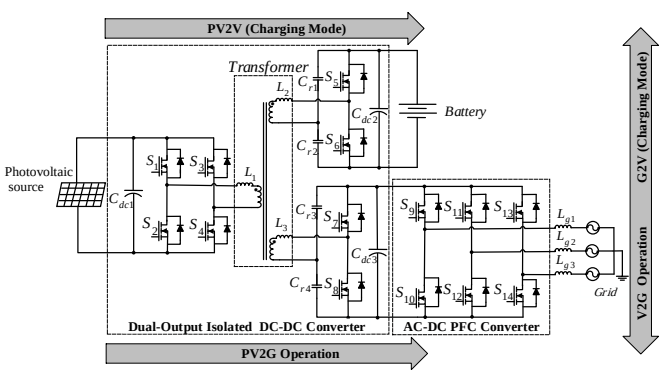

Fig. 1. The topology of the proposed multiport DC-DC converter

As Fig. 1 shows, the isolated structure includes two half-bridge converters at the secondary and tertiary sides of the transformer to lower the number of switching devices. Instead, the PV port at the primary side is equipped with a full-bridge converter to reduce the circulating current. Based on the proposed topology, the AC grid can deliver current to the batteries and also connect to PV arrays to acquire power. Moreover, the bidirectional PFC converter with switches ($S_9 \sim S_{14}$) is employed to improve the system's overall power quality and interface the AC grid.

Fig. 2. shows several operation scenarios of the converter. To reduce the voltage and current stresses of capacitors to around half, the resonant capacitors ($C_{r1} \sim C_{r4}$) deliver half resonant current in all scenarios. According to Fig. 2, for the bidirectional operation of the converter, the inductances (L_2 and L_3) of the isolating transformer act as the resonant inductors. Hence, C_{r1}, C_{r2}, and L_2 elements consist of a resonant circuit in scenarios I and IV whereas C_{r3}, C_{r4}, and L_3 elements lead to a resonant converter in scenarios II and III. Simultaneously conducting switches of the three ports is to be avoided in the proposed converter.

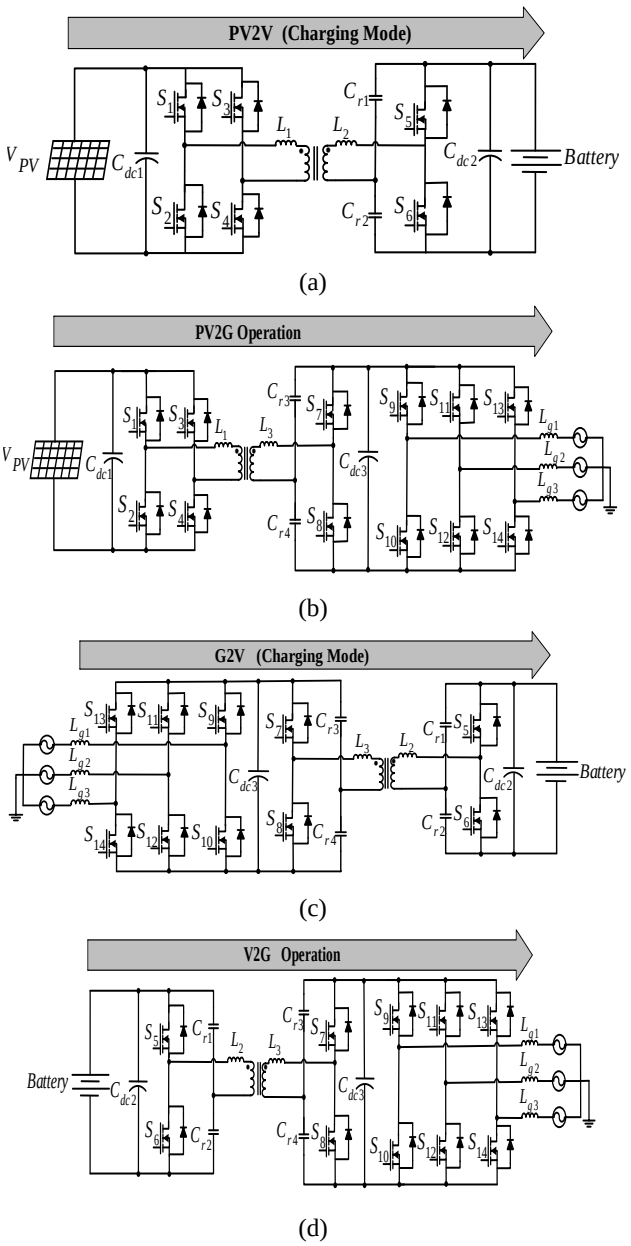

Fig. 2. The operation states for the isolated multiport converter: (a) Scenario I (PV2V), (b) Scenario II (PV2G), (c) Scenario III (G2V), (d) Scenario IV (V2G).

III. Operation Modes and Variables

To model and analyze the proposed converter's performance, the main variables and operation modes are

studied in detail. Since the voltage and current of the PV side are regulated by an MPPT controller, the system state variables can be expressed as

$$X^T = [i_{L1} \quad V_{Cdc3} \quad i_{L3} \quad i_{L2}]^T = [x_1 \quad x_2 \quad x_3 \quad x_4]^T \tag{1}$$

where $i_{L1\sim3}$ are the currents of the transformer inductances and v_{Cdc3} is the DC-link capacitor voltage of the AC grid.

To extract the averaged state-space model of the system, the state vectors during each scenario should be chosen. The detailed model of each scenario is described below.

A. Scenario I: PV to Vehicle (PV2V)

In Fig. 3, the current paths of the PV2V scenario are illustrated for different operation modes of the converter. As can be seen in Fig. 3(a), in scenario I in mode 1, switches S_1, S_4, and S_5 are delivering current to the battery from PV voltage (V_{PV}) through inductors L_1 and L_2 and capacitors C_1 and C_2. One of the system state variables (i_{L1}) which derivates from the PV current (I_{PV}) during mode 1 can be calculated with (2) by applying Kirchhoff's voltage low (KVL) through the red-arrowed current path (Fig. 3(a)) on the battery side.

$$v_{T2} = V_B - v_{L2} - v_{C2} \tag{2}$$

Applying Kirchhoff's voltage low for the red-arrowed current path on the PV side based on Fig. 3(a) can result in Eq. (3).

$$-V_{PV} + L_1 \dot{i_{L1}} + \frac{n_1 v_{T2}}{n_2} = 0 \tag{3}$$

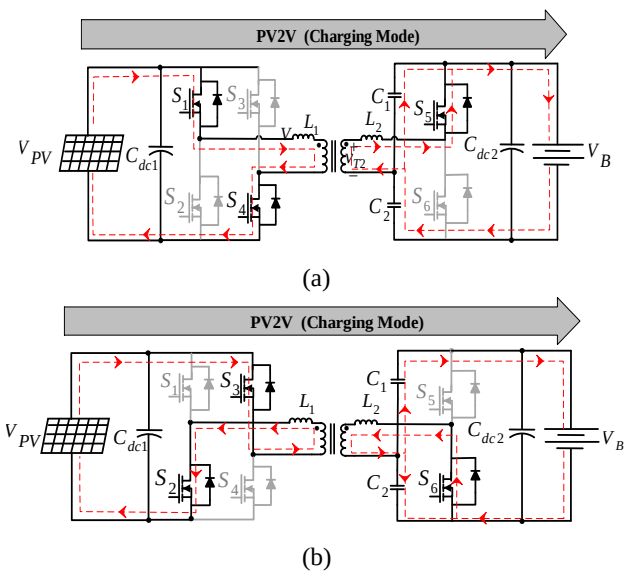

Fig. 3. The operation principles over PV2V scenario I: (a) Mode 1, (b) Mode 2

By combining Eq. (2) and (3), the averaged state-space equation in this mode can be found as follows

$$\dot{i_{L1}} = \frac{1}{L_1} V_{PV} - \frac{n_1}{n_2 \; L_1}(V_B - v_{L2} - v_{C1}) \tag{4}$$

where v_{T2} denotes the inducted voltage referred to the battery sides of the transformer, n_1/n_2 is its turn ratio, V_B is the battery voltage, v_L denotes the voltage across the leakage inductances of the transformer, and v_{C1} is the voltage of capacitor C_1.

Since the proposed converter plays the role of a charger in this scenario, the battery voltage is equal to

$$V_B = \frac{n_2}{n_1}(V_{PV} - v_{L1}) + v_{L2} + v_{C2} \tag{5}$$

According to Fig. 3(b), switches S_2, S_3, and S_6 deliver power to the battery by V_{PV} using inductors L_1 and L_2 and capacitors C_1 and C_2 during the second mode in scenario I. i_{L1} during mode 2 can be determined as

$$V_B + v_{L2} + v_{T2} - v_{C1} = 0 \tag{6}$$

$$-V_{PV} - L_1 \dot{i_{L1}} - \frac{n_1 v_{T2}}{n_2} = 0 \tag{7}$$

$$\dot{i_{L1}} = -\frac{1}{L_1} V_{PV} - \frac{n_1}{n_2 \; L_1}(v_{C1} - V_B - v_{L2}) \tag{8}$$

The battery voltage can be calculated as

$$V_B = \frac{n_2}{n_1}(V_{PV} + v_{L1}) - v_{L2} + v_{C1} \tag{9}$$

B. Scenario II: PV to Grid (PV2G)

Regarding to Fig. 4, during mode 3 of scenario II (Fig. 4(a)), switches S_1, S_4, and S_7 of the converter and S_9, S_{12}, and S_{14} of the PFC inverter deliver current from the PV port to the AC grid via inductors L_1 and L_3 and capacitor C_4. V_{Cdc3} (grid side DC-link voltage) as the second state variable of the converter in mode 3 can be written as

$$v_{T3} = -v_{L3} + v_{Cdc3} - v_{C4} \tag{10}$$

$$-V_{PV} + \frac{n_1 v_{T3}}{n_3} + L_1 \dot{i_{L1}} = 0 \tag{11}$$

$$v_{Cdc3} = v_{L3} + v_{C4} + \frac{n_3}{n_1}(V_{PV} - L_1 \dot{i_{L1}}) \tag{12}$$

As shown in Fig. 4(b), switches S_2, S_3, and S_7 of the converter and S_9, S_{12}, and S_{13} on the inverter port convey PV current to the AC grid using inductors L_1 and L_3 and capacitor C_3 in mode 4. The variable V_{Cdc3} during mode 4 can be expressed as

$$v_{T3} = -v_{L3} - v_{Cdc3} + v_{C3} \tag{13}$$

$$-V_{PV} - \frac{n_1 v_{T3}}{n_3} - L_1 \dot{i_{L1}} = 0 \tag{14}$$

$$v_{Cdc3} = -v_{L3} + v_{C4} + \frac{n_3}{n_1}(V_{PV} + L_1 \dot{i_{L1}}) \tag{15}$$

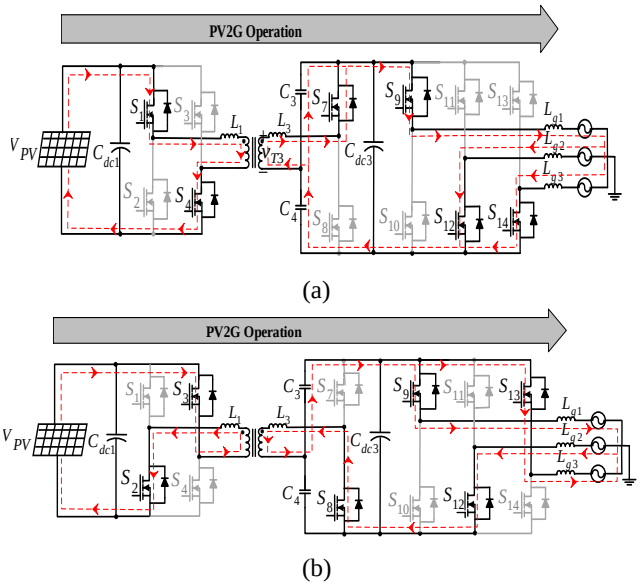

(a)

(b)

Fig. 4. The operation principles of PV2G modes: (a) Mode 3, (b) Mode 4

C. Scenario III: Grid to Vehicle (G2V)

Based on Fig. 5(a), switches S_5 and S_7 and also inverter switches S_{10}, S_{11}, and S_{14} conduct current to charge the vehicle from the AC grid by inductors L_2 and L_3 and capacitors C_1 and C_4 in mode 5. Another state variable of the converter (i_{L3}) which derivate from the AC grid current (I_G) in mode 5 can be determined as

$$v_{C4} + v_{T3} + L_3 \dot{i_{L3}} - v_{Cdc3} = 0 \tag{16}$$

$$v_{T2} = V_B - v_{C2} - v_{L2} \tag{17}$$

$$\dot{i_{L3}} = \frac{1}{L_3}(v_{Cdc3} - v_{C4}) - \frac{n_3}{n_2\ L_3}(\mathrm{V}_B - v_{C2} - v_{L2}) \tag{18}$$

In this scenario, the traction battery is also charged from the grid and the battery voltage can be found as

$$\mathrm{V}_B = \frac{n_2}{n_3}(v_{Cdc3} - v_{C4} - v_{L3}) + v_{C2} + v_{L2} \tag{19}$$

Similarly, over mode 6 (see Fig. 5(b)), differential equations can be expressed as

$$v_{T2} = -V_B + v_{C1} - v_{L2} \tag{20}$$

$$\dot{i_{L3}} = \frac{1}{L_3}(v_{Cdc3} - v_{C4}) - \frac{n_3}{n_2\ L_3}(\mathrm{V}_B - v_{C1} + v_{L2}) \tag{21}$$

$$\mathrm{V}_B = \frac{n_2}{n_3}(v_{Cdc3} - v_{C4} - v_{L3}) + v_{C1} - v_{L2} \tag{22}$$

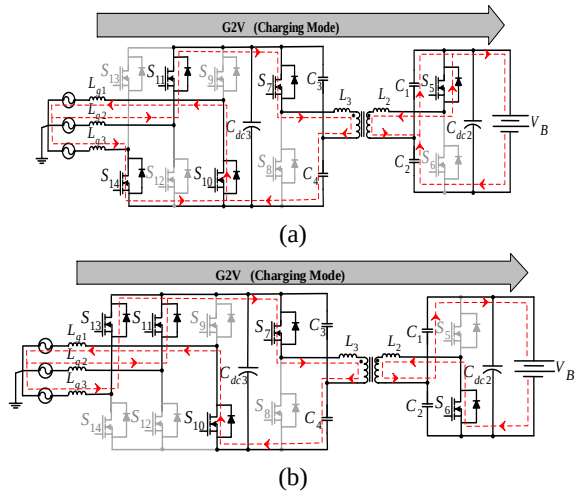

(a)

(b)

Fig. 5. Operation principles during G2V modes: (a) Mode 5, (b) Mode 6

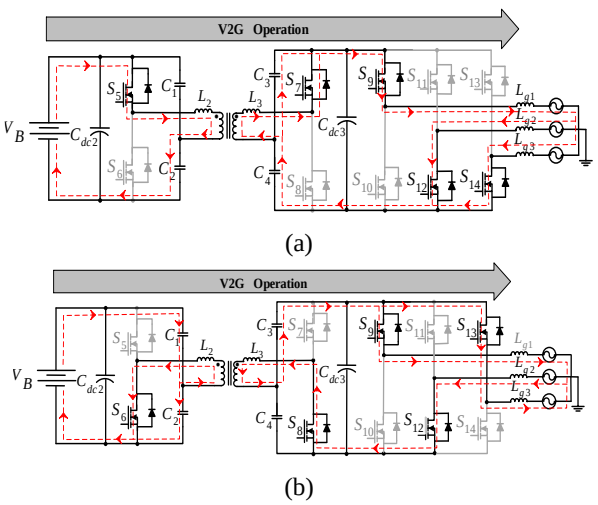

(a)

(b)

Fig. 6. The converter's performance over V2G scenario: (a) Mode 7, (b) Mode 8

D. Scenario IV: Vehicle to Grid (V2G)

According to Fig. 6(a), converter switches S_5 and S_7 and inverter-side switches S_9, S_{12}, and S_{14} are switched ON to deliver current from the vehicle to the grid by inductors L_2 and L_3 and capacitors C_2 and C_4. Then, the other variable of the converter (i_{L2}) which derivates from the battery current (I_B) during mode 6 is obtained as

$$\dot{i_{L2}} = \frac{1}{L_2}(\mathrm{V}_B - v_{C2}) - \frac{n_2}{n_3\ L_2}((v_{Cdc3} + v_{L3} + v_{C3}) \tag{23}$$

Similarly, based on Fig. 6(b), in mode 8, i_{L2} can be calculated as

$$\dot{i_{L2}} = \frac{1}{L_2}(v_{C2} - \mathrm{V}_B) + \frac{n_2}{n_3\ L_2}((v_{Cdc3} + v_{L3} - v_{C3}) \tag{24}$$

Owning to the explained operation modes, the isolated multiport converter can transfer power from and to different ports. To conclude the operation modes, Table 1 lists the switching patterns of the converter for each operation mode.

TABLE 1
THE OPERATION MODES AND PATTERNS OF CONVERTER SWITCHING FOR DIFFERENT SCENARIOS

Scenario	Mode	DC-DC Converter switches states								Charging mode
		S_1	S_2	S_3	S_4	S_5	S_6	S_7	S_8	
I	1	1	0	0	1	1	0	0	0	Yes
	2	0	1	1	0	0	1	0	0	
II	3	1	0	0	1	0	0	1	0	No
	4	0	1	1	0	0	0	0	1	
III	5	0	0	0	0	1	0	1	0	Yes
	6	0	0	0	0	0	1	1	0	
IV	7	0	0	0	0	1	0	1	0	No
	8	0	0	0	0	0	1	0	1	

IV. The Control of the Proposed Converter

The applied control strategy ensures that the current delivered to/from the grid is near sinusoidal with accepted quality and in phase. The overall block diagram of the studied converter's control strategy is shown in Fig. 7 in which to regulate the battery voltage, the voltages of the DC links must be fixed and the gain of the converter is appropriately adjusted. There is a unified multifunctional controller for PFC and DC-DC converters which is described in detail in this section. Since the converter operation depends on the aforementioned state variables, according to Fig. 7, the first state variable i_{L1} is controlled by the MPPT block through I_{PV}, v_{Cdc3} is regulated by the voltage PI controller, i_{L3} is controlled by the PFC inverter controller, and the last state variable i_{L2} is controlled by the battery-side current PI controller through I_B. Voltage and current controllers are employed to provide effective performance in adjusting DC values and then zero steady-state errors.

A. MPPT Controller for PV port

Since the PV cell suffers from environmental conditions such as irradiance level and surrounding temperature, to improve the efficiency of the PV system, the MPPT controller is necessary. For MPPT, the duty cycle of PV-side converter switches can be found by an appropriate definition of the error signal that comes from a closed-loop controller. Common MPPT approaches like constant voltage tracking (CVT) [31], incremental conductance (INC) scheme [32], and the Perturb and Observe (P&O) method [30] are presented. The CVT method has low accuracy and reliability due to voltage stabilizing rather than MPPT. Both the INC and the P&O methods can fluctuate near the maximum power point, normally an adaptive step to acquire better performance.

The proposed converter employs the INC algorithm-based MPPT control which is implemented using an integral controller to maximize the PV panel's output power. The basic concept of the INC approach is that the slope of the Power-Voltage (P-V) characteristics of the PV module which is illustrated in Fig. 8 is zero at maximum power points. It can be obtained from Fig. 8 that the condition for achieving maximum power at the peak point of the curve can be derived from the PV system output power as follows

$$\frac{dP_{PV}}{dV_{PV}} = \frac{d(V_{PV} I_{PV})}{dV_{PV}} = I_{PV} + V_{PV} \frac{dI_{PV}}{dV_{PV}} = 0 \tag{25}$$

The maximum power point is obtained by satisfying

$$\frac{dI_{PV}}{dV_{PV}} = -\frac{I_{PV}}{V_{PV}} \tag{26}$$

In numerical studies, the differential of PV voltage and current (V_{PV} and I_{PV}) can be calculated as

$$\begin{cases} dI_{PV} = I_{PV}(k) - I_{PV}(k-1) \\ dV_{PV} = V_{PV}(k) - V_{PV}(k-1) \end{cases} \tag{27}$$

where *k* is the time interval. The essence of defining the maximum power points by the INC method is to determine the optimum working point that satisfies Eq. (26).
There are three criteria in the process of the INC algorithm as follows

$$\begin{cases} 1) \text{ if } dI_{PV} / dV_{PV} > -I_{PV} / V_{PV} \text{ then increase } V_{PV} \\ 2) \text{ if } dI_{PV} / dV_{PV} < -I_{PV} / V_{PV} \text{ then decrease } V_{PV} \\ 3) \text{ if } dI_{PV} / dV_{PV} = -I_{PV} / V_{PV} \text{ then unchange } V_{PV} \end{cases} \tag{28}$$

To achieve the criteria in Eq. (28), a PI controller is employed to minimize the MPPT error. According to Fig. 9, the MPPT block takes the PV cell voltage and current as its inputs and regulates them to properly switch the PV-side converter gates. Then, when the solar irradiance varies, the MPPT controller adjusts the output based on the new maximum power point.

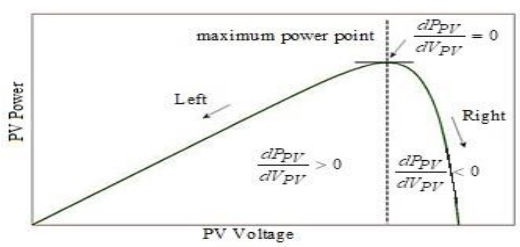

Fig. 8. The P-U characteristics of the PV module based on the INC concept

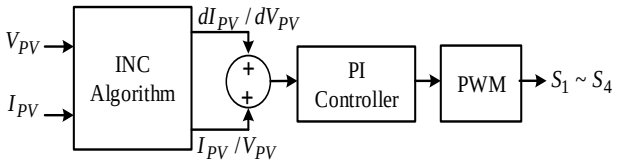

Fig. 9. The block diagram of the MPPT controller

B. PFC Inverter Controller

The control diagram of the PFC boost rectifier is depicted in Fig. 10. The PFC controller can secure the sinusoidal input from the AC grid current which results in a unity power factor and regulates the output voltage ($v_{C_{dc3}}$) at a constant desired level ($V_{dc,ref}$). The control scheme contains an inner current loop for the grid synchronization, an outer voltage loop for controlling $v_{C_{dc3}}$, and a three-phase phase-locked loop (PLL) to extract the grid voltage phase angle ($\phi = \omega t$). The extracted phase angle is applied to dq0 to abc Park's transformation and for synchronizing injected currents with grid voltages using the error signal of the AC-side DC-link controller (I_{d_ref}) . The control method is implemented using the dq0 synchronous reference frame which converts the grid quantities to DC values (v_{dq_mes} and i_{dq_mes}) to make the control easier.

The required active power is set by the direct axis reference current I_{d_ref} while the needed reactive power is determined using the quadrature axis reference current I_{q_ref} which is set to zero to make the unity power factor. The output voltages of the current regulator block are converted back to the abc values to serve as the reference signals utilized by the PWM pulse generator.

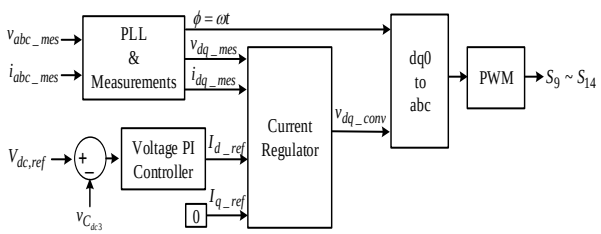

Fig. 10. The PFC controller's block diagram

C. Scenario Selection Scheme

The most important part of the control strategy is the scenario selection part, which allows the battery to be charged first from the solar cells and also allows it to be charged or discharged from/to the grid, as shown in Fig. 11. According to Table I, the control method mainly chooses scenario I (stand-alone operation) and scenario III (grid-connected operation) or both (PV2V + G2V), which makes the battery to be charged. Since the vehicle is never driven during plugged-in, the two charging scenarios can be separated by the scenario selection algorithm. This makes the converter operate in several modes with different scenarios. Furthermore, in contrast to the last established multiport converters which widely depend on the grid [30], the proposed control method enables the converter to perform as an off-grid and/or a grid-connected charger which can elevate charger reliability.

To extend the performance of the charger ports over the entire range of voltage, two variable DC-links ($v_{C_{dc2}}$ and $v_{C_{dc3}}$) are capable of delivering power to the vehicle. Considering Fig. 7, to minimize the errors in the control strategy between the reference values and measured amounts, standard PI controllers are employed.

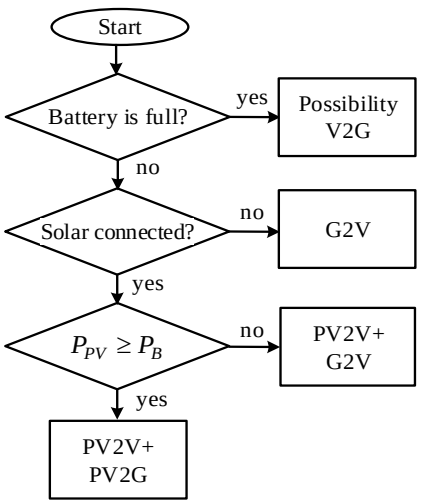

Fig. 11. The PFC scenario selection flowchart diagram

V. Simulation Results and Discussions

To test the proposed converter's operation and control methodology, the whole topology is built and simulated in MATLAB/Simulink environment. The major parameters of the converter elements are shown in Table 2. SunPower SPR-415E-WHT-D PV arrays are used for PV systems whose module parameters under specification standard test conditions (temperature = 25ºC, irradiation = 1000 W/m^2) are shown in Table 3. The voltage of the vehicle battery can be varied from 240 to 420 V, and the DC-link voltage of the grid side is controlled from 300 V to 600 V. The switching frequency of devices changes from 180 kHz to 200 kHz. The gain of the PI controllers is obtained through a trial-and-error procedure.

TABLE 2
MAIN PARAMETERS OF THE CONVERTER USED IN THE SIMULATION

Component	value
L_1	64 uH
L_2	38 uH
L_3	85 uH
N1:N2:N3	40:20:30
C_{r1} , C_{r2}	10 uF
C_{r3} , C_{r4}	5 uF

TABLE 3
PV MODULE PARAMETERS

parameter	**value**
Open-circuit voltage	64.2 V
Short-circuit current	5.96 A
Maximum power point voltage	54.7 V
Maximum power point current	5.58 A
Maximum power	305.27 W
Number of series-connected modules per string	5
Number of parallel strings	66
Number of cells per module	96

To test the steady state and dynamic performance of the PV arrays under different conditions of disturbance in solar irradiation at standard temperature, two types of irradiation changes, first ramp changes and then severe step disturbances are studied. In the first study, the solar radiation is slowly changed and the PV cells are subjected to ramp variations as shown in Fig. 12 to evaluate the profile of output power and voltage which come from PV arrays. According to Fig. 12, initial solar radiation is set to 1000 W/m^2 and can generate power of about 24 kW. Based on Fig. 12(b), the DC-link voltage of the PV side quickly reaches its reference value of 480 V due to proper tuning of the MPPT controller. To assess the dynamic response of the system, at time 0.4 s, the irradiance changed slowly and dropped to 200 W/m^2 which makes power track this change and settle down around 0.15 s. Regarding the scenario selection algorithm, during time 0.8 s to 1 s, the PV power is decreased and the converter operates in scenario III to charge the vehicle battery from the AC grid through the PFC inverter. To operate in scenario, I, the solar irradiance rose to 600 W/m^2 at t=1 s, leading to an increase in power to around 14.5 kW. Considering Fig. 12, it can be seen that after all disturbances in solar irradiation, both PV power and voltage settle down in their reference values by employing the ideal maximum power tracking algorithm.

To examine the performance of the PV system under extreme changes in solar irradiation, the array is subjected to sudden step variations as depicted in Fig. 13. Similar to the first test, at t = 0.4 s, the irradiation suddenly dropped to 400 W/m^2 then increased to 800 W/m^2. The DC link voltage reaches the desired steady state values during all these severe variations as illustrated in Fig. 13 (b). Based on Fig. 13(c), the PV output power followed the changes and settled with about a 60-ms delay. Since temperature changes in modules can also affect the PV outputs, the system reactions to the temperature step variations are also tested here. Fig. 14 shows the PV port responses to the temperature changes at constant standard irradiation of 1000 W/m^2. According to Fig. 14(a), the initial PV array temperature is 25^{o}C which leads to the generation of 24 kW power based on Fig. 14(c). At t = 0.4 s, the temperature increased to 40^{o}C and the PV power tracked this change by a little reduction in voltage and power. At t=1 s, the temperature dropped to 15^{o}C, boosting the voltage and power. Hence an increase in temperature can slightly reduce the PV output voltage and power.

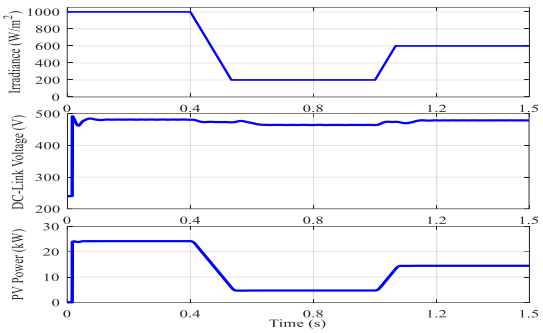

Fig. 12. The PV system's responses to ramp variations. (a) Solar radiation, (b) PV voltage, and (c) output power

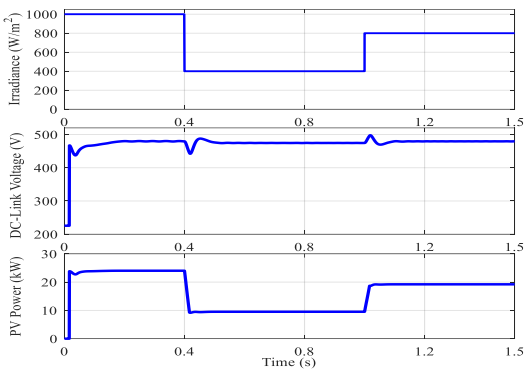

Fig. 13. The PV system's outputs for sudden step disturbances. (a) Solar radiation, (b) PV voltage, (c) output power

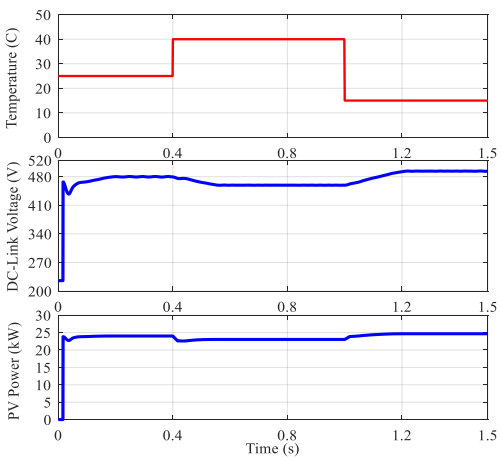

Fig. 14. The PV system's responses to step changes in temperature. (a) Temperature profile, (b) PV voltage, (c) output power

A. Converter Performance in Scenario I: PV2V Operation

To validate the stable performance of the MPPT algorithm and converter controllers ,the irradiation of 1000 W/m^2 at a fixed temperature of 25^{o}C is considered. As was already described, during the PV2V battery charging scenario, switches S_1 to S_4 on the PV side and switches S_5 and S_6 on the battery side serve as a DC chopper. Fig. 15 illustrates the results of the battery charging

during PV2V at maximum PV power of about 25 kW. Some small fluctuations are seen in voltage during the first intervals, but the converter insures 480 and 400 volts across the PV port and battery side, respectively. As illustrated in Fig. 16, the output power from PV panels (P_{PV}) is around 24 kW which is much higher than battery power (P_B), i.e., 4 kW. Therefore, in this scenario, the vehicle battery can completely charge from solar energy with no need for the power grid.

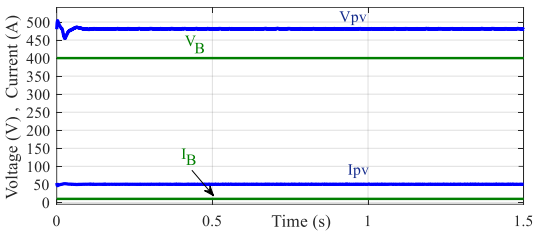

Fig. 15. The voltage and current outputs for the PV2V scenario during steady-state operation

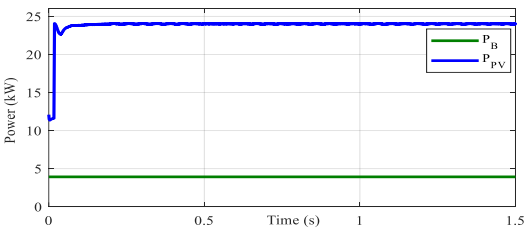

Fig. 16. The output power of the PV panels and vehicle battery for the PV2V scenario

B. Converter Performance in Scenario II: PV2G Operation

As was already explained, one of the imperative features of the proposed converter is the delivery of power to the grid when the PV output power is sufficiently high. According to Fig. 17, the current flows from the PV port to the grid and the converter acts as a grid-connected topology. Based on this scenario, the redundant power of the PV can inject into the network and feed some small loads to improve the whole system's performance.

C. Converter Performance in Scenario III: G2V Operation

Based on the aforementioned information, the battery can charge from the grid, too. Fig. 18 shows the charging operation when the battery is charged via the grid. This scenario improves the charger's reliability when the PV side suffers from environmental or seasonal conditions.

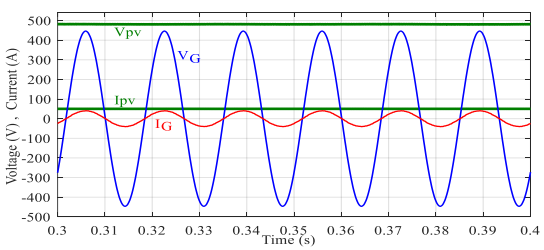

Fig. 17. The voltage and current outputs of the converter for the PV2G scenario during the steady-state operation

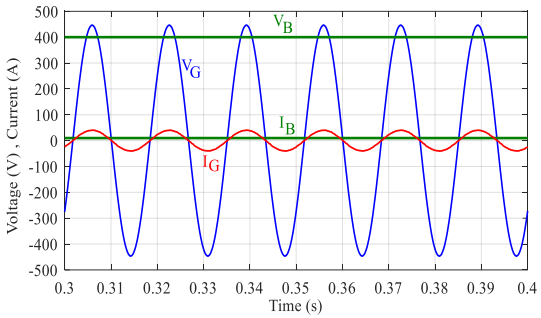

Fig. 18. The responses to the G2V scenario at the steady-state operation

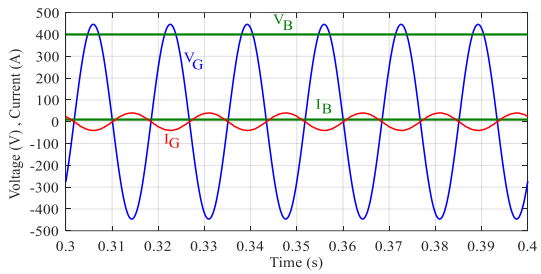

Fig. 19. The responses to the V2G scenario at steady-state

D. Converter Performance in Scenario IV: V2G Operation

Considering the proposed topology, vehicles can deliver their extra and/or unused power to the grid when needed. Hence, according to Fig. 19, battery current flows into the grid and ensures the bidirectional operation of the converter. As shown in Figs. 18 and 19, the current delivered to and from the AC grid is to be sinusoidal and in phase with the grid AC voltage which reduces current distortions and keeps a unity power factor. As illustrated in Fig. 19, the injected AC current is in the reverse direction of the grid voltage, but zero crossings points of the voltage and current still match each other.

E. Efficiency Comparison

To compare the results decently, it is better to consider the overall efficiency improvements over a wide range of parameter or variable variations. For this matter, the converter efficiency is compared for output power variations by taking the grid side voltage into account in this subsection. Fig. 20 illustrates the proposed isolated LLC converter efficiency during the scenarios in which EV batteries get charged under different voltage levels. As mentioned before, one of the key factors in battery charging is the state of charge (SOC) level which should be maintained at a rescannable rate (between 20 to 80 percent). The converter efficiency along with the output power is analyzed over the variable battery voltage from 250V to 400 V (from SOC around 60 to 100 percent, respectively) in Fig. 20. By choosing a constant input DC voltage, the efficiency declines as the output power P_O and also output current rises. On the other hand, the efficiency increases at a fixed DC-link

current. Furthermore, the maximum efficiency is around 96.3% at a power of 1 kW. Accordingly, for an appropriate SOC (around 75%), the efficiency of 96% at an output power of around 750 W for a battery voltage level of 300V is more acceptable.

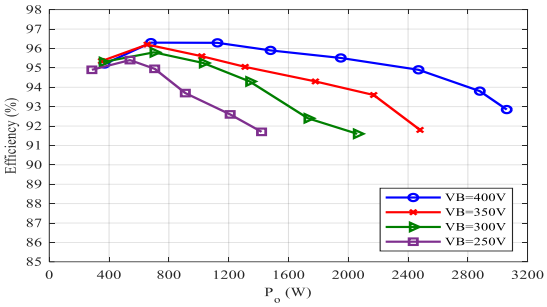

Fig. 20. The efficiency of the proposed converter during the battery charging modes

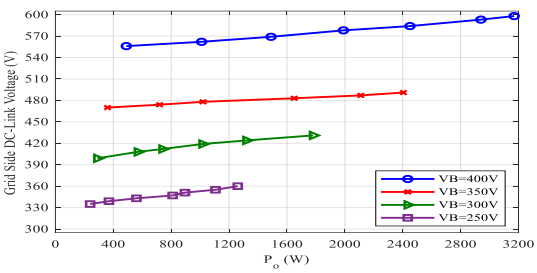

Fig. 21. The grid-side DC-link voltages during different studies using variable control of DC-link voltage.

A similar comparison study is performed in Fig. 21 which shows the grid-side DC-link voltage of the converter under different testing circumstances. Since one of the charging ports of the converter is the AC grid, the variations of DC voltage in the grid side should be analyzed to maintain not only the battery charging level but also the grid power factor. At the fixed battery voltage (V_B= 400V) and around the power related to the maximum efficiency (P_o=1 kW), the DC-link voltage is equal to 565V. For better SOC, the grid-side voltage should be maintained at 420V.

I. Conclusions

A multiport isolated DC-DC converter is studied for PEV applications by integrating the PV arrays and the power grid. The proposed converter was utilized to interface a hybrid energy system with separate sources based on different operation scenarios. As explained, the converter is designed as high power with low cost over a wide range of output voltage. A feasible unified multifunctional control system is employed to control the whole system. Considering the results, the converter operates appropriately during all different scenarios. Based on the control methodology, standard PI controllers are used to regulate the PV-side DC-link voltage, the grid-side voltage, and the battery voltage and current. The simulation results reveal that the converter is not only capable of MPPT for the PV system when solar energy is available, but can also control the charge/discharge of the vehicle battery to keep the DC-link voltage at a desired value. One of the distinguished features of the converter is the delivery of power to the battery from two ports in the lack of the PV power.

Acknowledgment

The corresponding author wishes to thank Dr. Mohsen Ebadpour for presenting and establishing the initial idea of this study named “A multiport isolated DC-DC converter for plug-in electric vehicles based on combination of photovoltaic systems and power grid” in “*12th Power Electronics, Drive Systems, and Technologies Conference (PEDSTC)*” of IEEE which was held in Tehran, Iran 2021 (see Ref. [29]). He is currently one of the manuscript authors and also the advisor in this research work.

REFERENCES

[1] Feizi M, Beiranvand R, Daneshfar M. An Integrated High Power Self-Equalized Battery Charger Using a Voltage Multiplier and Phase-Shifted Full-Bridge DC-DC Converter for Lithium-Ion Batteries. International Journal of Industrial Electronics Control and Optimization 2021; 4(2):141-155.

[2] Gonzalez A, Lopez-Erauskin R, Gyselinck J. Analysis, modeling, control and operation of an interleaved three-port boost converter for DMPPT systems including PV and storage at module level. Heliyon 2019; 5(3):1-31.

[3] Pan L, Zhang C. An Integrated Multifunctional Bidirectional AC/DC and DC/DC Converter for Electric Vehicles Applications. Energies 2016; 9(7):493.

[4] Ebadpour M, Sharifian M.B.B. Cascade H-Bridge Multilevel Inverter with Low Output Harmonics for Electric/Hybrid Electric Vehicle Applications. International Review of Electrical Engineering (IREE) 2012; 7(1): 3248-3256.

[5] Tu h, Feng H, Srdic S, Lukic S. Extreme Fast Charging of Electric Vehicles: A Technology Overview. In: IEEE Transactions on Transportation Electrification; 2019. IEEE; 2019. p. 861-878.

[6] Jyotheeswara Reddy K, Natarajan S. Energy sources and multi-input DC-DC converters used in hybrid electric vehicle applications – A review. International Journal of Hydrogen Energy 2018; 43(36):17387-17408.

[7] Yilmaz M, Krein PT. Review of battery charger topologies, charging power levels, and infrastructure for plug-in electric and hybrid vehicles. IEEE Trans Power Electron 2013; 28(5):2151-2169.

[8] Pellegrino G, Armando E, Guglielmi P. An Integral battery charger with power factor correction for electric scooter. IEEE Trans Power Electron 2010; 25(3):751-759.

[9] Zhu H, Zhang D, Zhang B, Zhou Z."A nonisolated three-port DC–DC converter and three-domain control method for PV-battery power systems. IEEE Trans Ind Electron 2015; 62(8):4937-4947.

[10] Wen G, Chen Y, Kang Y. A family of cost-efficient integrated single-switch three-port converters. In: Twenty-Eighth Annual IEEE Applied Power Electronics Conference and Exposition (APEC); 2013. IEEE; 2013. p. 1062-1067.
[11] Cheng T, Lu DDC, Gong A, Verstraete D. Analysis of a three-port DC-DC converter for PV-battery system using DISO boost and SISO buck converters. In: Australasian Universities Power Engineering Conference (AUPEC); 2015. IEEE; 2015. p. 1-6.
[12] Faraji R, Farzanehfard H. Soft-switched nonisolated high step-up three-port DC–DC converter for hybrid energy systems. IEEE Trans Power Electron 2018; 33(12):10101-10111.
[13] Kumar L, Jain S, A multiple source DC/DC converter topology. Int J Electron. Power Energy Syst 2013; 51:278-291.
[14] Li W, Xiao J, Zhao Y, He X. PWM plus phase angle shift (PPAS) control scheme for combined multiport dc/dc converters. IEEE Trans Power Electron 2012; 27(3):1479–1489.
[15] Pinto JG, Monteiro V, Goncalves H, Afonso JL. On-board reconfigurable battery charger for electric vehicles with traction-to-auxiliary mode. IEEE Trans Veh Technol 2014; 63(3):1104–1116.
[16] Wu H, Sun K, Ding S, Xing Y. Topology derivation of nonisolated three-port dc-dc converters from DIC and DOC. IEEE Trans Power Electron 2013; 28(7):3297–3307.
[17] Taheri A, Asgari N. Sliding Mode Control of LLC Resonant DC-DC Converter for Wide output voltage Range in Battery Charging Applications. International Journal of Industrial Electronics Control and Optimization 2019; 2(2):127-136.
[18] Chen Y-M, Liu Y-C, Wu F-Y. Multi-input DC/DC converter based on the multiwinding transformer for renewable energy applications. IEEE Trans Ind Appl 2002; 38(4):1096-1104.
[19] Wu H, Sun K, Chen R, Hu H, Xing Y. Full-bridge three-port converters with wide input voltage range for renewable power systems. IEEE Trans Power Electron 2012; 27(9):3965-3974.
[20] Hu W, Wu H, Xing Y, Sun K. A full-bridge three-port converter for renewable energy application. In: IEEE Applied Power Electronics Conference and Exposition – APEC; 2014. IEEE; 2014. p. 57-62.
[21] Sun X, Shen Y, Li W, Wu H. A PWM and PFM hybrid modulated three-port converter for a standalone PV/battery power system. IEEE Journal of Emerging and Selected Topics in Power Electronics 2015; 3(4): 984-1000.
[22] Zhang J, Wu H, Qin X, Xing Y. PWM plus secondary-side phase-shift controlled soft-switching full-bridge three-port converter for renewable power systems. IEEE Trans Ind Electron 2015;62(11):7061-7072.
[23] Tao H, Duarte JL, Hendrix MAM. Three-port triple-half-bridge bidirectional converter with zero-voltage switching. IEEE Trans Power Electron 2008; 23(2):782-792.
[24] Xu C et al. Performance analysis of coupled inductor based multiple-input DC/DC converter with PWM plus phase-shift (PPS) control strategy. In: IEEE ECCE Asia Downunder; 2013. IEEE; 2013. p. 994-998.
[25] Zeng J, Qiao W, Qu L.A n isolated three-port bidirectional dc-dc converter for photovoltaic systems with energy storage. IEEE Trans Ind Appl 2015; 51(4):3493–3503.
[26] Soltani Gohari H, Abbasadeh K, Gholami Gorji J. A Controllable Bidirectional Rectifier for EV Home Charging Station with G2H/G2VH/V2H/V2G Functions. International Journal of Industrial Electronics Control and Optimization 2021; 4(1):99-113.
[27] Zhao B, Song Q, Liu W, Sun Y. Overview of dual-active bridge isolated bidirectional dc-dc converter for high-frequency-link power-conversion system. IEEE Trans Power Electron 2014; 29(8):4091–4106.
[28] Jung J, Kim H, Ryu M, Baek J. Design methodology of bidirectional CLLC resonant converter for high-frequency isolation of dc distribution systems. IEEE Trans Ind Electron 2013; 28(4):1741–1755.
[29] Ebadpour M. A multiport isolated DC-DC converter for plug-in electric vehicles based on combination of photovoltaic systems and power grid. In: 12th Power Electronics, Drive Systems, and Technologies Conference (PEDSTC); 2021. IEEE; 2021. p. 1-5.
[30] Tang Y, Lu J, Wu B, Zou S, Ding W, Khaligh A. An integrated dual-output isolated converter for plug-in electric vehicles. IEEE Trans Veh Technol 2018; 67(2):966–976.
[31] Koutroulis E, Kalaitzakis K, Voulgaris NC. Development of a microcontroller-based, photovoltaic maximum power point tracking control system. IEEE Trans Power Electron 2001; 16(1):46-54.
[32] Li C, Chen Y, Zhou D, Liu J, Zeng J. A high-performance adaptive incremental conductance MPPT algorithm for photovoltaic systems. Energies 2016; 9(4):288.
[33] Mohanty S, Subudhi B, Ray PK. A grey wolf-assisted perturb & observe MPPT algorithm for a PV system. IEEE Trans Energy Convers 2017; 32(1):340-347.

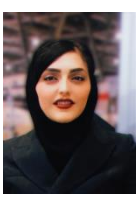

Nasim Bagheri was born in Tabriz, Iran in 1991. She received her B.Sc. degree in Biomedical Engineering from the Sahand University of Technology, Tabriz in 2013 and her M.Sc. degree in Electrical Engineering from Shabestar Azad University, Shabestar, Iran in 2015. She is a Ph.D. candidate in Electrical Engineering at Islamic Azad University, Shabestar Branch. Her current research interests include the hybrid and control of power electronic converters and their applications.

Hasan Alipour received B.Sc., M.Sc., and Ph.D. degrees in Power Electrical Engineering from the Iran University of Science and Technology (IUST), Tehran, Iran in 2008, the University of Tehran, Tehran, Iran in 2011, and the University of Tabriz, Tabriz, Iran in 2015, respectively. Currently, he is an assistant professor at the Engineering Faculty of Islamic Azad University, Shabestar Branch. His research interests include Electric and hybrid electric vehicles, electric machines drive, linear electric motors, renewable energies, and distributed generation.

Leila Mohammadian was born in Tabriz, Iran in 1984. She received her B.Sc., M.Sc., and Ph.D. degrees in Electrical Engineering from the Department of Electrical and Computer Engineering, University of Tabriz, Tabriz, Iran in 2007, 2011, and 2015, respectively. She has been with Shabestar Branch, Islamic Azad University, Shabestar, Iran since 2011. She has been an Assistant Professor since 2015. Her current research interests include the analysis and control of power electronic converters and their applications.

Jamal Beiza received his M.Sc. and Ph.D. degrees in Electrical Engineering from the Amirkabir University of Technology (AUT), Tehran, Iran in 2003 and 2009, respectively. He has been with the Department of Electrical Engineering of Islamic Azad University, Shabestar branch, Iran where he is now an Assistant Professor. His main fields of research are power system state estimation, power system operation, power system simulation, and modeling. He is a reviewer member of some scientific master Journals with the Institute for Scientific Information index. He has authored and co-authored more than 40 scientific papers.

Mohsen Ebadpour received his M.Sc. and Ph.D. degrees from the University of Tabriz, Iran, both in Electrical Power Engineering in 2011 and 2017, respectively. From March 2016 to March 2018, he had been a visiting research scholar at the Department of Electrical Engineering in the EPES research group at the University of British Columbia, Vancouver, Canada. Since 2011, he has joined the Department of Electrical Engineering, Islamic Azad University where he became an Assistant Professor in 2017. Currently, he is serving as an Associate Research Fellow in Research and Innovation Center for Electrical Engineering (RICE) with the University of West Bohemia in Pilsen, Czech Republic. He is the author and co-author of more than 30 journal and conference papers. His research interests include electrical machine drive control, modeling and analysis of power electronic converters, and fault-tolerant control.

International Journal Of
Industrial Electronics Control and Optimization
Print ISSN: 3517-2645
Online ISSN: 3568-2645
Homepage: https://ieco.usb.ac.ir/

PSO-Based EKF Wheel-Rail Adhesion Estimation

Ramazan Havangi [1]| Maryam Moradi [2]

Faculty of Electrical Engineering and Computer, University of Birjand, Birjand, Iran.[1,2]
Corresponding author's email: Havangi@Birjand.ac.ir

Article Info

Article type:
Research Article

Article history:
Received: 2022-Sep-04
Received in revised form:2023-Jan-09
Accepted: 2023-Feb-02
Published online: 2023-March-15

Keywords:
Adhesion force,
Wheel-rail,
Contact condition estimation,
PSO-based EKF.

ABSTRACT

An ideal traction and braking system not only ensures ride comfort and transportation safety but also attracts significant cost benefits through the reduction of damaging processes in wheel-rail and optimum on-time operation. To overcome the problem of the wheel slip/slide at the wheel-rail contact surface, it is crucial and scientifically challenging to detect adhesion and its changes because adhesion is influenced by different factors. However, critical information this detection provides is applicable not only in the control of trains to avoid undesirable wear of the wheels/track but also in the safety compromise of rail operations. The adhesion level between the wheel and rail cannot be measured directly, but the friction on the rail surface can be measured using measurement techniques. The braking and traction control system can be characterized by estimating wheel-rail adhesion conditions during railway operations. This paper presents the Particle Swarm Optimization (PSO)-based Extended Kalman Filter (EKF) to estimate adhesion force. The main limitation in applying EKF to estimate states and parameters is that its optimality is critically dependent on the proper choice of the state and measurement noise covariance matrices. To tackle this difficulty, a new approach based on the use of the tuned EKF is proposed to estimate induction motor (as a main part of the train moving system) parameters. This approach consists of two steps. In the first step, the covariance matrices are optimized by PSO and then, their values are introduced into the estimation loop. Finally, the superiority of the PSO-based EKF algorithm is verified by making simulations in Matlab and comparing the estimation performances of this technique and EKF. The results prove an acceptable performance in load torque and speed estimation after tuning the covariance matrices and confirm the high accuracy and efficiency of the proposed method.

NOMENCLATURE

a and b: semi-axis length of the contact patch
B and D: reduction factors
C_{11}: Kalker coefficient
C_v: viscous friction
F_a: adhesion force
F_N: normal force between the wheel and rail
G: shear module
$I_{s\alpha}$ and $I_{s\beta}$: $\alpha-\beta$ axis stator currents
c_1 and c_2:self-recognition and social component coefficients
J_{eqv}, J_x: equivalent and wheelset axle moment of inertia
J_g: gearbox moment of inertia
$\psi_{r\alpha}$ and $\psi_{r\beta}$: $\alpha-\beta$ axis rotor flux
J_{wR} and J_{wL}: right and left wheel moment of inertia
k_A and k_S: reduction factors in the adhesion and slip area
L_m: mutual inductance
L_r and L_s: rotor and stator self-inductance
n_i: gear reduction ratio
n_p : number of the pole pairs
N: number of unknown variables or number of samples
P_i: previous best position of each particle
Q and R: process and measurement noise covariance matrixes
r: wheel radius
R_r and R_s: rotor and stator resistance
μ_f: traction coefficient
T_m: motor torque
T_L: load torque
V: longitudinal velocity
$v(t)$ and $w(t)$: measurement and process noise
V_i, X_i: velocity and position of ith particle
w: inertia weight factor
ϵ: gradient of tangential stress
ξ: creepage between the wheel and rail
$\omega_{m,}\omega_w$: motor and angular velocity

I. Introduction

Locomotive design, which was introduced more than 200 years ago, is still developing and in progress. Based on the type of energy usage, railway vehicles are divided into three classes: steam, diesel-fueled, and electric. In steam locomotives, steam energy is provided by the combustion of fuels. Since steam locomotives cannot be loaded with over a certain amount of fuel, they cannot operate at long distances. So, the application of the steam system in this vehicle has been completely obsolete. The source of energy in diesel-fueled locomotives is diesel motors. According to the fuel tank, a diesel train that pulls ten wagons can take approximately 600-700 km distance. Unlike these two types, electric locomotives have no refueling problems, so they are suitable for traveling long distances. Another advantage of these locomotives is that they are the most economical locomotives because of their tractive effort.

Progress in science and technology, especially in the field of computer modeling, has allowed the adoption of new and advanced forms of traction systems for railway vehicles. However, the performance of the locomotive traction system is limited by the adhesion condition between the wheel and the rail. Adhesion is the key element for determining optimal traction performance. Moreover, adhesion affects the passengers' comfort, the safety of transportation equipment, and railway vehicles' energy management. Wheel shape and size and rail contact area directly influence the motion of railway vehicles. The Hertzian theory is one of the methods widely used to find the contact patch shape and size. This theory includes some assumptions such as non-conformal elliptical contact (valid if dimensions of the contact area are smaller than the curvatures of surfaces), frictionless surfaces, and elastic half-spaces. It is worth noting that the dynamics of railway wheelsets are influenced by different factors. This impactability and uncertain variations in the contact condition complicate the mechanical system of railway wheelsets significantly.

The interaction of the vehicle and track is affected by four main factors: suspension characteristics, metallurgy, contact mechanics, and friction. The wheel-rail interaction is the most important issue in the dynamics of railway vehicles. Any changes in the contact condition can trigger subsequent changes in the braking and traction responses of the rail vehicle [1], especially when the rail and/or wheel contact surfaces are subject to environmental factors such as dirt [2], water, deliberately applied friction modifiers [3], weather conditions [4], or contact surface temperatures [5-7], leading to the well-known problem of low adhesion. Slip/slide, which can potentially cause severe wear of wheel and rail surfaces and increase mechanical stress in the system, is caused by low adhesion. Wheels slip in traction or slide in braking if they deliver a higher force to the rail than they can transmit. Meanwhile, instability and inconsistent traction performance, which cause problems in train schedules, are negative effects of low adhesion. If creepage at the wheel-rail interface increases, the temperature will increase in the contact areas and it will decrease the coefficient of friction, resulting in the creation of flatness, shelling, and skid marks on the wheels and rails, which also suffer from wheel burns and deterioration caused by damaged wheels. As a result, the rails need regrinding, and the wheelsets need reprofiling or replacing, which imposes additional costs on the rail industry. Adhesion estimation in wheel-rail contact area during train operation, which is an important task for railway industries, is a multifaceted process as it depends on several operational factors that influence nonlinear processes at the wheel-rail contact interface. To characterize the braking and traction, which are key elements of performance and safety issues, accurate information about the adhesion is necessary [8].

There are many approaches proposed by researchers to studying adhesion. Investigating the lateral dynamics, specific types of friction conditions (dry or wet), or single wheelsets are methods mentioned in [9-11] for surveying the wheel-rail interface. To control the wheel rotational acceleration below a pre-defined threshold, controlling the measured slip ratio (relative speed between the train and wheel) is noted in commonly used wheel slip protection schemes [12-14]. The operational rail self-cleaning mechanism [15], axle load distributions, vehicle speed, and track irregularities are other train operational factors that researchers consider in adhesion estimation. Additionally, rail vehicle design has a significant effect on adhesion [16]. In [17], a single wheelset velocity was used as Kalman filter input to detect adhesion force for slip control purposes. This model has, also, been applied to detect wheel slip/slide and re-adhesion control of AC traction motors in railway applications [18]. To suppress the slide and slip and adjust the torque command, a multiple-induction motor single inverter has been investigated to estimate the adhesion force [19,20]. Extended Kalman filter (EKF)-based estimation of creepage, creep force, and friction coefficient between the wheel and rail surfaces by utilizing the stator voltage, current, and speed of the traction AC motor was proposed in [21]. Another method to detect slip velocity is multi-rate EKF state identification. In this method, traction motor load torque is identified by combining the multi-rate method and the EKF method. Faster detection of slip and reliability and traction performance improvement are benefits of this approach [22].

Estimation of the rotor fluxes, currents, and motor speed for direct vector control of induction motors in the implementation of the EKF algorithm was proposed in [23]. For the system to operate at the optimal state, proper selection of measurement noises and covariance matrices is an important problem associated with the use of EKF. It is worth noting that both matrices are not known, especially

since it is very difficult to define the system noise. Therefore, these matrices are often used as parameters for tuning. The adjustment can be made by using evolutionary algorithms or a trial-and-error approach [24]. Adhesion can be estimated by focusing on longitudinal dynamics and associated adhesion effects. In this method, an observer is designed, and nonlinear wheel-rail contact is considered. To cover this nonlinearity, EKF was combined with a parameter estimator [25]. It should be noted that EKF estimation is directly related to the correct selection of system and measurement noise covariance matrices. Due to the unknown stochastic properties of the corresponding noises in EKF, it is not possible to obtain the mathematical relationship between the EKF performance and the noise covariance matrices. Therefore, researchers have proposed different methods to determine these matrices in the literature. These methods have classified the matrices into constant and dynamic. In the first classification, matrices are determined by the trial-and-error method [26-29]. This approach is not only time-consuming but also does not yield optimum results for the whole speed range. In [30], an unscented Kalman filter (UKF) was employed for IM state estimation and the results were compared with EKF, which showed that at the beginning of the simulation, UKF outperformed EKF but when the input torque was changed, EKF started to outperform UKF. The next group of studies has performed off-line optimization of these matrices by focusing on heuristic algorithms such as differential evolution [31-32] and genetic algorithms [33].

Unlike conventional optimization algorithms such as Newton-Rapson and Levenberg-Marquardt, which require mathematical expressions and their derivatives, heuristic algorithms provide derivative-free global optimization using only fitness functions and fitness values [33]. Because of the offline optimization process, the optimization method is time-consuming like the trial-and-error method. Meanwhile, the operating conditions of the induction motor affect these matrices, so they must be updated depending on the working conditions. Therefore, the second group of studies [34-37] has proposed the capability of online updating of these matrices. Some of these studies [35,37] have used the fuzzy logic approach to update these matrices. Knowledge and experience of an expert are two key factors to achieve high performance estimations with this method, so its design process is quite complicated.

Model-based adhesion estimation (which is based on the contact forces and moments analysis) is another method used in the literature. Due to the dependence of creep forces and moments on the level of track irregularities, it is difficult to illustrate adhesion conditions without prior knowledge of the track irregularities. To solve such a problem, the estimation of adhesion conditions based on the eigenvalue analysis without prior knowledge of the track irregularity level was proposed [38]. The non-model-based estimation scheme compares the dynamic responses of leading and trailing wheelsets using the yaw positions of the leading and trailing bogies [39]. In general, simulation methodology used for rail vehicles' traction system can be divided into the following simulation stages: simulation of the mechanical system [40-42], simulation of the longitudinal dynamics of the train [40-41], simulation and modeling of the electrical and traction control systems [43-44], creep force modeling at the wheel-rail interface [45-50], simulation of the full mechatronic system of a locomotive [41,51-52], and validation and verification of the results [40,53-54].

PSO is an evolutionary computation method that is used to optimize nonlinear systems [55]. This approach was first introduced in [56], and since then, it has been considered one of the most popular optimization methods in the literature. In [57], the PSO algorithm is used to optimize the objective function to reach the best parameters and variables of controllers. In [58], the use of the PSO algorithm in railway studies is reviewed, but the use of PSO for adhesion and creep force modeling is not mentioned. PSO is preferred due to its simplicity and the high nonlinearity in adhesion and creep force models. To demonstrate the level of agreement between adhesion and creep force models and measurements, PSO-based parameterization of adhesion and creep force models is proposed in [59]. Swarm intelligence-based adhesion estimation algorithm allows determining the adhesion optimum between wheel and rail. Therefore, the reference slip value for the controller can be determined according to the adhesion conditions, which leads to an effective wheel slip control performance [60].

Among the state observer mentioned above, EKF is an accurate estimator. The disadvantage of EKF is that its effectiveness heavily depends on the covariance matrices of the measurement and system noises, which are critical parameters for torque and speed estimation of induction motors and usually could not be acquired accurately. Thus, several intelligent optimization algorithms have been proposed to enhance the EKF performance. In this paper, the PSO algorithm is employed to optimize EKF for torque (which has a linear relation with adhesion force) and estimate the speed of the induction motor. The main contributions of this paper are (1) the formulation of a mathematical model for the torque estimation of an induction motor for wheel-rail adhesion estimation, (2) the successful employment of the PSO algorithm to optimize EKF covariance matrices, and (3) the construction and implementation of a simulation model in Matlab to evaluate the performance of PSO-EKF. The effectiveness of the proposed approach for adhesion estimation is verified through simulation experiments, and its superiority in the estimation of variables compared to conventional EKF is proved.

The rest of this paper is organized into five sections. Section II introduces the principle concepts of PSO. Section

III gives the details of the traction system and the sixth-order mathematical model of the induction motor. The PSO-based EKF framework is presented in Section IV. Section V provides the details of the experimental results in the implementation of EKF. Finally, Section VI presents the conclusion.

II. Particle Swarm Optimization Concepts

PSO is a metaheuristic algorithm that optimizes a problem by iteratively trying to improve a candidate solution with regard to a given measure of quality. PSO is motivated by the intelligent collective behavior of some animals, such as bird flocking and fish schooling. This optimization algorithm exploits the concepts of social sharing of information in which the population is called a swarm, and each individual in the swarm is called a particle. In PSO, to improve the results for a defined objective function, an iterative procedure is followed and the particles move in the search space based on the reasoning as follows.

First, they evaluate their fitness continuously and in each iteration, memorize the best position that they have ever had in their movement history. Second, knowing the position of the best particle in the swarm, particles move in the n-dimensional space, foraging the solution.

Particles in the swarm are in communication with each other and update the mentioned parameters in each iteration. While moving toward the best position, they change their position and velocity based on the local and global best information. Local best refers to the best position of each particle in its movement history, and the best position of the whole group is called global best which is updated in each iteration. Therefore, the whole group would have sufficient knowledge about the position of the new global best, if the best position is changed. All the particles in the swarm search areas near the global best and try to move toward them. This phenomenon is called convergence.

Small values of the inertia weight allow all particles to reduce their speed so that when they reach the area of the global best, their speed converges to zero. When unpleasant convergence occurs, we can give the particles a new set of initial values to get rid of this unpleasant situation. PSO has two advantages over the GA algorithm. First, in PSO, particles decide about the next movement in the space by using their history and the best of the group history but in GA, transferring the knowledge of the current group to the next is completely hereditary. It is obvious that random procedures of cross-over and mutation affect this inheritance, and pure knowledge is not transferred from one generation to the next; hence, PSO is more reliable and faster than GA. Second, death and reborn of the particles in GA, in each iteration, cause computational burden on the system to arise whereas in PSO, the population of the particles is constant and particles only update their position and velocity, so there is no computational burden problem.

III. Traction System and Discrete-Time Mathematical Model

In the simulated system used in this research, a wheelset with two wheels is driven by an AC induction motor through a gear set. The details of the traction system are presented in Fig.1.

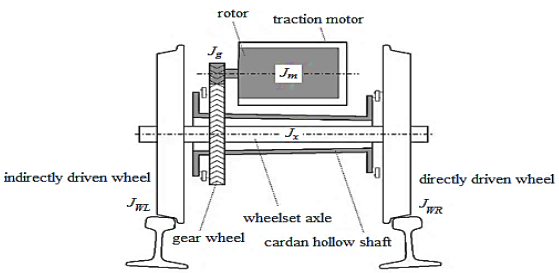

Fig. 1. The schematic of the traction system.

The wheels are driven by the creep forces generated at the contact patch between the wheels and the rail. Hence, the dynamic equations are given as:

$$\omega_w = \frac{\omega_m}{n_i} \quad (1)$$

$$\frac{d\omega_m}{dt} = \frac{T_m - T_L}{J_{eqv}} \quad (2)$$

where ω_w is the wheel's angular velocity, ω_m is the motor's angular velocity, n_i is the gear reduction ratio, T_m is the motor torque, and T_L and J_{eqv} are the load torque and the equivalent moment of inertia, respectively represented as:

$$T_m = \frac{n_p L_m}{L_r}(I_{s\beta}\psi_{r\alpha} - I_{s\alpha}\psi_{r\beta}) \quad (3)$$

$$T_L = \frac{2rF_a}{n_i} \quad (4)$$

$$J_{eqv} = J_m + \frac{J_g + J_x + J_{wR} + J_{wL}}{n_i^2} \quad (5)$$

where Fa is the longitudinal creep force or adhesion force of a single wheel and J_g, J_x, J_{wR}, J_{wL} are the moment of inertia of the gearbox, wheelset axle, right wheel, and left wheel, respectively.

In this paper, the sixth-order rotor flux-based induction motor model is used in the EKF algorithm to estimate $I_{s\alpha}$, $I_{s\beta}$, $\psi_{r\alpha}$, $\psi_{r\beta}$, ω_m, and T_L. In this modeling, the state variables are stator current, rotor flux, angular velocity of the motor, and load torque. The state space representation of such a model can be written as follows [61]:

$$\frac{dx(t)}{dt} = AX(t) + Bu(t) + \mathrm{w(t)} \quad (6)$$

$$y(t) = CX(t) + v(t) \quad (7)$$

$$X = [I_{s\alpha} \quad I_{s\beta} \quad \psi_{r\alpha} \quad \psi_{r\beta} \quad \omega_m \quad T_L]^T \quad (8)$$

$$y = [I_{s\alpha} \quad I_{s\beta}]^T \quad (9)$$

$$u = [u_{s\alpha} \quad u_{s\beta}]^T \quad (10)$$

$$A=\begin{bmatrix} -\left(\frac{R_s}{\sigma L_s}+\frac{L_m^2 R_r}{\sigma L_s L_r^2}\right) & 0 & \frac{L_m R_r}{\sigma L_s L_r^2} & \frac{L_m}{\sigma L_s L_r} n_p \omega_m & 0 & 0 \\ 0 & -\left(\frac{R_s}{\sigma L_s}+\frac{L_m^2 R_r}{\sigma L_s L_r^2}\right) & -\frac{L_m}{\sigma L_s L_r} n_p \omega_m & \frac{L_m R_r}{\sigma L_s L_r^2} & 0 & 0 \\ \frac{R_r L_m}{L_r} & 0 & -\frac{R_r}{L_r} & -n_p \omega_m & 0 & 0 \\ 0 & \frac{R_r L_m}{L_r} & n_p \omega_m & -\frac{R_r}{L_r} & 0 & 0 \\ \frac{-3 n_p L_m}{2 J_{eqv} L_r}\psi_{r\beta} & \frac{3 n_p L_m}{2 J_{eqv} L_r}\psi_{r\alpha} & 0 & 0 & -\frac{C_v}{J_{eqv}} & -\frac{1}{J_{eqv}} \\ 0 & 0 & 0 & 0 & 0 & 0 \end{bmatrix} \quad (11)$$

$$B=\begin{bmatrix} \frac{1}{\sigma L_s} & 0 \\ 0 & \frac{1}{\sigma L_s} \\ 0 & 0 \\ 0 & 0 \\ 0 & 0 \\ 0 & 0 \end{bmatrix} \quad (12)$$

$$C=\begin{bmatrix} 1 & 0 & 0 & 0 & 0 & 0 \\ 0 & 1 & 0 & 0 & 0 & 0 \end{bmatrix} \quad (13)$$

$$\sigma = 1-\frac{L_m^2}{L_s L_r} \quad (14)$$

where R_s is the stator resistance, R_r is the rotor resistance, L_s is the stator self-inductance, L_r is the rotor self-inductance, L_m is the mutual inductance, n_p is the number of the pole pairs, σ is the leakage coefficient, and C_v is the viscous friction. The extended model of IM can be represented by (15) and (16).

$$\begin{bmatrix} \dot{I}_{s\alpha} \\ \dot{I}_{s\beta} \\ \dot{\psi}_{r\alpha} \\ \dot{\psi}_{r\beta} \\ \dot{\omega}_m \\ \dot{T}_L \end{bmatrix} = A\begin{bmatrix} I_{s\alpha} \\ I_{s\beta} \\ \psi_{r\alpha} \\ \psi_{r\beta} \\ \omega_m \\ T_L \end{bmatrix} + \begin{bmatrix} \frac{1}{\sigma L_s} & 0 \\ 0 & \frac{1}{\sigma L_s} \\ 0 & 0 \\ 0 & 0 \\ 0 & 0 \\ 0 & 0 \end{bmatrix}\begin{bmatrix} U_{s\alpha} \\ U_{s\beta} \end{bmatrix} + w(t) \quad (15)$$

$$\begin{bmatrix} I_{s\alpha} \\ I_{s\beta} \end{bmatrix} = \begin{bmatrix} 1 & 0 & 0 & 0 & 0 & 0 \\ 0 & 1 & 0 & 0 & 0 & 0 \end{bmatrix}\begin{bmatrix} I_{s\alpha} \\ I_{s\beta} \\ \psi_{r\alpha} \\ \psi_{r\beta} \\ \omega_m \\ T_L \end{bmatrix} + v(t) \quad (16)$$

where $w(t)$ and $v(t)$ are the process and measurement noise, respectively.

$$F_a = \frac{2F_N\mu_f}{\pi}\left(\frac{k_A\epsilon}{1+(k_A\epsilon)^2} + \arctan(k_S\epsilon)\right),\ k_S \le k_A \le 1 \quad (17)$$

F_a at the wheel-rail contact is modeled by Polach's method [62], which has been widely used in commercial codes owing to its short computational time and satisfactory accuracy compared with other methods.

$$\epsilon = \frac{G\pi ab C_{11}}{4F_N\mu_f} \quad (18)$$

$$\xi = \sqrt{\xi_x^2+\xi_y^2} \qquad \xi \approx \xi_x,\ \xi_y \approx \quad (19)$$

where F_N is the normal force between the wheel and rail, μ_f is the traction coefficient, k_A and k_S are different reduction factors in the areas of adhesion and slip, respectively, G is the shear module, a and b are the semi-axis lengths of the contact patch, C11 is the Kalker coefficient, and ξ is the creepage between the wheel and rail. In this paper, the creepage terms contain only the longitudinal component, and the lateral dynamics of the system are neglected. This creepage was calculated by the following equation [63]:

$$\xi = \frac{\omega_w r - V}{V} \quad (20)$$

where V is the longitudinal velocity of the train. The traction coefficient in (17) depends on the slip velocity (ξV) and friction coefficient, which is expressed by the following equation:

$$\mu_f = \mu_0((1-D)e^{-B\xi V} + +D \quad (21)$$

where D and B are reduction factors under different friction coefficients.

IV. Wheel-rail Adhesion Estimation using PSO- EKF

In this paper, we attempt to find the best linear estimation of the state vector of the induction motor to estimate the adhesion force between the wheel and rail surfaces. The state and measurement equations are given as follows:

$$F_e(k) = \frac{\partial f_e(x_e(k).u_e(k))}{\partial x_e(k)}\Big|\hat{x}_e(k).\hat{u}_e(k) \quad (22)$$

$$F_u(k) = \frac{\partial f_e(x_e(k).u_e(k))}{\partial u_e(k)}\Big|\hat{x}_e(k).\hat{u}_e(k) \quad (23)$$

$$P^-(k+1) = F_e(k)P_k(k)(F_e(k))^T + F_u(k)D_u(k)$$
$$(F_u(k))^T + Q(k) \quad (24)$$

$$K(k) = P^-(k+1)H^T(HP^-(k+1)H^T + R(k))^{-1} \quad (25)$$

$$\hat{x}_e(k+1) = \hat{f}_e\big(x_e(k).\hat{u}_e(k)\big) + K(k)(z(k) - H\hat{x}_e(k)) \quad (26)$$

$$P(k+1) = (I - K(k)H)P^-(k+1) \quad (27)$$

where Q and R are the covariance matrixes of process and measurement noise and I is the unit matrix symbol. Due to the uncertainty of Q and R, their values are obtained by trial-and-error methods which are very tedious procedures. The values of these matrixes have a significant effect on the EKF output. This is considered a defect for this type of estimator. To overcome this problem and to avoid the

computational complexity of the trial-and-error method, we use both EKF and PSO techniques and try to tune Q and R. In the literature, the trial-and-error method is used to tune the covariance matrices of EKF, which is a very laborious task. To surmount this problem, genetic algorithms have been used to optimize and tune the two matrices automatically [64]. In this work, EKF is designed and implemented for the estimation of motor torque with randomly selected values of Q and R. To optimize the EKF-based torque estimation of the induction motor and avoid the difficulty of determining Q and R, an alternative method is used in which the two matrices are tuned and optimized based on PSO. This approach consists of two steps. It first allows finding the optimal values of Q and R, and then these values are injected into the EKF estimator to estimate motor parameters.

In PSO, all particles fly all over a multidimensional search space and adjust their position according to their own experience and that of neighbors. The position of the i^{th} particle (X_i), the previous best position of each particle (P_i), and the individual velocity (V_i) that each particle moves in the swarm are defined as follows:

$$X_i = (x_{i1}, x_{i2}, \ldots, x_{iN}) \quad (28)$$

$$P_i = (p_{i1}, p_{i2}, \ldots, p_{iN}) \quad (29)$$

$$V_i = (v_{i1}, v_{i2}, \ldots, v_{iN}) \quad (30)$$

where i and N denote the i^{th} particle and dimension of the problem or the number of unknown variables, respectively. In PSO, initialization is done with a group of random particles and it is tried to find the optimum value by updating generations. Each particle is updated by two best values in every iteration: 1) the best position that each particle achieved so far during the optimization process or pbest and 2) the best position ever achieved by any particle in the population or gbest. After finding the two best values, the position and the velocity of each particle in the k^{th} iteration are updated by the following equations in the inertia weight approach (IWA):

$$v_i(k+1) = \underbrace{w.v_i(k)}_{\text{Current motion}} + \underbrace{c_1.r_1(k).(p_i(k) - x_i(k))}_{\text{Personal influence}} + \underbrace{c_2.r_2(k).(p_g(k) - x_i(k)}_{\text{Social influence}} \quad (31)$$

$$x_i(k+1) = x_i(k) + v_i(k+1) \quad (32)$$

where w is the inertia weight factor that controls the impact of the previous velocity on the new velocity, v_i is the velocity of the i^{th} particle, c_1 and c_2 are the positive constants, called coefficients of the self-recognition and social component and determine which controls the relative impact of the local and the global knowledge on the movement of each particle respectively, r_1 and r_2 are two random numbers used to maintain the diversity of the population and uniformly distributed in the interval [0,1], p_i is pbest of the i^{th} particle, x_i is the current position of the i^{th} particle, and p_g is gbest of the swarm.

The velocity is updated by Eq. (31) from the previous velocity to the new one. The new position of each particle is determined by Eq. (32) which is the sum of the previous position and the new velocity. Tuning of Q and R is necessary to achieve the best estimations. Any changes in these two parameters affect both the steady-state and transient duration operation of EKF. If Q increases, large state noises or uncertainties in the machine will be inevitable, which will cause higher Kalman gain, faster EKF transient performance, and more heavily weighted measurements. Strong noise measurements, weighted less noise, decreased Kalman gain, and slower transient performance are the consequences of increased R.

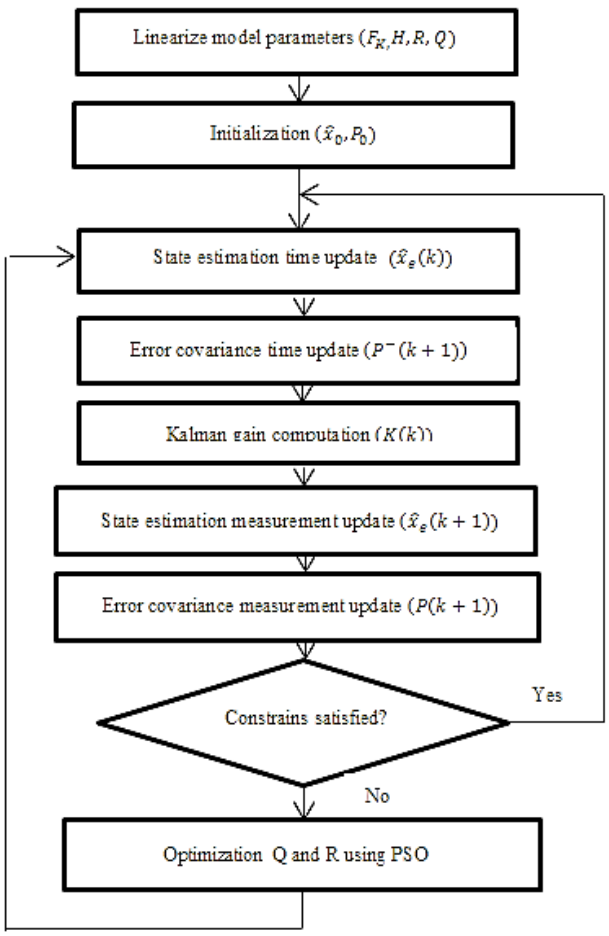

Fig 2. The PSO-EKF algorithm flowchart

Therefore, in the first step, the optimal values of Q and R are found. Then, these values of Q and R are injected into the EKF estimator to estimate the rotor speed and torque of the induction motor. For comparison purposes, the performance of EKF is evaluated by the fitness function between the estimated current and the actual stator current as Eq. (33). The manual adjustment of EKF is simple to implement, but the process is time-consuming. So, to obtain satisfactory

estimation performance, an experienced operator is needed. In this work, PSO- EKF is used to get the optimal covariance matrices. In the optimization of covariance matrices, the elements of system noise and measurement noise covariance matrices are regulated under some performance index, i.e. fitness function. The stator current can be measured by using current sensors. Smaller differences between the measured and the estimated current imply more accurate torque and speed estimation of the induction motor. These difference values of stator current can be adopted as the fitness function,
which must be minimized as below:

$$\min \ J=\frac{1}{N}\sum_{k=0}^{N}\|i_s(k)-\hat{\imath}_s(k)\|_2^2 \qquad (33)$$

where N is the number of samples involved in the optimization, i_s is the actual stator current, $\hat{\imath}_s$ is the estimated stator current, and $\|.\|_2$ is the Euclidean distance.

PSO has six main steps. 1) Each particle in the swarm starts to move with random velocity and position in N dimensions of the problem space. 2) Fitness of each particle is evaluated. 3) Velocity and position of each particle are changed according to Eq. (31) and (32), respectively. 4) The lbest (local best) and gbest will be updated if necessary; the updated position of each particle is evaluated according to its fitness. 5) If the criterion is met, the optimization process ends; otherwise, it goes to step 3 and the steps are repeated. 6) The best global solution results from this optimization process.

In this paper, the PSO-EKF method is utilized to evaluate the accuracy compared with EKF in estimating variables. The method is composed of two steps. At first, a PSO-based EKF structure is presented which allows for finding the optimal values of Q and R. In the second step, these optimal values are injected into the EKF estimator to estimate the torque, which leads to adhesion force estimation. The block diagram of the PSO-EKF parameter estimation system is illustrated in Fig.2. Also, the pseudo-code for PSO-EKF is shown in Appendix A.

V. Results and simulation

This section aims to evaluate the accuracy of EKF in estimating the variables. To demonstrate the performance of the proposed PSO-EKF approach, adhesion force in different wheel-rail contact conditions and induction motors are simulated using Matlab software. Note that the sampling period we used to write our codes in Matlab language is 10^{-3} s.

To simulate dry, wet, low, and very low contact conditions between the wheel and rail, friction coefficients are designed as follows:

$$\mu_0 = \begin{cases} 0.55 & t < 10 \\ 0.3 & 10 \le t < 20 \\ 0.06 & 20 \le t < 30 \\ 0.03 & 30 \le t < 35 \end{cases}$$

Q and R can be given as:
Q = diag ([1e-11 1e-9 1.39e-12 1e-9 1.85e-6 1.42e-6])×0.02
R = diag ([4e-3 4e-3])

The values of k_A, k_S, D, and B under different friction conditions are listed in Table 1.

TABLE 1
POLACH MODEL PARAMETERS UNDER DIFFERENT FRICTION CONDITIONS [18]

Model parameter	Wheel–rail conditions			
	Dry	Wet	Low	Very Low
k_A	1	1	1	1
k_S	0.4	0.4	0.4	0.4
D	0.6	0.2	0.2	0.1
B	0.4	0.4	0.4	0.4

The parameters used in the simulation are listed in Table 2. Fig.3 shows the curves of the adhesion force versus creepage in different wheel-rail contact conditions. As is seen in this figure, the creepage curve has a nonlinear characteristic. The area on the right side of the peak is called the creepage zone and the area on the left side of the peak is the adhesion zone.

TABLE 2
PARAMETERS AND VALUES USED IN THE SIMULATION

f (Hz)	L_S(H)	L_m(H)	L_r(H)	R_r (Ω)	R_S (Ω)
50	0.1004	0.0915	0.0969	1.294	1.54
r (m)	G ($\frac{N}{m^2}$)	C_{11}	F_N (kN)	J_{eqv} (kg.m^2)	C_v ($\frac{N.m}{rad.s}$)
0.34	8.4×10^{10}	4.12	50	0.07	0.015
V($\frac{m}{s}$)	b (m)	n_p	a (m)	n_i	
15	0.0075	3	0.0015	6.92	

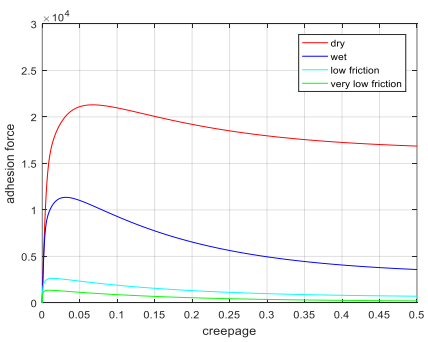

Fig.3. Adhesion force–creepage curves.

The creepage zone is the non-stable part of the curve, and adhesion decreases when the creepage increases. On the other hand, the adhesion zone is the stable part of the curve, in which adhesion increases when the creepage increases. Increasing the creepage, the slip region increases versus the

stick region.

In the next step, induction motor parameters are estimated using EKF, and their actual and estimated trajectories are compared separately to check the degree of estimation accuracy and convergence. Estimated stator currents in $\boldsymbol{\alpha}$ and $\boldsymbol{\beta}$ frames ($\hat{\boldsymbol{I}}_{\boldsymbol{s\alpha}}$, $\hat{\boldsymbol{I}}_{\boldsymbol{s\beta}}$) with their actual trajectory are presented in Figs.4 (a) and (b), respectively. The trajectory of the estimated and actual rotor fluxes in $\boldsymbol{\alpha}$ and $\boldsymbol{\beta}$ frames ($\hat{\boldsymbol{\psi}}_{\boldsymbol{r\alpha}}$,$\hat{\boldsymbol{\psi}}_{\boldsymbol{r\beta}}$)are displayed in Figs.5 (a) and (b), respectively.

It can be seen in Figs.4 and 5 that the presence of an error in the estimated trajectories of the stator current and rotor flux relative to the actual trajectories of these two variables is inevitable.

The estimated and actual motor speeds (ω_m,$\hat{\omega}_m$) are given in Fig.6 according to which the EKF estimator tracks the speed trajectory with a lower bound of error and converges fast. Despite good convergence, according to the simulation observations, any changes in the values of the noise and process covariance matrices will lead to significant changes in the estimated trajectory of motor speed.

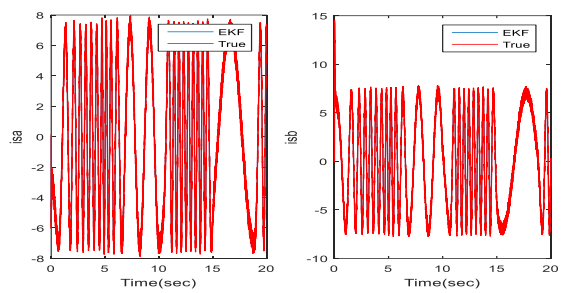

Fig.4.The trajectories of the estimated and actual motor currents (a) in α axis (b) in β axis.

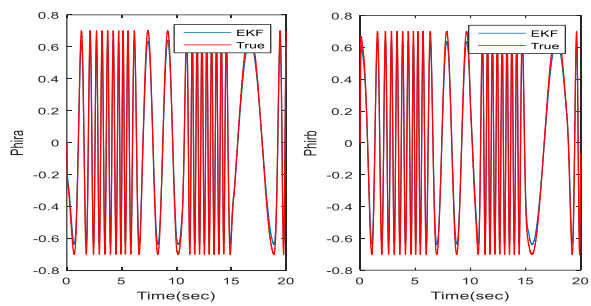

Fig.5. The trajectories of the estimated and actual rotor fluxes (a) in α axis (b) in β axis

The trajectory of the estimated and actual load torque (T_L , $\hat{T}_L$) is presented in Fig.7. According to the linear relationship between the load torque and the adhesion force expressed in Eq. 4, the estimated adhesion force trajectory is obtained as shown in Fig.8. Contrary to the relatively good convergence between the estimated and actual motor speed trajectory, we are faced with a high error band in the estimated and actual load torque trajectory. To overcome this error and achieve the desired trajectory, it is necessary to change the system and process noise covariance matrices' values. Achieving such values will be possible using trial and error, which is a time-consuming approach.

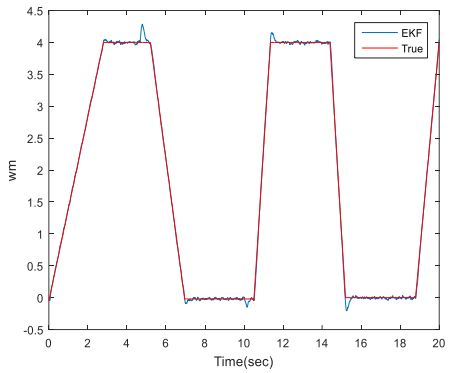

Fig.6. The trajectory of the estimated and actual motor speed.

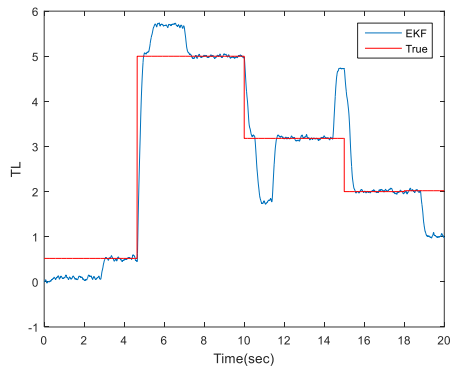

Fig.7. The trajectory of the estimated and actual load torque.

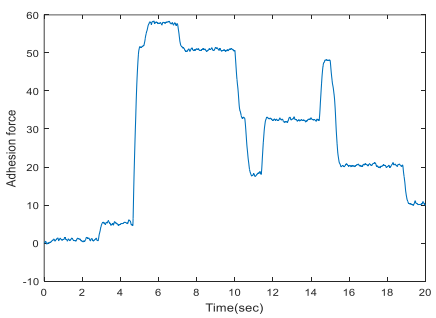

Fig.8. The trajectory of the estimated adhesion force.

It can be seen from the simulation results that estimating the variables using EKF cannot provide the necessary accuracy and convergence in load torque and speed estimation, which are the most important factors in estimating wheel and rail adhesion. As a result, using an integrated method to eliminate these drawbacks can play an essential role in achieving the desired result. As was already mentioned, the key problem of EKF is that the covariance matrices Q and R have a great effect on the estimation results. Bad choices of these two matrices will lead to large estimation errors or the result of estimation divergent. Tuning of Q and R will yield the best estimations.

In this section, we try to tune and optimize Q and R based on the PSO algorithm. It is worth noting that the convergence of the PSO method to the optimal solution depends on the three parameters of c1, c2, and w in Eq. (31). During simulations, c1, c2, and w are set to 2, 2, and 1, respectively and swarm population is set to five particles. In the following, we will show the simulation results obtained by our proposed approach PSO- EKF. The optimized parameters of EKF obtained by our proposed approach are as follows:

QR = [(1e-8)/5 (1e-6)/5 (1.39e-9)/5 (1e-6)/4
(1.85e-3)/4 (1.42e-2)/4 4e-3 4e-3]×3e-6

PSO- EKF stator currents in α and β frames with their actual trajectories are presented in Figs.9 (a) and (b), respectively. The trajectories of PSO- EKF and actual rotor fluxes in α and β frames are displayed in Figs.10 (a) and (b), respectively.

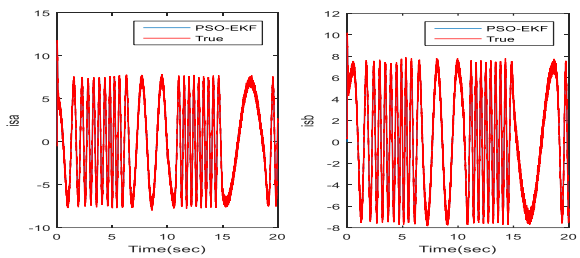

Fig.9. The trajectories of the PSO- EKF and actual motor currents (a) in α axis (b) in β axis.

It can be seen in Figs.9 and 10, the trajectories of the stator current and rotor flux relative to the actual trajectories of these two variables have suitable convergence.

PSO-EKF and actual trajectories of induction motor speed are depicted in Fig.11. The trajectories of - EKF and actual load torque are presented in Fig.12.

Figs.11 and 12 show that the proposed estimator tracks the speed and torque trajectories with a lower bound of error and converges fast. As can be seen, when sudden changes happen in the speed and torque, the error changes in a narrow band interval. Therefore, the tuned estimator tracks the state trajectories with higher precision and converges fast.

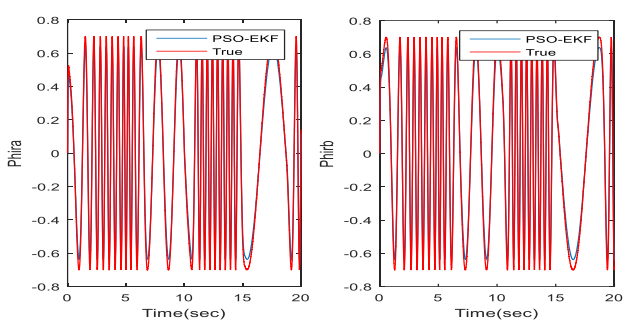

Fig.10. The trajectories of the PSO- EKF and actual rotor fluxes (a) in α axis (b) in β axis

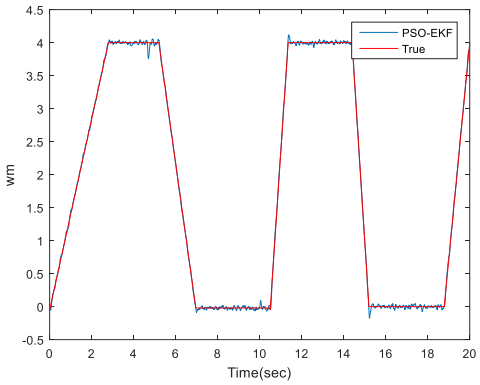

Fig.11. Trajectory of the PSO- EKF and actual motor speed.

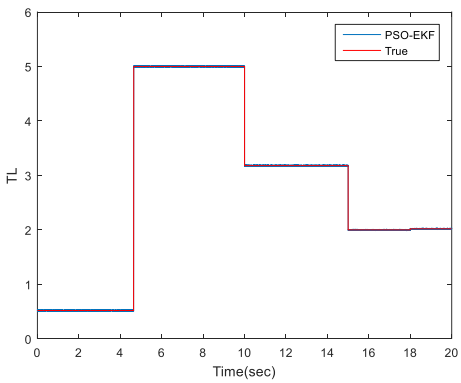

Fig.12. The trajectory of the estimated and actual load torque.

The PSO-EKF adhesion force trajectory is shown in Fig. 13, which is derived from the part of Eq. (4).

The estimated longitudinal creep force makes it possible to determine the level of adhesion that is present between the wheel and the rail. The simulation results show that the proposed approach gives desired output within 5 iterations compared to the trial-and-error approach. In Figs. 9-12, the simulation results relative to the best optimal values of EKF parameters are plotted, which show good convergence between the estimated and actual states. In spite of relatively good convergence between trajectories in the proposed approach, tuning of EKF is time-consuming and challenging.

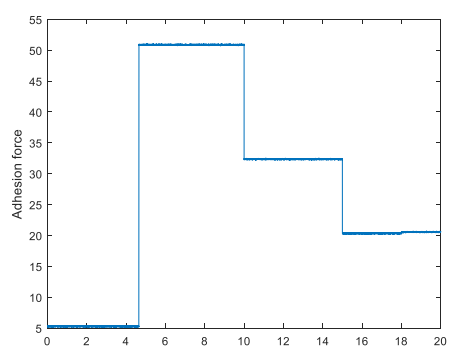

Fig.13. The trajectory of the estimated adhesion force

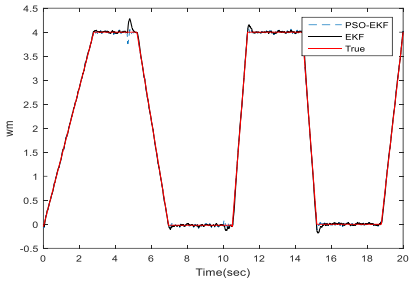

(a)

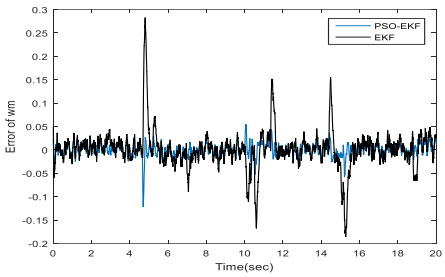

(b)

Fig.14. The speed estimation results for EKF PSO-EKF (a) Estimated speed (b) speed estimation error

A. Performance Comparison

To further show the effectiveness of PSO-EKF, its performance is compared with EKF in Figs.14-15. Considering the resulting estimation performances, the proposed method outperforms EKF because it does not require a priori knowledge of the noises. In addition, in the proposed method, the process covariance is tuned adaptively. The Q matrix in EKF is selected by the trial-and-error method, so it deteriorates the estimation performance of EKF. In addition, it is quite difficult to determine Q that gives sufficient estimation performance by the trial-and-error method.

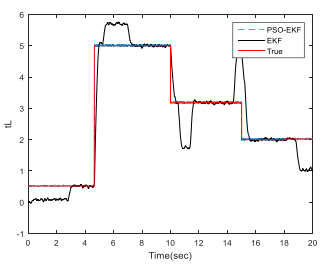

(a)

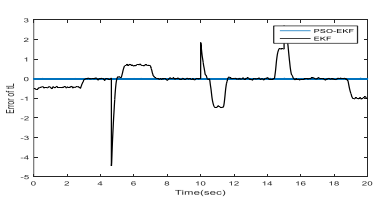

(b)

Fig.15. Load torque estimation results for EKF PSO-EKF (a) Estimated load torque and (b) load torque estimation error

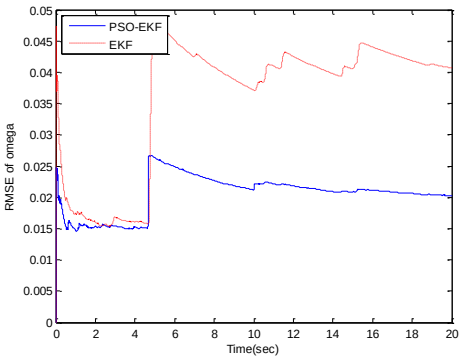

Fig.16. RMSE of Omega over time

To further evaluate the estimations accuracy of the approaches, the root mean square error (RMSE) speed and load torque occurring in estimations are given in Figs. 16-19. RMSE is obtained over 40 Monte Carlo runs. The RMSE of estimations over time is shown in Figs.16 and 17 and their mean and variance are shown in Figs. 18 and 19. Each bar in Figs. 18 and 19 represents the mean and variance of RMSE. It can be found that PSO-EKF outperforms EKF in terms of the mean and variance of RMSE. It can be seen that the RMSE of PSO-EKF is smaller than the RMSE of EKF, so it can be deduced that the speed and load torque estimated by PSO-EKF is closer to their actual values. As a result, the adhesion force estimated using PSO-EKF is more accurate.

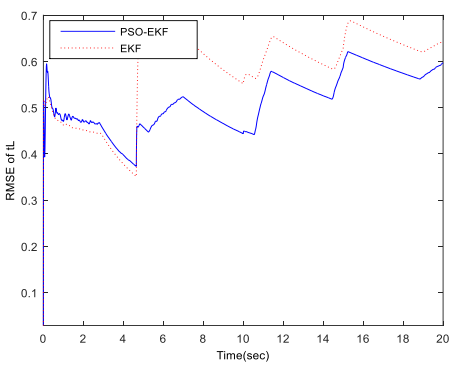

Fig.17. The RMSE of the load torque over time

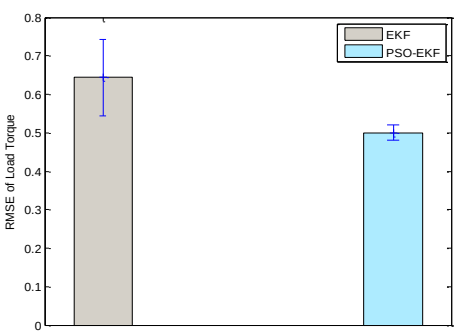

Fig.18. The RMSE of the load torque

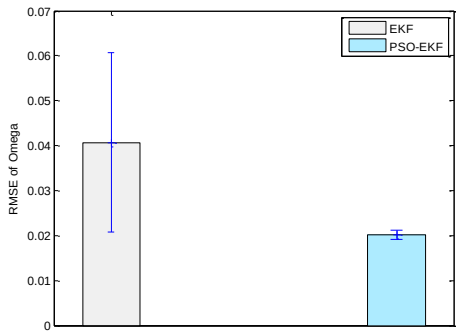

Fig.19. The RMSE of Omega

TABLE3
RUNNING TIME FOR EKF AND PSO-EKF

Method	Running Time(Sec)
EKF	15
PSO-EKF	20

To provide a comprehensive comparison of the methods, we provide the computational time for each method in Table 3. It shows that the cost for this improvement is in the slightly increased computational load in PSO EKF. However, this fact is insignificant if the poor performance of EKF is taken into account.

VI. Conclusions

EKF is based on system linearization and requires a Jacobian matrix in this process. The calculation of the Jacobian matrix is a difficult and error-prone operation. As we saw in the simulation results of this paper, EKF does not have the necessary accuracy in estimating the variables. This is due to the high dependence of the output on the values of noise and process covariance matrices, which can be mentioned as another drawback of this type of filter. A PSO-EKF is proposed to make an effective re-adhesion estimator. The PSO- EKF estimator's performance was evaluated by comparing the actual and estimated values of load torque, motor speed, rotor flux, and stator current. Then, according to the relationship between the torque and longitudinal creep force, the motor torque and adhesion force were calculated. It was observed that PSO-EKF estimated the states with low error values when the wheel-rail contact conditions varied. In this course, different creep curves corresponding to different contact conditions are utilized and the estimation results are found accurate and desirable. Beneficial implications of the proposed estimator include improvement in the performance of the re-adhesion controller, creepage reduction, and maximum traction achievement. Meanwhile, the proposed PSO-EKF estimator has superiority in estimation when the wheel-rail contact conditions change. Despite these advantages, one of the major problems of this type of estimator is that tuning the covariance matrices of process and measurement noise is time-consuming. An appropriate hybrid model such as GA-PSO-EKF may provide more flexible and fast convergence and less computational time than the individual models. This estimator shall be simulated and implemented in future works to improve the estimation accuracy and save time.

REFERENCES

[1] J. Zhou, M. Wu, C. Tian, et al., "Experimental investigation on wheel–rail adhesion characteristics under water and large sliding conditions." Industrial Lubrication and Tribology, Vol. 73, No. 2, pp. 366-372. 2021.

[2] H. Chen, T. Furuya, S. Fukagai, et al., "Wheel slip/Slide and low adhesion caused by fallen leaves." wear, Vol. 446–447, 203187, 2020.

[3] M. Harmon, R. Lewis "Review of top of rail friction modifier tribology. Tribology Materials, Surfaces & Interfaces." pp.150–162, 2016.

[4] Y. Lyu, E. Bergseth, U. Olofsson "Open system tribology and influence of weather condition. Scientific Reports." 6:32455, 2016.

[5] H. Chen, H. Tanimoto, "Experimental observation of temperature and surface roughness effects on wheel/rail adhesion in wet conditions." Int J Rail Transportation. 6:101–112, 2018.

[6] U. Olofsson, Y. Lyu, "Open system tribology in the wheel–rail contact—a literature review." Appl Mechanics Rev. 69:60803, 2017.

[7] M. Shen., Y. Qin, D. Ji, et al. "Role of ambient temperature in the adhesion and damage characteristics of wheel/rail interface during rolling-sliding contact." wear, Vol. 506–507, 204458. 2022.

[8] M. Spiryagin, C. Cole, YQ Sun, et al. "General modelling techniques. Design and simulation of rail vehicles." Boca Raton, Florida: CRC Press/Taylor and Francis. pp. 79–95, 2014.

[9] H. Chen, M. Ishida, A. Namura, et al. "Estimation of wheel/rail adhesion coefficient under wet condition with measured boundary friction coefficient and real contact area", Wear, Vol. 271, pp. 32–39, 2011.

[10] I. Hussain, T. Mei, and Ritchings, "R. Estimation of wheelrail contact conditions and adhesion using the multiple model approach", Vehicle System Dynamics, Vol. 51, pp. 32–53, 2013.

[11] S. Strano, and M. Terzo, "On the real-time estimation of the wheel-rail contact force by means of a new nonlinear estimator design model", Mechanical Systems and Signal Processing, Vol. 105, pp. 391–403, 2018.

[12] H. Schwartz and R. Kresse, "Implementation of an advanced wheel creep control with searching strategy on a light rail vehicle," European Conference on Power Electronics and Applications, Nagaoka, Japan, pp. 3.434–3.438, 1997.

[13] I. Yasuoka, T. Henmi,Y. Nakazawa, and I. Aoyama, "Improvement of re-adhesion for commuter trains with vector controltraction inverter," Proceedings of the Power Conversion Conference, pp. 51–56, 1997.

[14] T. Watanabe and A. Yamanaka, T. Hirose, K. Hosh, and S. Nakamura, "Optimisation of readhesion control of Shinkansen trains with wheel–rail adhesion, prediction, Proceedings of the Power Conversion Conferecne," Nagaoka, Japan, pp. 47–50, 1997.

[15] M. Spiryagin, P. Wolfs, Q. Wu, et al. “Rail Cleaning Process and its Influence on Locomotive Performance.” Joint Rail Conference (JRC2017). Philadelphia, PA: ASME. Apr 4, 2017.

[16] M. Spiryagin, C. Cole, YQ. Sun, “Adhesion estimation and its implementation for traction control of locomotives.” Int J Rail Transportation, pp.187–204, 2014.

[17] P. Pichlík, J. Zděnek, “Adhesion force detection method based on the kalman filter for slip control purpose,” Automatika – Journal for Control, Measurement, Electronics, Computing and Communications, Vol. 57, No. 2, pp. 405-415, 2016.

[18] Y. Zhao, B. Liang, “Re-adhesion control for a railway single wheelset test rig based on the behaviour of the traction motor,” Vehicle Syst Dyn, Vol. 51, No. 1, pp. 173–1185, 2013.

[19] A. Kawamura, , K. Takeuchi, T. Furuya, et al., “Measurement of Tractive Force and the New Maximum Tractive Force Control by the Newly Developed Tractive Force Measurement Equipment,” IEEJ Transactions on Industry Applications, Vol. 123, No. 8, pp. 885-893, 2003.

[20] Y. Matsumoto, N. Eguchi, A. Kawamura, “Novel Re-Adhesion Control for Train Traction System of The Shinkansen with The Estimation of Wheel-to-Rail Adhesive Force,” IECON'01, 27th Annual Conference of the IEEE Industrial Electronics Society (Cat. No.37243), 29 Nov.-2 Dec. Denver, CO, USA, Vol. 2, pp. 1207-1212, 2001.

[21] Y. Zhao, B. Liang, “Re-adhesion control for a railway single wheelset test rig based on the behaviour of the traction motor”, Vehicle System Dynamics, Vol 51, No. 8, pp. 1173-1185, 2013.

[22] S. Wang, J. Xiao, J. Huang, Sheng, H., “Locomotive Wheel Slip Detection Based on Multi-Rate State İdentification of Motor Load Torque”, Journal of the Franklin Institute, Vol. 353, No. 2, pp. 521-540, 2016.

[23] M. Barut, O. Bogosyan, M. Gokasan, “EKF Based Estimation for Direct Vector Control of Induction Motors”, IEEE 28th Annual Conference of the Industrial Electronics Society, Sevilla, Spain, pp.1710-1715. November 2002.

[24] L. Zhang, Y. Zhang, Z. Liu, et al, “Application of Genetic Algorithms in EKF for Speed Estimation of an Inducion Motor”, Proc. on IEEE Power Electronics Specialist Conference, Acapulco, Mexico, Vol. 1, pp. 345-349, 15-19, June 2003.

[25] C. Schwarz, A. Keck, “Observer Synthesis for the Adhesion Estimation of a Railway Running Gear”. ELSEVIER, Vol 52, Issue 15, pp. 319-324, 2019.

[26] M. Barut, S. Bogosyan, and M. Gokasan, “Speed-Sensorless Estimation for Induction Motors Using Extended Kalman Filters,” IEEE Transactions on Industrial Electronics, Vol. 54, No. 1, pp. 272–280, Feb. 2007.

[27] M. Barut, R. Demir, E. Zerdali, and R. Inan, “Real-Time Implementation of Bi Input-Extended Kalman Filter-Based Estimator for Speed-Sensorless Control of Induction Motors,” IEEE Transactions on Industrial Electronics, Vol. 59, No. 11, pp. 4197–4206, Nov. 2012.

[28] R. Inan and M. Barut, “Bi input-extended Kalman filter-based speed-sensorless control of an induction machine capable of working in the field-weakening region,” Turk J Elec Eng & Comp Sci, Vol. 22, No. 3,pp. 588–604, Apr. 2014.

[29] E. Zerdali and M. Barut, “Novel version of bi input-extended Kalman filter for speed-sensorless control of induction motors with estimations of rotor and stator resistances, load torque, and inertia,” Turk. J. Electr.Eng. Comput. Sci., Vol. 24, No. 5, pp. 4525–4544, 2016.

[30] S. H. Moosapour, M. Asadollahi, and S. S. Moosapour, “State Estimation in a Power System by Utilizing EKF and UKF.” 28th International Power System Conference, Tehran, 2014.

[31] K. L. Shi, T. Chan, Y. Wong, and S. Ho, “Speed estimation of an induction motor drive using an optimized extended Kalman filter,” IEEE Transactions on Industrial Electronics, Vol. 49, No. 1, pp. 124–133, Feb.2002.

[32] N. Salvatore, A. Caponio, F. Neri, S. Stasi, et al, “Optimization of Delayed-State Kalman-Filter-Based Algorithm via Differential Evolution for Sensorless Control of Induction Motors,” IEEE Transactions on Industrial Electronics, Vol. 57, No. 1, pp. 385–394, Jan. 2010.

[33] E. Zerdali and M. Barut, “The Comparisons of Optimized Extended Kalman Filters for Speed-Sensorless Control of Induction Motors,” IEEE Transactions on Industrial Electronics, Vol. 64, No. 6, pp. 4340–4351, Jun. 2017.

[34] A. Almagbile, J. Wang, and W. Ding, “Evaluating the Performances of Adaptive Kalman Filter Methods in GPS/INS Integration,” Journal of Global Positioning Systems, Vol. 9, No. 1, pp. 33–40, Jun. 2010. Using an Interfacing Multiple-Model Extended Kalman Filter,” IEEE Transactions on Power Electronics, Vol. 29, No. 6, pp. 3011–3019, Jun. 2014.

[35] K. Drozdz, “Estimation of the mechanical state variables of the two-mass system using fuzzy adaptive Kalman filter - Experimental study,” in 2015 IEEE 2nd International Conference on Cybernetics (CYBCONF), pp. 455–459, Jun. 2015.

[36] Z. Yin, G. Li, Y. Zhang, et al, “A Speed and Flux Observer of Induction Motor Based on Extended Kalman Filterand Markov Chain,” IEEE Transactions on Power Electronics, Vol. 32, No. 9, pp. 7096–7117, Sep. 2017.

[37] Z. Yin, L. Xiao, X. Sun, et al, “A speed and flux estimation method of induction motor using fuzzy extended kalman filter,” in Electronics and Application Conference and Exposition (PEAC), 2014 International, pp. 693–698, Nov. 2014.

[38] C. P. Ward, R. M. Goodall, R. Dixon, et al. “Adhesion estimation at the wheel–rail interface using advanced model-based filtering. Vehicle System Dynamics,” Vol. 50, pp.1797–1816, 2012.

[39] P. Hubbard, C. Ward, R. Goodall, et al. ‘Real time detection of low adhesion in the wheel/rail contact. Proceedings of the Institution of Mechanical Engineers,” Part F: Journal of Rail and Rapid Transit, Vol. 227, pp. 623–634, 2013

[40] S. Iwnicki, editor. Handbook of railway vehicle dynamics. Boca Raton, FL: CRC Press; 2006.

[41] M. Spiryagin, C. Cole, YQ. Sun, et al. “Design and simulation of rail vehicles, ground vehicle engineering series,” Boca Raton, FL: CRC Press; 2014.

[42] C. Weidemann, “State-of-the-art railway vehicle design with multibody simulation,” J Mech Systems Transport Logist, pp. 12–26; 2010.

[43] A. Steimel, “Electric traction–motive power and energy supply: basics and practical experience,” Munich: Oldenbourg Industrieverlag; 2008.

[44] R. Mathew, F. Flinders, and W. Oghanna, "Locomotive 'total systems' simulation using SIMULINK," Proceedings of international conference on electric railways in a United Europe; Amsterdam, pp. 202–206, 1995.
[45] O. Polach, "Creep forces in simulations of traction vehicles running on adhesion limit," Wear. 258:992–1000; 2005.
[46] EAH. Vollebregt, "Numerical modeling of measured railway creep versus creep-force curves with CONTACT," Wear. Vol. 314, pp. 87–95; 2014.
[47] M. Spiryagin, KS. Lee, HH. Yoo, et al, "Modeling of adhesion for railway vehicles." J Adhes Sci Technol. pp.1017–1034; 2008.
[48] M. Spiryagin, O. Polach, and C. Cole, "Creep force modelling for rail traction vehicles based on the Fastsim algorithm," Veh Syst Dyn.;51(11):1765–1783, 2013.
[49] JJ. Kalker, "A fast algorithm for the simplified theory of rolling contact," Veh Syst Dyn.Vol.1, pp.1–13; 1982.
[50] O. Polach, "Influence of locomotive tractive effort on the forces between wheel and rail," Veh Syst Dyn. pp.7–22; 2001.
[51] M. Spiryagin, S. Simson, C. Cole, et al. "Co-simulation of a mechatronic system using Gensys and Simulink," Veh Syst Dyn, Vol. 50, pp. 495–507, 2012.
[52] HP. Kotz, "A toolkit for simulating mechatronics in railway vehicles," Simpack User Meeting 2003, Germany, 2003. Available from: http://www.simpack.com/fileadmin / simpack/doc/usermeeting03/um03-siemens_kotz.pdf.
[53] M. Spiryagin, A. George, YQ. Sun, et al, "Investigation on the locomotive multibody modelling issues and results assessment based on the locomotive model acceptance procedure," J Rail Rapid Transit; Vol. 227, Issue 5, pp. 453–468, 2013.
[54] O. Polach, A. Böttcher, D. Vannucci, et al, "Validation of simulation models in the context of railway vehicle acceptance," J Rail Rapid Transit. October 28, 2014; published online before print.
[55] Y. Zhang, S. Wang, G. Ji, "A comprehensive survey on particle swarm optimization algorithm and its applications," Math. Probl. Eng. 2015.
[56] R. Eberhart, J. Kennedy, "A new optimizer using particle swarm theory," Micro Machine and Human Science, MHS 95., Proceedings of the Sixth International Symposium on, 1995, pp. 39–43, 1995.
[57] M. M. Rizi, S. Abazari, N, Mahdian, "Dynamic Stability Improvement of Power System with Simultaneous and Coordinated Control of DFIG and UPFC using LMI," Vol. 4, Issue 3, pp. 341-353, 2021. Available from: https://doi.org/10.22111/ieco.2021.37604.1340
[58] Q. Wu, C. Cole, T. McSweeney, "Applications of particle swarm optimization in the railway domain," Int. J. Rail Transp. Vol. 4, Issue 3, pp.167–190, 2016.
[59] A. Onat, P. Voltr, "Particle swarm optimization based parametrization of adhesion and creep force models for simulation and modelling of railway vehicle systems with traction," ELSEVIER, Vol. 99, 102026, 2020.
[60] A. Zirek, A. Onat, "A novel anti-slip control approach for railway vehicles with traction based on adhesion estimation with swarm intelligence," Springer, Vol. 28, Issue 4, pp. 346–364, 2020.
[61] M. Barut, S. Bogosyan, and M. Gokasan, "EKF Based Sensorless Direct Torque Control of IMs in The Low Speed Range", Proceedings of the IEEE International Symposium on Industrial Electronics, 2005, ISIE 2005, Dubrovnik, Croatia, pp. 20-23 June 2005.
[62] O. Polach, "A Fast Wheel-Rail Forces Calculation Computer," Veh. Syst. Dyn. Suppl, Vol. 33, pp. 728–739, 1999.
[63] J. Kalker, "On The Rolling Contact of Two Elastic Bodies in The Presence of Dry Friction," Wear, Vol. 11, Issue 4, pp. 303, 1968.
[64] KL. Shi, YK. Wong, and SL. Ho, "Speed estimation of an induction motor drive using an optimized extended Kalman filter.," IEEE Trans. On Industrial Electronics, Vol. 49, pp. 124-133, 2002.

APPENDIX A: The pseudo code for PSO-EKF

1. Initialize particles and the parameters of PSO Do

2. Reconstruct the matrices Q, R

3. Run EKF

3.1 Find Jacobian matrices $\mathbf{F_e(k)}$

$$F_e(k) = \frac{\partial f_e(x_e(k).u_e(k))}{\partial x_e(k)}\Big| (\hat{x}_e(k).\hat{u}_e(k))$$

3.2 Prediction of error covariance matrix

$$P^-(k+1) = F_e(k)P_k(k)(F_e(k))^T + F_u(k) D_u(k)(F_u(k))^T + Q(k)$$

3.3 Calculation of Kalman gain matrix

$$K(k) = P^-(k+1)H^T(HP^-(k+1)H^T + R(k))^{-1}$$

3.4 Update state and error covariance

$$\hat{x}_e(k+1) = \hat{f}_e\big(x_e(k).\hat{u}_e(k)\big) + K(k)(z(k) - H\hat{x}_e(k))$$

$$P(k+1) = (I - K(k)H)P^-(k+1)$$

4. Optimization Q and R by PSO

4.1 Evaluate fitness of particles

$$J = \frac{1}{N}\sum_{k=0}^{N}\|i_s(k) - \hat{i}_s(k)\|_2^2$$

4.2 Update particle velocity and position

$$v_i(k+1) = w.v_i(k) + c_1.r_1(k).(p_i(k) - x_i(k)) + c_2.r_2(k).(p_g(k) - x_i(k))$$

$$x_i(k+1) = x_i(k) + v_i(k+1)$$

Until Maximum iteration

Ramazan Havangi received his M.S. and Ph.D. degrees from the K.N. Toosi University of Technology, Tehran, Iran in 2003 and 2012, respectively. He is currently an Associate Professor of control systems with the Department of Electrical and Computer Engineering at the University of Birjand, Birjand, Iran. His main research interests are inertial navigation, integrated navigation, estimation and filtering, evolutionary filtering, simultaneous localization and mapping, fuzzy, neural network, and soft computing.

Maryam Moradi was born in Tehran, Iran. She received her B.S. degree in Control Engineering from Gonabad Azad University, Gonabad, Iran in 2008, and her M.S. degree in Telecommunications Engineering from the Faculty of Engineering at the University of Sistan

and Baluchestan, Zahedan, Iran in 2015. Since 2018, she has been a Ph.D. student in Control Engineering at the Faculty of Engineering, the University of Birjand, Birjand, Iran. In 2019, she joined the University of Applied Sciences & Technology as a teacher.

International Journal Of
Industrial Electronics Control and Optimization
Print ISSN: 3517-2645
Online ISSN: 3568-2645
Homepage: https://ieco.usb.ac.ir/

Comparative Analysis of Two Novel Passive Harmonic Suppression Circuits for Industrial Applications

Rohollah Abdollahi[1] | Alireza Reisi[2]

Department of Electrical Engineering, Technical and Vocational University (TVU), Tehran, Iran.[1,2]
Corresponding author's email: abdollahi@tvu.ac.ir

Article Info

Article type:
Research Article

Article history:
Received: 28 Oct 2022
Received in revised form :19 Feb 2023
Accepted: 19 Feb 2023
Published: 26 March 2023

Keywords:
12-pulse diode rectifier,
Passive harmonic suppression,
Tapped reactors,
Total harmonic distortion.

ABSTRACT

The 12-pulse diode rectifier (12-PDR) fails to comply with the limits of total harmonic distortion (THD) of supply current to be less than 5% specified in the IEEE Standard 519. Increasing the number of pulses further improves various power-quality indexes while imposing an additional cost of adding different converters and growing system complexity. Passive harmonic suppression circuits (PHSCs) have been observed to be a viable and cost-effective solution to improve the THD of AC-mains current at a reduced cost. PHSCs increase the number of rectification pulses without leading to significant changes in the installations and yield harmonic reduction in both AC and DC sides. This paper presents a comparative analysis of two novel PHSCs connected at the DC-bus of 12-PDR. One is PHSC-I based on four tapped reactors (FTRs) and four auxiliary diodes; the other is PHSC-II, with two tapped reactors (TTRs) and two auxiliary diodes. The operation modes and optimal parameters of both PHSCs are analyzed with similar inputs (AC side) and outputs (DC side). Both 12-PDR are connected to the same AC source as input, and both PHSCs supplied similar DC loads at their outputs, thus leading to an accurate and fair comparison between the two PHSCs. The results show that the input current THD of a 12-PDR with PHSC-II is lower than that of a PHSC-I and lower than existing passive harmonic suppression circuits. In addition, PHSC-II leads to lower connection losses, current stress, and cost than PHSC-I, so in industrial applications that require low input current THD, low connection losses/current stress, and low cost, PHSC-II is highly recommended.

I. Introduction

The application of rectification systems in the high-power industry is increasing, such as in DC-arc furnaces, plasma power supplies, graphite electrolysis plants, and electric aircraft [1]. Multi-pulse rectifiers (MPRs) have received more attention thanks to their straightforward configuration and high reliability and efficiency compared to DC generators. MPRs convert the alternative to direct voltage with a negligible ripple on a rectifier bridge and a phase-shifting transformer. Extensive research has been conducted to suppress input current harmonic distortion using MPR in industrial applications [1-2]. The current THD in the buck-boost PFC rectifier [3] and six-pulse rectifier [4] are 5.5% and 3.3%, respectively. The theory of 12-pulse rectification was developed long ago and played an irreplaceable role in multi-pulse basic research [5]. The first method is to adopt multi-phase transformers with multi-pulse diode bridges. Theoretically, this operation increases the number of MPRs and thus reduces the input current harmonic distortion [6-7]. Yet, the complex structure of multi-phase transformers and the high number of diodes employed are some of the disadvantages of this method [8-9]. The second method to reduce the input harmonic distortion is utilizing the multi-tapped interphase reactor (IPR) [10]. If the IPR existing in the

conventional 12-pulse rectifier is replaced with a two-tapped IPR and two auxiliary diodes, the performance of the rectifier will be upgraded to 24 pulses [11]. It should be noted that the current flow through these two auxiliary diodes is equal to the load current, increasing the diodes' conduction losses. The third method proposed recently is adding passive harmonic suppression circuits (PHSC) [12]. This method has two windings, the primary winding, including unconventional IPR (UIPR), is similar to the multi-tapped IPR and is connected to diode bridges, and the secondary winding is connected to a passive harmonic suppression circuit [13].

PHRCs are generally classified into two categories, single and dual PHRCs, as shown in Fig. 1. Basically, the main difference between various PHRCs is the configuration of the interphase transformer and the number of auxiliary diodes. In single PHRCs (tapped IPT [11], single-phase full-wave rectifier [12], single-phase diode-bridge rectifier [13]), auxiliary diodes are connected only to the secondary side of the interphase transformer. Auxiliary diodes are connected to both the primary and secondary sides of the interphase transformer in the following structures: double PHRCs (two single-phase full-wave rectifiers) [14], single-phase diode-bridge rectifiers and single-phase full-wave rectifiers [15], two-tapped IPT and single-phase full-wave rectifier [16], and two-tapped IPT and single-phase diode-bridge rectifier [17]. In [18], the classification of PHSC types is presented, and in [19], PHSC types are compared in terms of technical indicators, such as the ability to reduce input current harmonic distortion, efficiency, and economic indicators, such as weight, kVA rating, and cost.

This paper presents two novel harmonic suppression circuits (PHSC-I and PHSC-II) in 24-PDR and compares them in terms of technical and economic indicators. The PHSC-I consists of one FTR and four auxiliary diodes, and the PHSC-II includes two TTRs and two auxiliary diodes. Each of PHSC-I and PHSC-II can optimally operate in different applications in high-power rectification systems. The paper's primary purpose is to present two novel PHSCs and describe the performance and comparative analysis of these two circuits from technical and economic aspects. The performance of PHSC-I and PHSC-II in the DC-link of 12-PDR is described in Sections 2 and 3, respectively. Then the technical and economic comparison of PHSC-I and

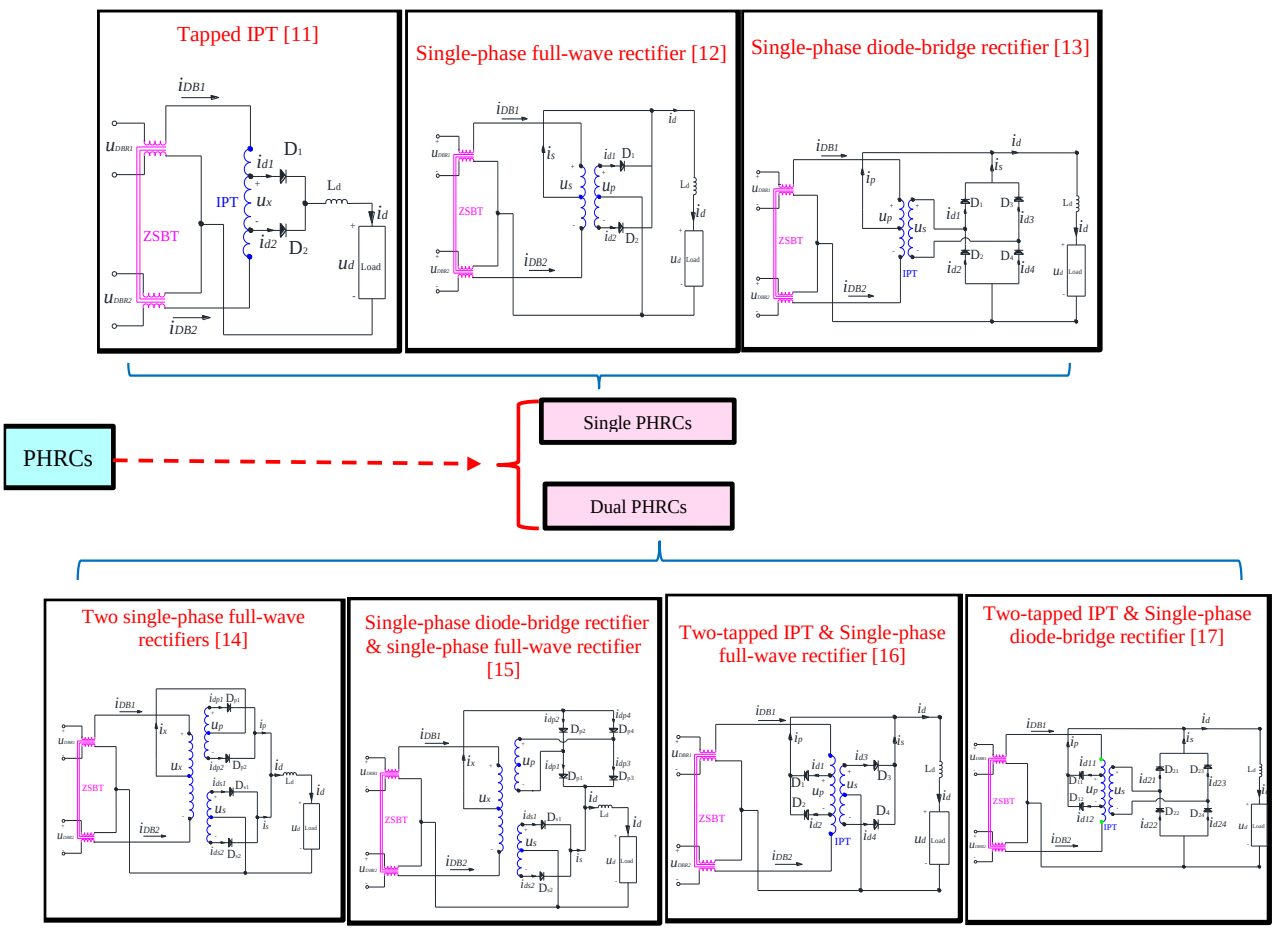

Fig. 1. Conventional PHSCs classification.

PHSC-II is presented in Section 4. Some conclusions are given in Section 5.

II. 12-PDR with PHSCs

As shown in Fig. 2, the 12-PDR with PHSCs consists of two main parts:

- A conventional 12-PDR
- Two novel PHSCs (PHSC-I or PHCS-II)

The 12-PDR comprises a tapped star-connected 6-phase autotransformer to produce two sets of 3-phase voltages (v_{a1} to v_{d1} and v_{a2} to v_{d2}) with a 30˚ phase shift. These two sets of the 3-phase voltage are converted to a 12-pulse waveform bypassed through two 6-pulse DBRs. To increase the 12-pulse waveform to the 24-pulse waveform, the PHSC is connected to the DC bus of these two 6-pulse DBRs. The 12-PDR with PHSC-I consists of two 6-pulse DBRs, and zero-sequence blocking transformer (ZSBT), an FTR, and two auxiliary diodes. But, the 12-PDR with PHSC-II consists of two 6-pulse DBRs, two TTRs, and two auxiliary diodes. ZSBT ensures the independent operation of DBRs, but 12-PDR with PHSC-II does not require ZSBT.

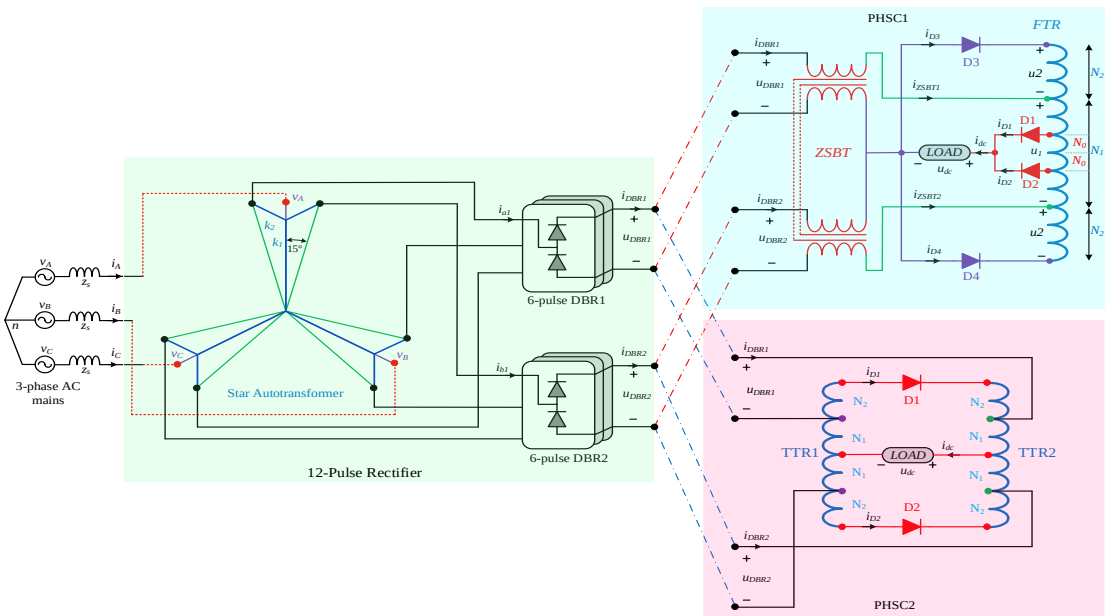

Fig. 2. 12-DBR with two novel PHSCs

A. Circuit Configuration and Working Principle of the PHSC-I

As indicated in Fig. 2, the 24-PDR comprises a conventional 12-PDR and PHSC-I. The PHSC-I is connected to the DC bus of the conventional 12-PDR, two 6-pulse DBRs, to generate a 24-pulse waveform. According to Fig. 3, the PHSC-I contains a ZSBT and a Four Tapped Reactor (FTR) with four auxiliary diodes. Output terminals of DBR1 and DBR2 are connected to ZSBT. Diodes D1 and D2 are connected to FTR1 with the N_1 turn on the winding. The diodes D3 and D4 are connected to the FTR2 with N_2 turn on the winding.

The following equations describe tap ratios m and k for this FTR:

$$k = \frac{N_0}{N_1} \quad (1)$$

$$m = \frac{N_2}{N_1} \quad (2)$$

The operation of the 24-PDR depends on the relation between the voltages across the windings (N_1 and N_2) of the FTR (u_1 and u_2) and output voltage (u_{dc}). According to the relation between u_{dc}, u_1, and u_2, the 24-PDR has four operation modes. Table 1 describes the operating principle of the PHSC-I indicated in Fig. 3 in four modes based on the relationship between load voltage u_{dc} and voltages u_1 and $(u_2 + (k+0.5)u_1)$. These four modes are described in Table 1 through KirchhOFF's Voltage Law (KCL) and KirchhOFF's Current Law (KCL) based on the status of diodes and DBRs. In this table, the ON and OFF status of diodes means forward bias (conducting) and reverse bias (not conducting); ON for DBRs means being active, and OFF means being in the reverse bias.

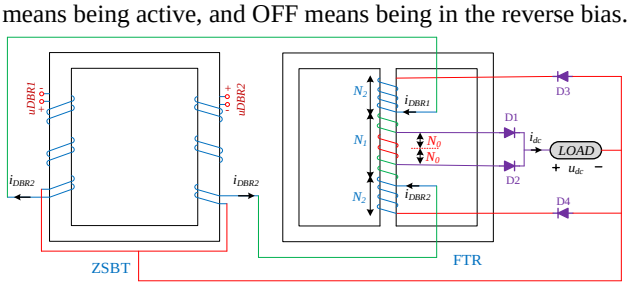

Fig. 3. Structure of the PHSC-I

In mode 1, D3 and D4 are OFF, so both u_2 are zero. The load is supplied by DBR1 (iDBR1) and DBR2 (iDBR2) output currents through D1. By applying KCL

$$i_{dc} = i_{DBR1} + i_{DBR2} \quad (3)$$

The FTR equation for MMF is expressed as

$$i_{DBR1}(0.5N_1 - kN_1) = i_{DBR2}(0.5N_1 + kN_1) \quad (4)$$

Using (3) and (4), the currents i_{DBR1} and i_{DBR2} are determined by the following equations:

$$\begin{cases} i_{DBR1} = (0.5 + k)i_{dc} \\ i_{DBR2} = (0.5 - k)i_{dc} \end{cases} \quad (5)$$

And also, applying KVL gives:

$$u_{dc} = u_{DBR1} - (0.5 - k)u_1 \quad (6)$$

$$u_{dc} = u_{DBR2} + (0.5 + k)u_1 \quad (7)$$

$$u_1 = u_{DBR2} - u_{DBR1} \quad (8)$$

In mode 2, the DBR2 is OFF since u_2 is higher than (v_{a2} to v_{d2}), so DBR1 supplies the load through D1. In this mode, D4 adds N_2 to N_1 to keep voltage and current in the fixed range. Here, applying KCL gives:

$$i_{dc} = i_{DBR1} + i_{D4} \quad (9)$$

The MMF equation of the FTR is presented as follows:

$$i_{DBR1}(0.5N_1 - kN_1) = i_{D4}(N_2 + 0.5N_1 + kN_1) \quad (10)$$

Using (8) and (9), the currents i_{DBR1} and i_{D4} are written as below:

$$i_{DBR1} = \frac{k+m+0.5}{m+1} i_{dc} \quad (11)$$

$$i_{D4} = \frac{0.5-k}{m+1} i_{dc} \quad (12)$$

The relations among u_{DBR1}, u_{DBR2}, u_{dc}, and u_1 are summarized as follows:

$$u_{dc} = \frac{k+m+0.5}{m+1} u_{DBR1} \quad (13)$$

$$u_{DBR2} = \frac{m}{m+1} u_{DBR1} \quad (14)$$

$$u_{FTR1} = \frac{1}{m+1} u_{DBR1} \quad (15)$$

In mode 3, similar to mode 1, D3 and D4 are OFF, so both u_2 are zero, and the load is supplied by DBR1 (i_{DBR1}) and DBR2 (i_{DBR2}) output currents through D2. Applying KCL gives:

$$i_{dc} = i_{DBR1} + i_{DBR2} \quad (16)$$

The MMF equation in N_1 is written as follows:

$$i_{DBR1}(0.5N_1 + kN_1) = i_{DBR21}(0.5N_1 - kN_1) \quad (17)$$

Using (15) and (16), i_{DBR1} and i_{DBR2} can be written as

$$i_{DBR1} = (0.5 - k)i_{dc} \quad (18)$$

$$i_{DBR2} = (0.5 + k)i_{dc} \quad (19)$$

The following relationship is established between u_{DBR1}, u_{DBR2}, u_{dc}, and u_1:

$$u_{dc} = u_{DBR1} - (0.5 + k)u_1 \quad (20)$$

$$u_{dc} = u_{DBR2} + (0.5 - k)u_1 \quad (21)$$

$$u_1 = u_{DBR1} - u_{DBR2} \quad (22)$$

In mode 4, the DBR1 is OFF because -u_2 is higher than (v_{a1} to v_{d1}), so just DBR2 supplies the load through D2. In this mode, D3 adds N_2 to N_1 to keep voltage and current in the fixed range. Here, applying KCL gives:

$$i_{dc} = i_{DBR2} + i_{D3} \quad (23)$$

The following equation expresses the MMF equation of the FTR:

$$i_{DBR2}(0.5N_1 - kN_1) = i_{D3}(N_2 + 0.5N_1 + kN_1) \quad (24)$$

Using (23) and (24), the currents i_{DBR2} and i_{D3} are determined as below:

$$i_{DBR2} = \frac{k+m+0.5}{m+1} i_{dc} \quad (25)$$

TABLE 1
WORKIND MODEs OF THE PHSC-I

#	KVL	KCL	Diode1	Diode2	Diode3	Diode4	DBR1	DBR2
1	$u_1>0$ & $u_2+(k+0.5)\,u_1<u_{dc}$	$i_{DBR1} + i_{DBR2} = i_{dc}$	ON, $i_{D1} > 0$	OFF, $i_{D2} = 0$	OFF, $i_{D3} = 0$	OFF, $i_{D4}= 0$	ON, $i_{D1}>0$	ON, $i_{D1} > 0$
2	$u_1>0$ & $u_2+(k+0.5)\,u_1>u_{dc}$	$i_{DBR1} + i_{D4} = i_{dc}$	ON, $i_{D1} > 0$	OFF, $i_{D2} > 0$	OFF, $i_{D3} = 0$	ON, $i_{D4} > 0$	ON,$i_{D1} > 0$	OFF, $i_{D1} = 0$
3	$u_1<0$ & $-u_2-(k+0.5)\,u_1<u_{dc}$	$i_{DBR1} + i_{DBR2} = i_{dc}$	OFF, $i_{D1} < 0$	ON, $i_{D2} < 0$	OFF, $i_{D3} = 0$	OFF, $i_{D4}= 0$	ON,$i_{D1} > 0$	ON, $i_{D1} > 0$
4	$u_1<0$ & $-u_2-(k+0.5)\,u_1>u_{dc}$	$i_{D3} + i_{DBR2} = i_{dc}$	OFF, $i_{D1} < 0$	ON, $i_{D2} < 0$	ON, $i_{D3} < 0$	OFF, $i_{D4}= 0$	OFF,$i_{D1} = 0$	ON, $i_{D1} > 0$

$$i_{D3} = \frac{0.5-k}{m+1} i_{dc} \quad (26)$$

The relations among u_{DBR1}, u_{DBR2}, u_{dc}, and u_1 are determined as follows:

$$u_{dc} = \frac{k+m+0.5}{m+1} u_{DBR2} \quad (27)$$

$$u_{DBR2} = \frac{m}{m+1} u_{DBR2} \quad (28)$$

$$u_{FTR1} = -\frac{1}{m+1} u_{DBR2} \quad (29)$$

The optimal tap ratios of the FTR (i.e., m and k) are obtained subject to minimizing the input current %THD. Therefore, the critical point of designing the PHSC-I is determining the optimal FTR turns ratio, significantly decreasing the input current %THD. These values could be determined based on the try-and-error method using MATLAB simulation, which is set (k=0.25 and m=6.5), resulting in an input current THD of 1.72%. The designed PHSC-I has been evaluated using MATLAB simulation in situations where the load voltage is 380V (50Hz) and the full load power is 10kW. Fig. 4 and Fig. 5 indicate the simulation

results, the waveform of the primary voltage, and the current of the 12-PDR with PHSC-I, respectively. The 12-PDR with PHSC-I output voltage waveform is shown in Fig. 4(a), and the FTR1 and FTR2 voltage waveforms are shown in Fig. 4(b) and Fig. 4(c), respectively. As mentioned before, the relationship between these voltages determines the operating modes of the PHSC-I. The ZSBT voltage waveform is also shown in Fig. 4(d).

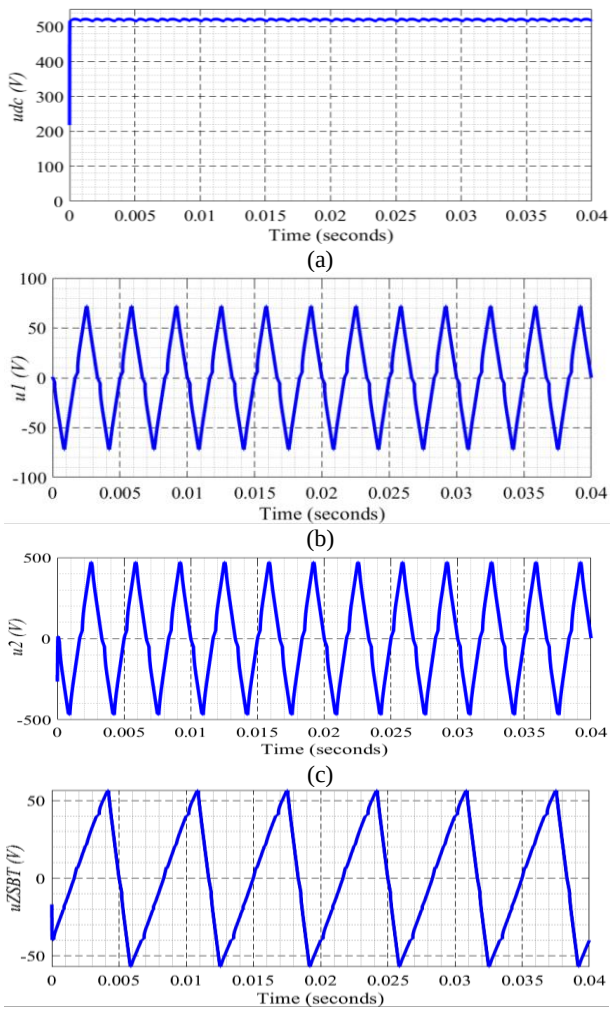

Fig. 4. Main voltage waveforms of the 12-PDR with PHSC-I. (a) u_{dc}, (b) u_1, (c) u_2, (d) u_{ZSBT}

The 12-PDR with PHSC-I output current waveform is shown in Fig. 5(a). The currents flowing through the auxiliary diodes (i_{D1} and i_{D2}) are shown in Fig. 5(b), and the currents flowing through the auxiliary diodes (i_{D3} and i_{D4}) are shown in Fig. 5(c). As can be seen, a significant part of the load current passes through the D1 and D1, and the current passing through the auxiliary diodes D3 and D4 are minimal compared to the load current, which leads to a reduction in conduction losses and the current stress of the auxiliary diodes D3 and D4.

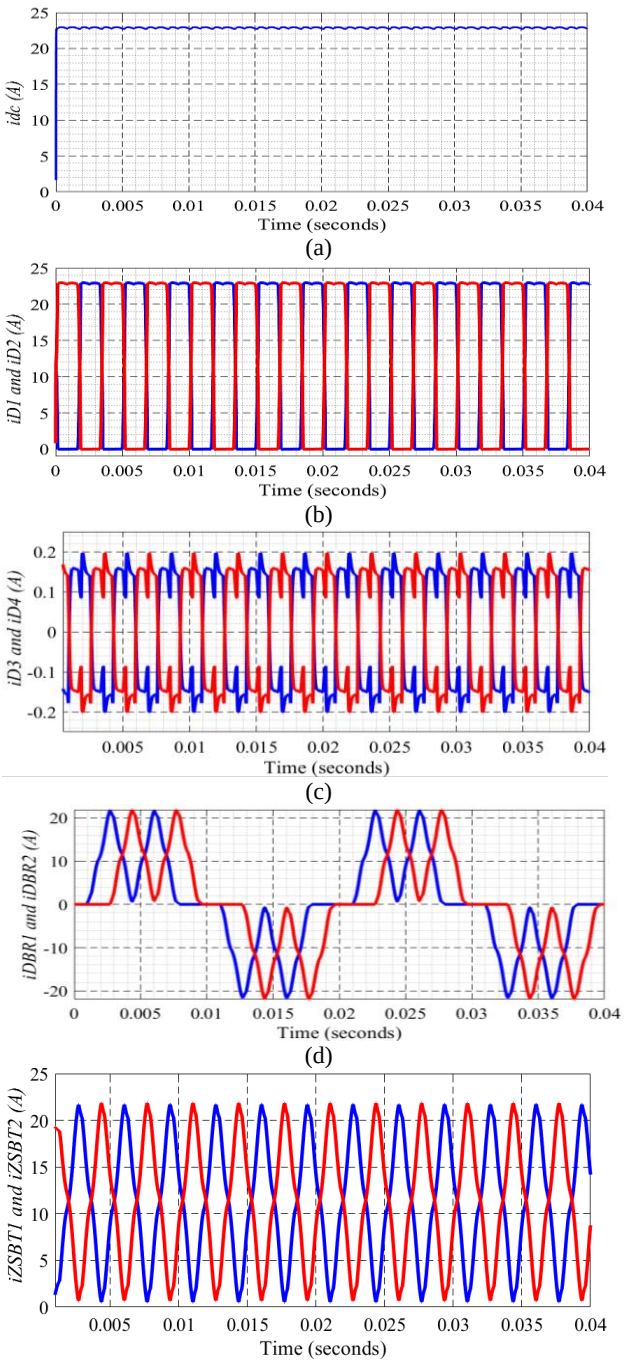

Fig. 5. Main current waveforms of the 12-PDR with PHSC-I. (a) i_{dc}, (b) i_{D1} and i_{D2}, (c) i_{D3} and i_{D4}, (d) i_{DBR1} and i_{DBR2}, (e) i_{ZSBT}

The input currents of these two 6-pulse DBRs are shown in Fig. 5(d), and the ZSBT current of the 12-PDR with PHSC-I is demonstrated in Fig. 5(e). These figures confirm the high performance of the 12-PDR with PHSC-I in reducing the harmonic distortions of the input current, thus providing a fully sinusoidal current.

B. Circuit Configuration and Working Principle of the PHSC- II

According to Fig. 6, The PHSC-II consists of two TTRs and two auxiliary diodes. Each TTR is hooked up in the positive and negative polarity of 6-pulse DBRs. Then, the two TTRs are connected through two auxiliary diodes. Finally, the two TTRs are connected to the load. Table 2 describes the working principle of the PHSC-II, indicated in Fig. 6, in three modes based on the relationship between load voltage u_{dc} and voltage (u_{TTR1}+u_{TTR2}). These three modes could be described based on the status of diodes and DBRs through KCL and KVL.

In mode 1, D_1 and D_2 are OFF, and the 24-PDR behaves as a conventional 12-PDR. From the KCL and Magnetic Motive Force (MMF) balance of the windings in the two TTRs, the relationship among the output current of DBR1, the output current of DBR2, and the load current are given as follows:

$$i_{DBR1} = i_{DBR2} = \frac{1}{2} i_{dc} \quad (30)$$

In mode 2, D_2 and DBR1 are ON. Meanwhile, the DBR2 is turned OFF.

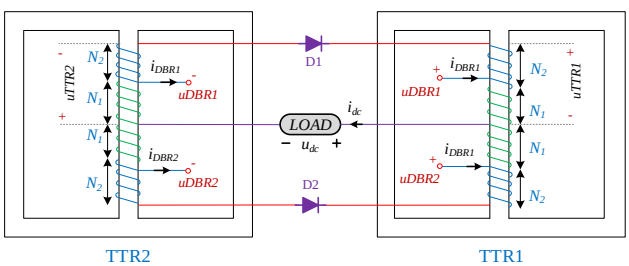

Fig. 6. Structure of the PHSC-II

$$\begin{cases} i_{DBR1} = \frac{2m}{2m+1} i_d \\ i_{D2} = \frac{1}{2m+1} i_d \end{cases} \quad (31)$$

In mode 3, the diodes that were ON in mode 2 now turn OFF, and vice versa. In terms of KCL and the MMF of the two TTRs, the currents i_{DBR2} and i_{D1} are given as follows:

$$\begin{cases} i_{DBR2} = \frac{2m}{2m+1} i_d \\ i_{D1} = \frac{1}{2m+1} i_d \end{cases} \quad (32)$$

where m is the turns ratio of the TTR and equals to $(N_1+N_2)/2N_1$ (as shown in Fig. 6). The optimal turns ratio of the TIPR (i.e., m) is determined using the try and error method subject to minimize %THD of the input current. The TTR turns ratio of 7.90 results in an input current THD of 0.67%.

Figs. 7 and 8 show the primary voltage and current of the 12-PDR with the PHSC-II. The rectifier output voltage waveform is shown in Fig. 7(a), and the TTR voltage waveform is shown in Fig. 7(b). As mentioned before, the relationship between these voltages determines the operating modes of the PHSC-II. The 6-pulse DBRs output voltage is shown in Fig. 7(c). According to this figure, by using PHSC-II in 12-PDR, the operational independence of these two DBRs is confirmed without needing ZSBT. Fig. 7(d) shows the output waveform of a 6-phase autotransformer, which consists of two series of 3-phase voltages with 30-degree displacement. These two series of 3-phase voltages supply two 6-pulse diode bridges (DBR1 and DBR2) to achieve a 12-PAR. The rectifier output current waveform is shown in Fig. 8(a). The currents flowing through the auxiliary diodes (i_{D1} and i_{D2}) are shown in Fig. 8(b), and the current flowing through the DBRs (i_{DBR1} and i_{DBR2}) is shown in Fig. 8(c). Based on Fig. 8(b), a significant part of the load current passes through the TTR, and the current passing through the auxiliary diodes (i_{D1} and i_{D2}) is minimal compared to the load current, which leads to a reduction in conduction losses and the current stress of the auxiliary diodes.

TABLE 2
WORKIND MODEs OF THE PHSC-II

#	KVL	KCL	Diode 1	Diode 2	DBR 1	DBR 2
1	$\lvert u_{TTR1} + u_{TTR2} \rvert < u_{dc}$	$i_{DBR1} + i_{DBR2} = i_{dc}$	OFF, $i_{D1} = 0$	OFF, $i_{D2} = 0$	On, $i_{DBR1} > 0$	On, $i_{DBR2} > 0$
2	$u_{TTR1} + u_{TTR2} > u_{dc}$	$i_{DBR1} + i_{D2} = i_{dc}$	OFF, $i_{D1} = 0$	On, $i_{D2} > 0$	On, $i_{DBR1} > 0$	OFF, $i_{DBR2} = 0$
3	$-(u_{TTR1} + u_{TTR2}) > u_{dc}$	$i_{D1} + i_{DBR2} = i_{dc}$	On, $i_{D1} > 0$	OFF, $i_{D2} = 0$	OFF, $i_{DBR1} = 0$	On, $i_{DBR2} > 0$

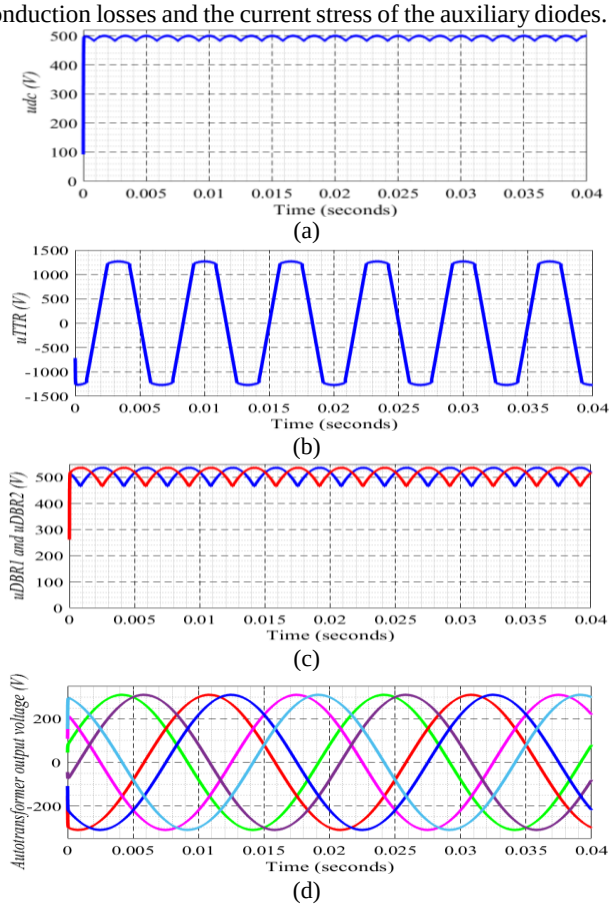

Fig. 7. Main voltage waveforms of the 12-PDR with the PHSC-II. (a) u_{dc}, (b) u_{TTR}, (c) u_{DBR1} and u_{DBR2}, (d) autotransformer voltage

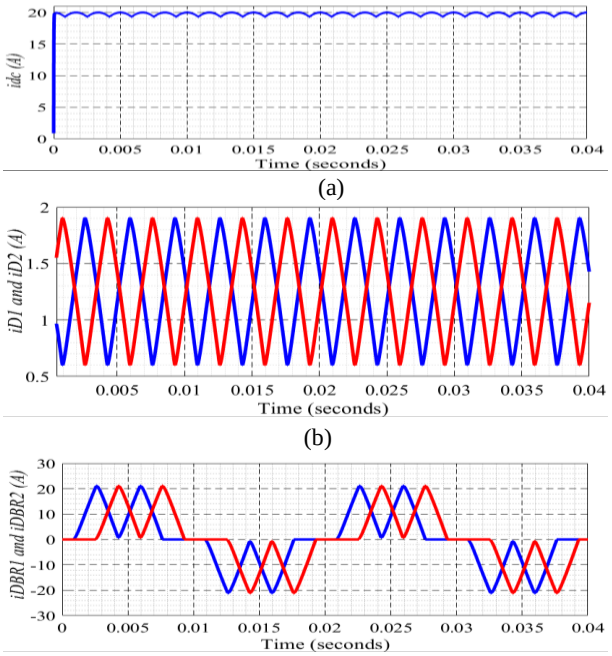

Fig. 8. Main current waveforms of the 12-PDR with the PHSC-II. (a) i_{dc}, (b) i_{D1} and i_{D2}, (c) iDBR1 and i_{DBR2}

III. Comparison of PHSC-I with PHSC-II

Ref. [20] presents an electrical and magnetic comparison between two structures of 10-phase autotransformers. With this approach to clarifying the main characteristics of the two novel PHSCs, a technical and economic comparison is performed between the PHSC-I and the PHSC-II. Comparison of technical indicators includes calculating %THD input current of 12-PDR with PHSCs under different load conditions, according to standard requirements IEEE-519. Fig. 9 shows the input current/voltage and their harmonic spectrums of the 12-PDR with (a) PHSC-I and (b) PHSC-II. The input current THD is calculated under 380V line-to-line voltage and 50Hz frequency, and a source reactance of 3mH and considering a load resistance of 10kW. After using the PHSC-I in the 12-PDR, the simulated THD of the current and voltage are about 1.72% and 0.57%, respectively.

Also, using the PHSC-II in the 12-PDR, the simulated THD of the current and voltage are about 0.67% and 0.31%, respectively. Therefore, the harmonic reduction ability of the PHSC- II is significant. Although the input current THD in both 12-PDR structures with PHSC-I and PHSC-II is less than 5%, considering the harmonic components according to Fig. 10, the harmonic components are slightly more than the requirements of IEEE-519 in 12-PDR with PHSC-I in the range of 23-35 and 35-50 [21]. Instead, 12-PDR with PHSC-II fully complies with the requirements of the IEEE-519 standard for both input current THD and amplitude of harmonic components.

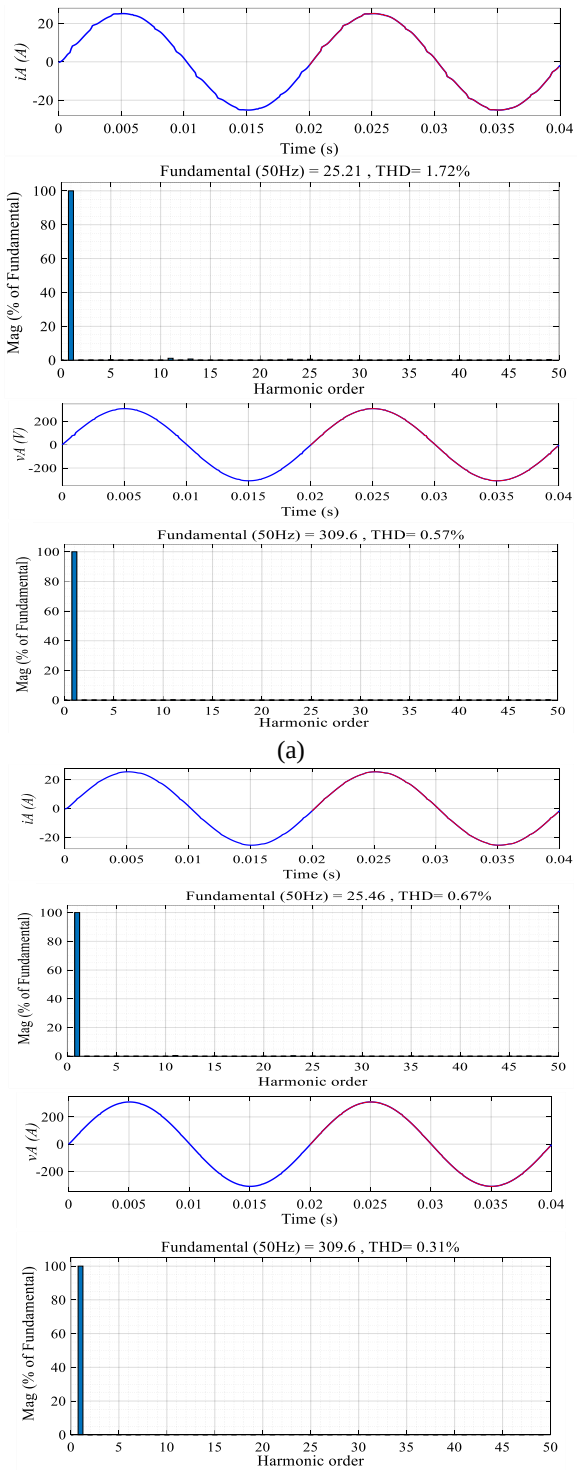

Fig. 9. Input current/ voltage waveform and their harmonic spectrums of the 12-PDR with (a) PHSC-I and (b) PHSC-II

TABLE 3
THE VOLTAGE/CURRENT OF WINDINGS AND RATING OF TWO NOVEL PHSCs UNDER 10 KVA

Topologies	C	RMS values	W_1	W_2	W_3	W_4	W_5	VA rating	Total VA rating
PHSC-I	ZSBT	V_{rms} (V)	34.44	34.44	34.44	34.44		442.55	697.58
		I_{rms} (A)	12.85	12.85	12.85	12.85			
	FTR	V_{rms} (V)	291.2	11.18	21.94	11.18	291.2	255.03	
		I_{rms} (A)	0.17	12.85	5.64	12.85	0.17		
PHSC-II	TTR1	V_{rms} (V)	540.7	34.96	34.96	540.7		563.46	1126.92
		I_{rms} (A)	1.34	11.51	11.51	1.34			
	TTR2	V_{rms} (V)	540.7	34.96	34.96	540.7		563.46	
		I_{rms} (A)	1.34	11.51	11.51	1.34			

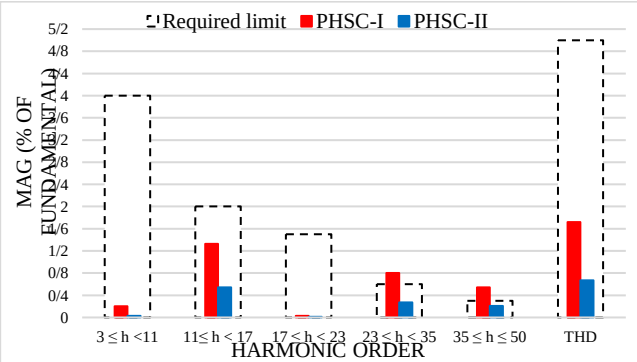

Fig. 10. Harmonic current limits of the 12-PDR with PHSC-I and PHSC-II in % of fundamental.

It should be noted that the passive harmonic suppression circuit similar to the structure of PHSC1 is presented in an 18-pulse rectifier [22], but it should be noted that firstly, in this 18-pulse rectifier, the optimal turns ratio is k=0.15 and m=1.87. Secondly, for this optimum turns ratio, the minimum of the input current THD is 5.44%, while in the proposed 24-pulse rectifier, for the optimal turn ratio PHSC1, k=0.25 and m=6.5 and the minimum of The input current THD is 1.72%. Also, a 40-pulse rectifier based on a passive harmonic suppression circuit similar to the structure of PHSC2 is proposed with an optimal turns ratio of m=14.17 [23], while the optimal value of the winding turns ratio of PHSC2 in the proposed 24-pulse rectifier is m=7.90. In other words, in this paper, the turns ratio of PHSC1 and PHSC2 is optimized according to the 24-pulse rectifier.

For the economic evaluation, first, the kVA rating of improved PHSCs is calculated, and then the cost is estimated according to the approach outlined in [24], where the cost of the transformer is estimated to be 4.5 times the kVA rating, and a diode price is considered as 2.25$. The kVA rating of the components of the PHSCs is calculated based on the following equation [25]:

$$S = 0.5 \sum V_{winding} I_{winding} \quad (33)$$

where $V_{winding}$ and $I_{winding}$ are the rms voltage and current of the windings of the PHSC components obtained from simulations under a 10 kVA load. As can be seen in Table 3, it can be seen that the kVA ratings of the PHSC-I and PHSC-II are 697.58 VA and 1126.92 VA, respectively. Therefore, the rating of PHSC-I and PHSC-II is 6.97% and 11.27% of the load power, respectively. It should be noted that the kVA rating of PHSC-I is 40% lower than the rank of PHSC-II.

Considering the diode's voltage drop of 0.7 V and the internal resistance of the diode of 1 mΩ, the connection losses of the diodes are determined as follows.

$$P_{Diode} = \frac{1}{\pi}\int_0^{\pi}(V_f i_d + i_d^2 R_d)d\theta = V_f I_d + I_d^2 R_d \quad (34)$$

Considering the current of the diodes in PHSC-I (I_{D1} = I_{D2} =15.7 A and I_{D3} = I_{D4} = 0.17 A) and PHSC-II (I_{D1} = I_{D2} =1.34 A), the connection losses are 22.71 W and 1.87 W, respectively. Also, due to the low current passing through the diodes of PHSC-II, it can be concluded that the current stress of circuit PHSC-II is much less than that of PHSC-I. Therefore, the connection losses and current stress of PHSC-II are much less than those of PHSC-I.

The iron and winding losses of the transformer are calculated as follows:

$$P_{core} = m_c k_c B_m^{\alpha} f_T^{\beta} \quad (35)$$

The copper losses can be determined by:

$$P_{copper} = \sum J \rho_{cu} (MLT_i) K_i N_i I_i \quad (36)$$

where, the mean length per turn (MLT_i), the number of turns (N_i), and the RMS current of the i^{th} winding (I_i) have been given in [26]. The total losses of the PHSCs have been calculated based on simulations using equations (34)-(36) and the parameters listed in Table 4. Therefore, the total losses in PHSC-I and PHSC-II are 104.36 W and 153.49 W, respectively.

To present the advantages of each of the PHSCs, Table 5 presents a technical and economic comparative analysis of the two novel PHSCs. According to this table, the THD of the input current of a 12-PDR with PHSC-II is less than PHSC-I.

TABLE 4
PARAMETERs USED IN THE CALCULATION OF LOSSEs [26]

Parameter	Symbol	Value
Material Coefficient	k_c	6.754×10^{-4}
AC/DC Resistance Factor	K_i	1.05
Maximum Flux Density	B_m	1.2 T
Current Density	J	2.3 A/mm^2
Electrical Resistivity of Cu	ρ_{cu}	2.3×10^{-8} Ωm
Exponent of Frequency	β	1.651
Exponent of Flux Density	α	1.559

Also, the connection losses and current stress of PHSC-II are less than those of PHSC-I. The total losses of PHSC-I are less than those of OHSC-II, and, as a result, its efficiency is higher. The kVA rating of PHSC-I is smaller, so its weight and size are lower. The PHSC-I consists of 4 diodes, and the PHSC-II consists of two diodes. Considering the kVA rating and the number of diodes, the cost of PHSC-II is less than that of PHSC-I, which is more economical. With these specifications, the PHSC-I is recommended for applications where weight, size, and efficiency are required. Also, in industrial applications with low input current THD, low connection loss, low current stress, and low cost, PHSC-II is recommended.

TABLE 5
COMPARISON OF TWO NOVEL PHSCs FOR 10 KW LOAD

Topologies	%THD of input current	Core Losses [W]	Copper Losses [W]	Connection Losses [W]	Total Power Losses [W]	kVA-Rating [VA]	Number of	Approximate Cost
PHSC-I	1.72	18.33	63.32	22.71	104.36	697.58	4	12.14
PHSC-II	0.67	26.64	125.18	1.87	153.69	1126.92	2	9.57

A comparison of the input current THD of a 12-pulse rectifier using existing PHSCs compared to PHSC-I and PHSC-II is shown in Fig. 11. As can be seen in this figure, the THD of the input current of 12 pulses with PHSC-II is much lower compared to other different PHSCs, which shows the high ability of PHSC-II in suppressing the harmonic distortion of the input current.

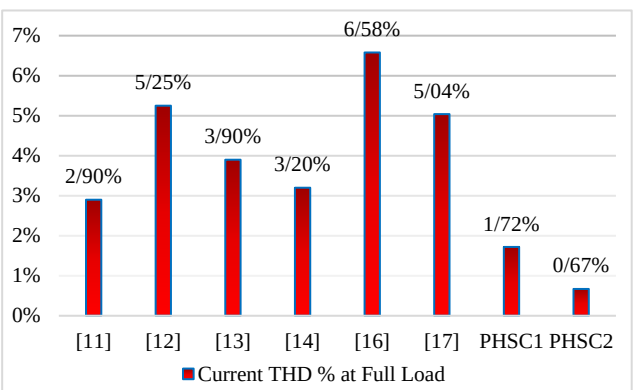

Fig. 11. Comparison of input current THD of 12-pulse rectifier with different PHSCs

IV. Conclusion

In the last few years, utilizing the PHSC in the DC-link of the multi-pulse rectifier has been considered an efficient solution to reducing the harmonic distortion of the input current. With this approach, two novel PHSCs are presented in this paper, and their performance is described, then are technically and economically compared under the same input source and output load conditions. The results demonstrate that the input current THD of a 12-PDR with PHSC-II is lower than that of PHSC-I and lower than existing passive harmonic suppression circuits, which verifies the high performance of PHSC-II to suppress the harmonic distortion of the input current. Furthermore, PHSC-II has lower connection losses, current stress, and cost than PHSC-I, so PHSC-II is recommended in industrial applications that require low input current THD, low connection losses/current stress, and low cost.

References

[1] B. Singh, S. Gairola and B. N. Singh, A. Chandra, and K. Al-Haddad, "Multipulse ac-dc converters for improving power quality: A review," IEEE Trans. on Power Electron., vol. 23, no. 1, pp. 260–281, Jan. 2008.

[2] D. A. Paice, Power Electronic Converter Harmonic Multipulse Methods for Clean Power. New York: IEEE Press, 1996.

[3] M. Monfard, M. Babaei, S. Sharifi, "A Z-Source Network Integrated Buck-Boost PFC Rectifier," International Journal of Industrial Electronics, Control and Optimization (IECO), vol. 2, no. 4, pp. 289-296, October 2019.

[4] H. Radmanesh, M. Saeidi, "Linear Modelling of Six Pulse Rectifier and Designee of Model Predictive Controller with Stability Analysis," International Journal of Industrial Electronics, Control and Optimization (IECO), vol. 3, no. 4, pp. 491-501, September 2020.

[5] R. Abdollahi, G. B Gharehpetian, A. Anvari-Moghaddam, and F. Blaabjerg, "An improved 24-pulse rectifier for harmonic mitigation in more electric aircraft," IET Power Electronics, vol. 14, no. 11, pp. 2007–2020, 2021.

[6] R. Abdollahi and G. B. Gharehpetian, "A 20-pulse autotransformer rectifier unit for more electric aircrafts," IEEE J. Emerg. Sel. Topics Power Electron., vol. 9, no. 3, pp. 2992–2999, Jun. 2021.

[7] P. S. Prakash, R. Kalpana, and B. Singh, "Inclusive Design and Development of Front-End Multi-Phase Rectifier with Reduced Magnetic Rating and Improved Efficiency," IEEE Trans. Emerg. Sel. Topics Power Electron., vol. 8, no. 3, pp. 2989–3000, Sept. 2020.

[8] R. Abdollahi and G. B. Gharehpetian, "Inclusive Design and Implementation of Novel 40-Pulse AC-DC converter for retrofit application and harmonic mitigation," IEEE Trans. Ind. Electron., vol. 63, no. 2, pp. 667-677, Feb. 2016.

[9] J. Chen, H. Bai, J. Chen, and Ch.Gong, "A Novel Parallel Configured 48-Pulse Autotransformer Rectifier for Aviation Application," IEEE Trans. Transp. Electrif., vol. 37, no. 2, pp. 2125-2138, Feb.

2022.
[10] R. Abdollahi, G. B. Gharehpetian, and M. S. Mahdavi, "Cost - effective multi - pulse AC - DC converter with lower than 3% current THD," International Journal of Circuit Theory and Applications, vol. 47, no. 7, pp. 1105-1120, 2019.
[11] B. Singh, G. Bhuvaneswari, V. Garg, and S. Gairola, "Pulse multiplication in ac–dc converters for harmonic mitigation in vector controlled induction motor drives," IEEE Trans. Energy Conv., vol. 21, no. 2, pp.342–352, Jun. 2006.
[12] Sh. Yang, J. Wang, and W. Yang, "A novel 24-pulse diode rectifier with an auxiliary single-phase full-wave rectifier at DC side," IEEE Trans. Power Electron., vol. 32, no. 3, pp. 1885–1893, Mar. 2017.
[13] F. Meng, X. Xu, and L. Gao, "A simple harmonic reduction method in multi-pulse rectifier using passive devices," IEEE Trans. Ind. Informat., vol. 13, no. 5, pp. 2680–2692, Oct. 2017.
[14] J. Wang, X. Yao, X. Gao, and Sh. Yang, "Harmonic reduction for 12-pulse rectifier using two auxiliary single-phase full-wave rectifiers," IEEE Trans. Power Electron., vol. 35, no. 12, pp. 12617–12622, Dec. 2020.
[15] J. Wang, X. Yao, J. Bai, Q. Guan, Sh. Yang, "A Simple 36-Pulse Diode Rectifier with Hybrid Pulse Multiplication Inter-phase Reactor at DC side," IEEE Trans. Emerg. Sel. Topics Power Electron., vol. 9, no. 3, pp. 3540–3555, June 2021.
[16] F. Meng, X. Xu, L. Gao, et al., "Dual passive harmonic reduction at DC link of the double-star uncontrolled rectifier," IEEE Trans. Ind. Electron., vol. 66, no. 4, pp. 3303–3309, Apr. 2019.
[17] L. Gao, X. Xu, Z. Man and J. Lee, "A 36-pulse diode-bridge rectifier using dual passive harmonic reduction methods at DC link," IEEE Trans. Power Electron., vol. 34, no. 2, pp. 1216–1226, Feb. 2019.
[18] Q. Du, L. Gao, Q. Li, T. Li, and F. Meng, "Harmonic Reduction Methods at DC Side of Parallel-connected Multi-pulse Rectifiers: A Review," IEEE Trans. Power Electron., vol. 36, no. 3, pp. 2768–2782, March 2021.
[19] R. Abdollahi, and G. B Gharehpetian, "Suggestion of DC side passive harmonic reduction circuits for industrial applications based on a comparative study," IET Power Electronics, vol. 15, no. 6, pp. 531–547, 2022.
[20] R Abdollahi, M Golchob, "Electric and magnetic comparison of two 10-phase autotransformers,"Ain Shams Engineering Journal, vol. 13, no. 4, 101662, 2022.
[21] IEEE Standard 519-1992, IEEE Recommended Practices and Requirements for Harmonic Control in Electrical Power Systems. New York: IEEE Inc., 1992.
[22] M. Abdul Malek, and Muhammad Abdul Goffar Khan, "A Simple 18-Pulse Star Rectifier Using Two Passive Auxiliary Circuits at DC Link," IEEE Trans. Power Electron., vol. 37, no. 5, pp. 5583-5593, May. 2022.
[23] R. Abdollahi, G. B. Gharehpetian, A. Anvari-Moghaddam, F. Blaabjerg, "A 40-Pulse Autotransformer Rectifier Based on New Pulse Multiplication Circuit for Aviation Application," IEEE Trans. Ind. Electron., Early Access, DOI: 10.1109/TIE.2022.3227229.
[24] R. Abdollahi, G. B. Gharehpetian, and M. Davari "A Novel More Electric Aircraft Power System Rectifier Based on a Low-Rating Autotransformer", IEEE Trans. Transp. Electrif., vol. 12, no. 4, pp. 330-343, 2022.
[25] R. Abdollahi, G. B Gharehpetian, A. Anvari-Moghaddam, and F. Blaabjerg, "Pulse Tripling Circuit and Twelve Pulse Rectifier Combination for Sinusoidal Input Current," IEEE Access, vol. 9, pp. 103588-103599, 2021.
[26] Colonel Wm. T. McLyman, "Transformer and Inductor Design Handbook," Taylor & Francis Group, LCC, 5-7, 2011.

Rohollah Abdollahi is currently working toward the Ph.D. degree with the Shahid Beheshti University, Tehran, Iran. He received the M.Sc. degree in electrical engineering (power electronics and electrical machines) from Iran University of Science and Technology, Tehran, Iran, in 2011. He is a faculty member of the Department of Electrical Engineering, Technical and Vocational University (TVU), Tehran, Iran. He is the author of more than 80 journal article papers. He has been granted two U.S. patents and 13 Iran patents. His fields of interest include power electronics, power quality, and power systems.

Alireza Reisi received the Ph.D. degree in electrical engineering from Bu-Ali Sina University, Hamedan, Iran, in 2017. He is an Assistant Professor in the Department of Electrical Engineering, Technical and Vocational University (TVU), Tehran, Iran. He publishes, teaches, and consults widely in most aspects of power system, renewable energy, and power electronic.

International Journal Of
Industrial Electronics Control and Optimization
Print ISSN: 3517-2645
Online ISSN: 3568-2645
Homepage: https://ieco.usb.ac.ir/

A Compact Antenna with Dual Polarization for Mobile and Wireless Communication

Fatemeh Kazemi

Faculty of Engineering, University of Zabol, Zabol, Iran.
Corresponding author's email: Fkazemi@uoz.ac.ir

Article Info

Article type:
Research Article

Article history:
Received: 2022-Nov-03
Received in revised form: 2023-Feb-20
Accepted: 2023-Mar-12
Published online: 2023-Mar-29

Keywords:
Small Antenna,
Parasitic Elements,
Circular Polarization,
Wireless Communication Systems.

ABSTRACT

In this paper, a dual-polarized antenna fed by CPW is presented. The proposed includes a conductor on the radiator and has defected ground, so it has been achieved as an omnidirectional antenna which makes it a low loss, and a simple antenna which is appropriate for a wireless communication system. By imposing the different circumstances of U-shape elements on the ground, the features of antennas have been improved. The scattering characteristic of the antenna are less than -20 dB with high impedance matching at 2.2GHz, 4.8GHz, and 6.6GHz. Also, the antenna covers 400 MHz bandwidth from 2 GHz to 2.4 GHz, 500 MHz bandwidth from 4.6 GHz to 5.1 GHz, and 1.3 GHz bandwidth from 5.7 GHz to 7 GHz, respectively. In addition, the maximum gain of the antenna is almost 10 dB. The simple and compact antenna with an overall size of 25x20mm^2 is designed on an FR-4 substrate with 0.8 mm thickness. On the one hand, the structure is fabricated and tested. The results of the antenna have shown that the measured results agree with the simulated results; The performance of the antenna with CPW-fed, consisting of compact size, circular polarization, and suitable gain at resonance frequencies, make it a suitable choice for the communication system and the portable device.

I. Introduction

Wireless communication systems are highly diverse with different applications [1]. Although electronic and telecommunication structures continue to downsize with the development of communication technologies and instruments, the previous capabilities need to be preserved in the new structures and methods proposed by scientists. Responsible for transmitting and receiving information, wireless communication systems are confronted with challenges such as noise, interference and etc. [2-3].

As one of the key elements of wireless communications, antennas have continued their development with technological advancements over time [4]. The physical size and configuration of an antenna are initially dependent on its operating frequency. Old antennas used to be very large and thus unsuitable for deployment in portable wireless circuits [5]. The next generations of antennas were able to solve most of the previous problems in this field. Microstrip antennas, slot antennas, and integrated-circuit antennas were invented to integrate with other portable circuits such as printed circuit boards (PCBs), or semiconductor chips. In addition to their other advantages, the use of integrated circuit technology in the fabrication of antennas has high precision in manufacturing, which cannot be achieved with traditional methods [6-7].

To transfer the highest power from the input to the radiating structure, an appropriate transmission and power line is required, for instance, a microstrip transmission line, parallel

transmission line, and coaxial transmission line. In addition to these lines, delta matching helped perfect the integration of transmission lines with radiating structures. Ground and radiation structure are two important parts of radio systems. The full ground structure in the previous generation of antennas had a smaller bandwidth. However, a defected ground solved these problems and allowed antennas to cover multiple bands simultaneously [8]. The radiation structures have also experienced undergone significant changes and modifications in their shapes such as Circular, square, and star structures as well as the met material and integrated structures with multiple layers. Generally, the miniaturization of the configuration changes the electromagnetic characteristics, including the antenna gain and bandwidth [9].

An antennas with multi-purpose operation and multi-band coverage is now required more than often. Most communication systems prefer to use a single radiating element with multiple bands and purposes, leading to reduces size and weight. These antennas have numerous interesting applications. New antennas are multi-purpose and adaptable, so that with the smallest change in their dimentions, their operating frequency changes. Thanks to the switching mechanism, in adaptive antennas, the operating frequency, phase, and radiation pattern can be altered [10-11]. The gain and polarization of the antenna is known as min parameters of antenna. the higher the gain, the stronger the antenna, so the antenna will produce the radio frequency field strongly. The circular polarization antenna transmits waves that rotate continuously between horizontal and vertical planes to provide more flexibility. However, because the energy is split between the two planes, the readout range of a circularly polarized antenna is shorter compared to a linear polarized antenna with the similar gain[12-14]. A metamaterial fractal antenna with the size of 51.9×51.9 mm^2 has been designed on the FR-4 substrate in [4] fed by a CPW line on the top layer. It has narrow bandwidth at all bands and obtains the peak of gain 9.5 dBi [7]. Several antennas use slots and CPW feed lines to improve characters; for example, [8], introduces a wide circular polarized antenna with a peak gain of 3.5 dB at low frequency and almost 6 dB at high; moreover, in [10], it is designed for medical applications. For using DC voltage and circuit, these antennas become bulky or utilize multilayer substrate [13-14]. There are several 1-D and wearable structures for antenna polarization and gain enhancement [15]. Circular polarization is one of the main factors to consider in antenna design. [16-17].

Here, an antenna with a low profile and plain structure is provided at 2.2 GHz, 4.8 GHz, and 6.6 GHz, which is useful for mobile and wireless systems. The circularly polarized antenna consists of a simple defected ground structure with one U-shaped parasitic element and rectangle element on both sides of the feed line. This structure with a total size of 25×20mm^2 is simulated and printed on a low-cost efficient Fr-4 substrate with 0.8 mm thickness. The proposed antenna has been fabricated and tested. Using the U-shaped parasitic element has led to achieving circular polarization in the first and third band and liner polarization in the second band; in addition, using CPW feed line and defected ground structure has offered more than 50% size reduction of the structure compared to other similar ones. High gain antenna with dual polarization in the desired band provides the suitable structure for WLAN, Wi-Fi, and UMTS (Universal Mobile Telecommunication Service). The antenna has been optimized using a full-wave simulator (HFSS). It helps to analyze the structure to show the influence of each parameter efficiently. basic structure, according to desired antenna and normalized formulations have been obtained and extracted.

II. Antenna Geometry and Design Procedure

Size go hand in hand with electromagnetic features; therefore, nowadays, the structure should be physically developed. Antenna is the essential case of telecommunication systems that must be made smaller. Moreover, due to its integration into integrated structures, size reduction has negative effects on antenna characteristics. By introducing new methods of feeding as well as new antenna such as microstrip, to some extent, the situation gets improved [18-20].

Micro stripe antenna consists of ground conductor and the feed line connected to the patch, which is resonant at selective frequencies. Among the types of feed lines and antenna structures mentioned above, Coplanar waveguides (CPW) feed and rectangular-shaped patches are chosen for wireless communication systems due to their inherent wide bandwidth and better performance. CPWs and taper sector have also played a vital role in this research area. CPW feed line constructed on straightforward taper. The tapered segment attaches a 50Ω CPW signal line to the antenna. The taper is utilized to gain well impedance matching.

To reach maximum power from the feed to the patch, the antenna requires a transmission line and delta match which provides the best way for. The design of the antenna relies on the equations in [1-2]. The first and most important factor of the antenna is its bandwidth and resonance frequencies. Therefore, the S-Parameter curve helps to identify them. Additionally, antennas that work well must have matching frequencies. Firstly, the base antenna is designed according to Fig 1. S-parameters in Fig 3 show that the dual-band liner polarized antenna is achieved.

For further achievement and improving features, the process of designing and the diverse type of antenna is investigated in Fig 2. According to Fig 3, from 1 GHz to 8 GHz, the proposed antenna has covered several selective frequencies. The first one is at 2.2GHz and the other ones are at 4.8 and 6.6 GHz. In addition, it has 400 MHz, 500GMHz, and 1.3GHz bandwidth, respectively.

Based on Fig 3, it is shown that the antenna has reconfigurable features with varying U-shaped parasitic elements on the ground. Initially, the antenna has been a dual-band. After inserting that element, it has turned into a third band with

suitable features for wireless communication systems. The parameters of the antenna are given in Table I.

TABLE I
PARAMETERS OF THE ANTENNA

Parameters		Parameters		Parameters	
W	25mm	g	15mm	g3	0.775mm
L	20mm	g1	0.125mm	w1	1.55mm
L1	16mm	g2	0.275mm	w2	3.75mm
w4	4.75mm	w5	4mm	w3	5mm

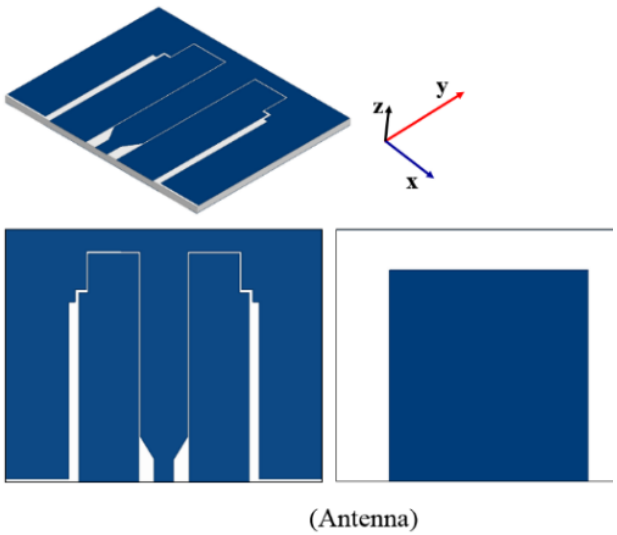

Fig.1. The structure of base antenna

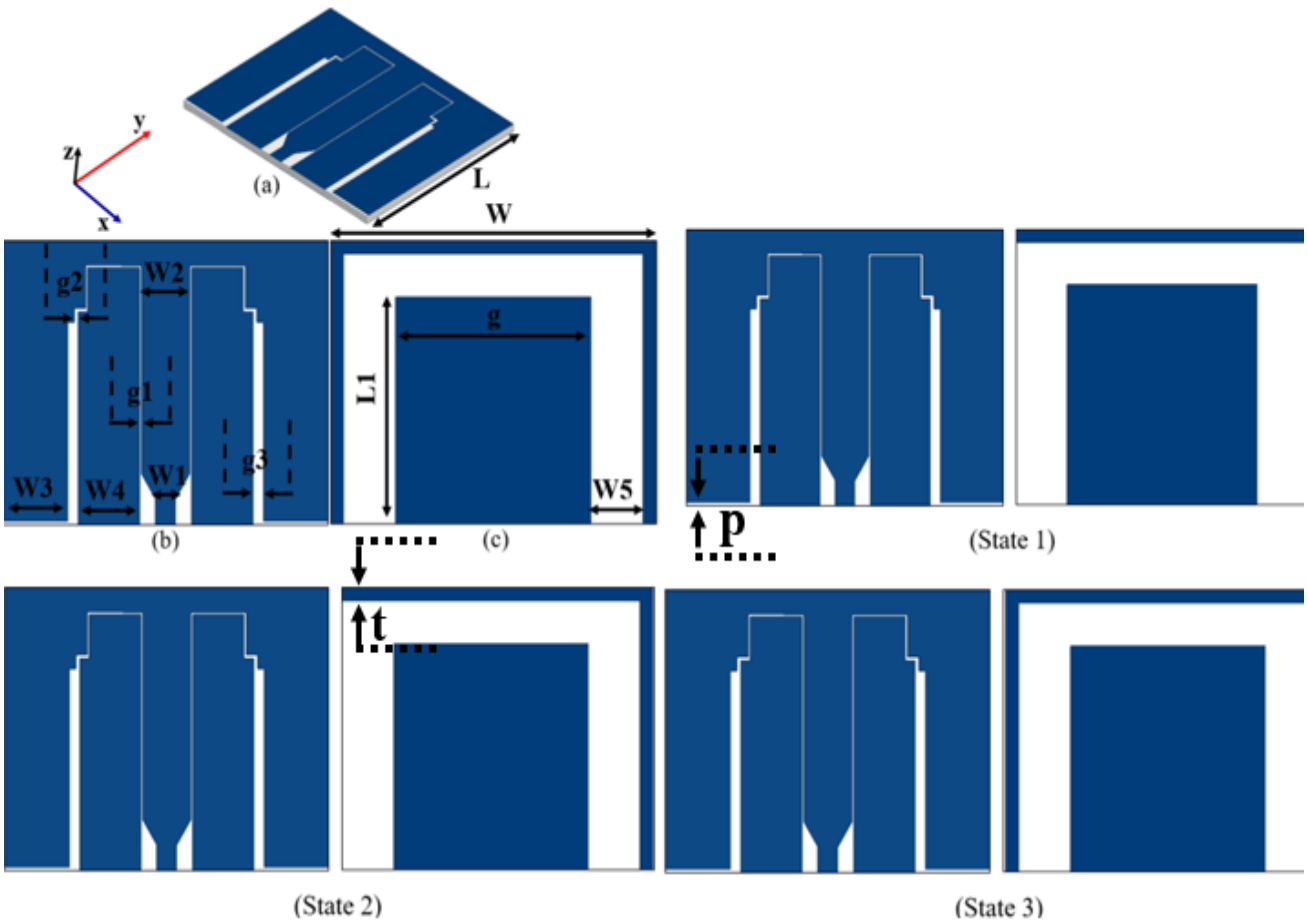

Fig.2. 3-D schematic and antenna evolutionary process.

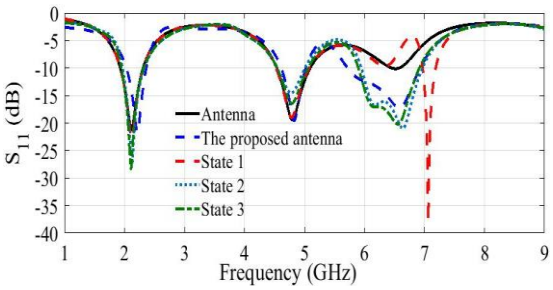

Fig.3. Simulated S-parameter of all state and the proposed antenna.

III. Surface Current Distribution

The surface current distribution is the best way to understand and depict the antenna patch radiation mechanism at the main frequencies shown in Figure 4-6 at the resonance frequencies of 2.2 GHz, 4.8GHz, and 6.6GHz, respectively. Apparently, the edge of the structure achieves the most current. From Fig. 3-5, it is clear that mainly current spread on the bottom part of the patch which makes resonance around 2.2 GHz. The resonance at around 4.8 GHz and 6.6 GHz is caused by the current distributed over the edge rectangular elements on both sides of the feed line as shown in Figure 4-6, respectively.

To investigate the polarization of the proposed antenna, the surface current distribution for 2.2 and 6.6 GHz frequencies in different phases of 0, 90, 180 and 270 degrees is shown in Figure 4-6. The rectangular elements on the both side of antenna produce circular polarization for antenna at f=2.2GHz. Similarly, the main part of the antenna in generating the 6.6 frequency is located around the edge and top of the patch. The current vector rotates counterclockwise, causing the left-handed circular polarization (LHCP) radiation to be in the θ = 0° direction.

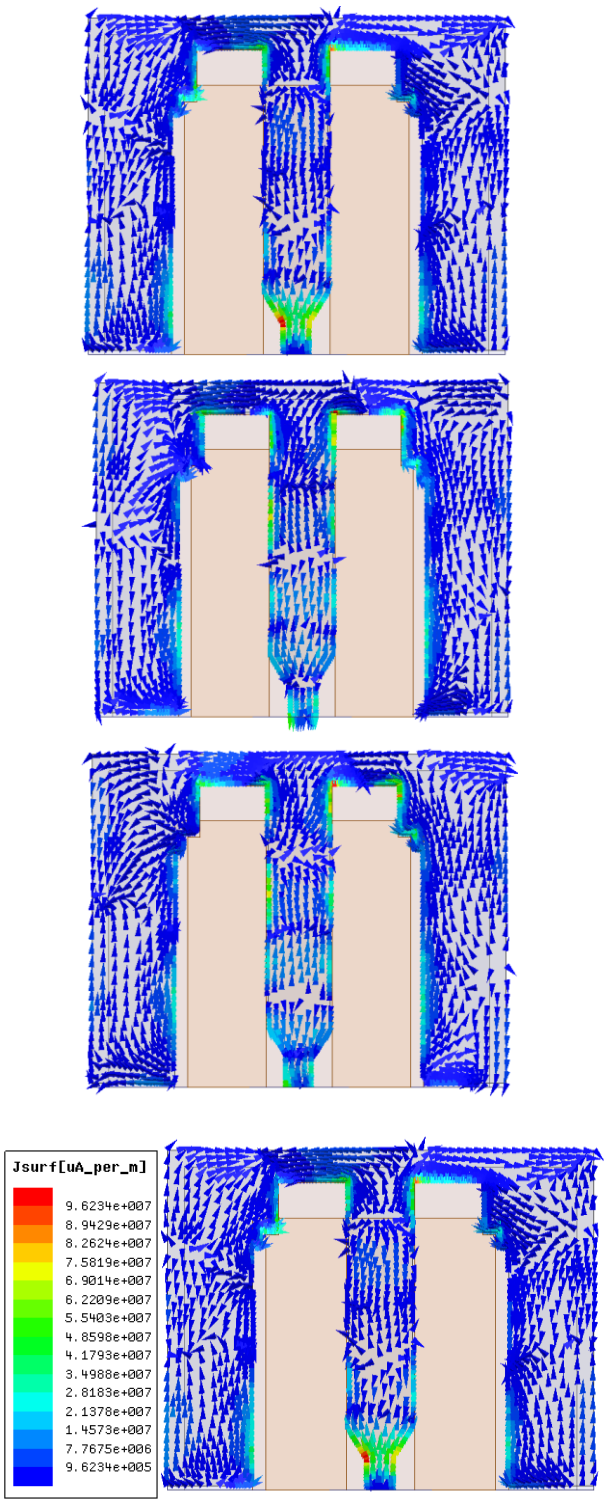

Fig.4. Simulated of surface current distributions at f=2.2GHz.

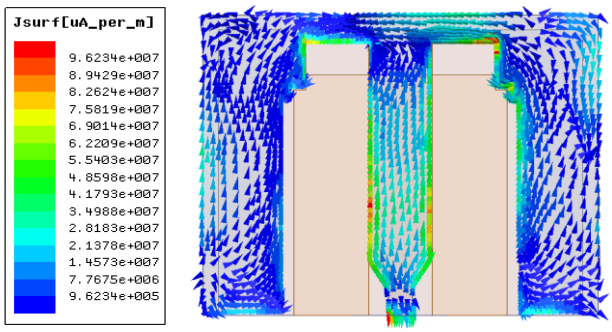

Fig. 5. Simulated of surface current distributions at 4.8 GHz.

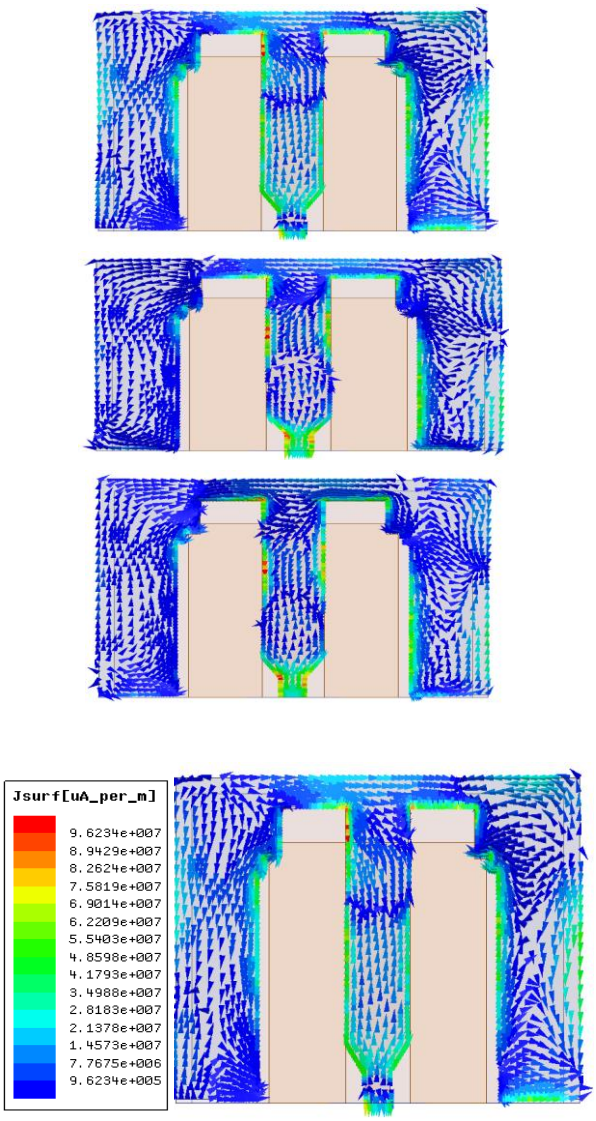

Fig. 6. Simulated of surface current distributions at 6.6 GHz.

IV. Parametric Study

In this section, in order to have a better comprehension of the results, parametric study on some important parameters in antenna design has been investigated. The main key is to obtain a good impedance matching and control it. Since the U-shaped element is the main part of the antenna, it can help control the antenna. Especially at the third resonance frequency, the change of P and it causes a minor variation in impedance matching and frequency shift. A parametric study has been investigated in HFSS software for important factors with several values. As depicted in Fig 7(a), for P=1 to 4 mm low impedance matching and bandwidth has been changed preciously. Moreover, the third band have been getting better compared to the past manner. Another parametric study is the width of the U-shaped parasitic element at the ground plane location, which shows that a small difference of 0.5 mm changes the resonance frequency and decreases the impedance matching as well as the third resonance frequency, according to Fig. 7(b). In order to clarify the performance of circular polarization of antenna, axial ratio can be helpful with presenting date. Therefore, axial ratio of antenna is obtained from 1GHz to 9GHz to illustrate behavior of antenna based on changing the amount of W4. In Fig 7(c), W4 values have been varied from 4.75mm to 5.5mm to show that stair-shape radiator is capable of creating circular polarization. The axial ratio is obtained 400 MHz and 1.3GHz bandwidth, from 2 GHz to 2.4 GHz and from 5.7 GHz to 7 GHz, respectively.

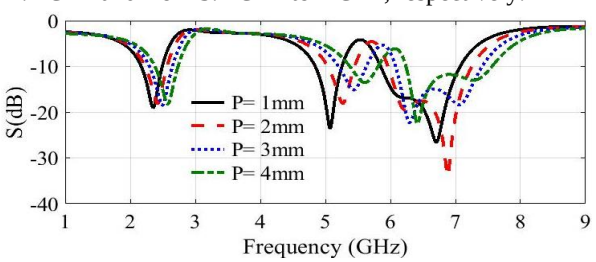

(a)

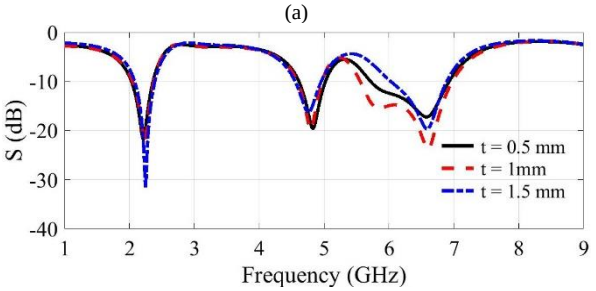

(b)

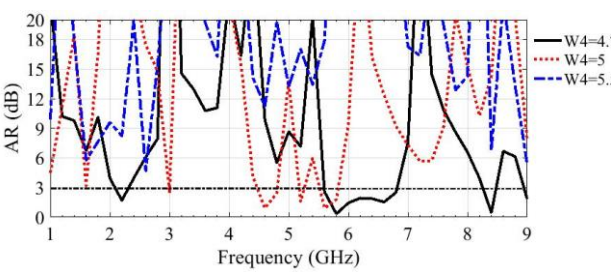

(c)

Fig. 7. (a) S-parameters for different values of P, (b) Simulated reflection coefficients for three values of t, and (c) Simulated axial ratio for three different values of W4.

V. Fabricated Antenna

pou E8363C illustrated as shown in Fig 8(a). Also, the measured and simulated results are presented in Fig 8(b). After making and testing the antenna, the test results are similar and in good agreement with the simulated results. As FR4 substrate provides suitable results in simulation process as well as an easy accessibility and lower cost in market, this material is selected to be used. Fortunately, the experimental results confirm the simulated ones to a high extent which ensures suitability of this material. In fact, a trade-off between cost, availability, and dielectric loss is performed which ends in selection of FR4 substrate. The proposed antenna works well in the desired bands of WLAN: The 802.11 working in five frequency ranges: 2.4 GHz, 4.9 GHz, 5 GHz, and 5.9 GHz bands. Each range is divided into a multitude of channels. Similarities can result from the quality of the substrate and the way the antenna is soldered, and the lack of the correct caliber of the measuring device.

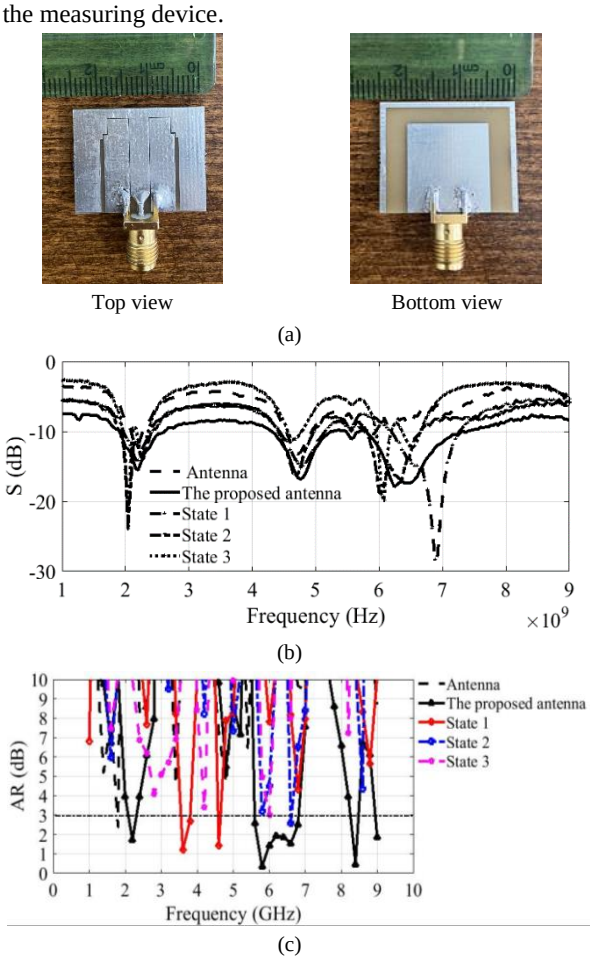

Fig 8. (a) Fabricated structure top and bottom view, (b) Measured and simulated reflection coefficient, (c) simulated axial ratio for the proposed antenna and other state of antenna.

Although, the tested results explicitly testify that both results are almost the same, but fabrication and measurement setup tolerances cannot be ignored. In the proposed antenna, a bandwidth of 400 MHz from 2 GHz to 2.4 GHz, 500 MHz from 4.6 GHz to 5.1 GHz, and 1.3 GHz from 5.7 GHz to 7 GHz is obtained with good impedance matching. On the other hand, based on Fig 8(c), the simulation results of axial ratio show that circular polarization has been obtained at the desired frequencies. The antenna has circular polarization at 2.2 GHz and 6.6GHz with 200MHz and around 1GHz bandwidth, respectively.

VI. Radiation Pattern

Another key feature of an antenna is its radiation pattern as it indicates the direction and power of the transmitting wave. For communication systems, omnidirectional patterns are the best choice. Actually, in the omnidirectional manner, the antenna radiates around itself with approximately the same power, which is widely adopted by wireless communication and portable systems [21-23]. Based on Fig. 9, the simulated and tested results show that the radiation pattern of the proposed antenna is omnidirectional at 2.2 GHz, 4.8 GHz, and 6.6 GHz on XOZ plane and YOZ plane.

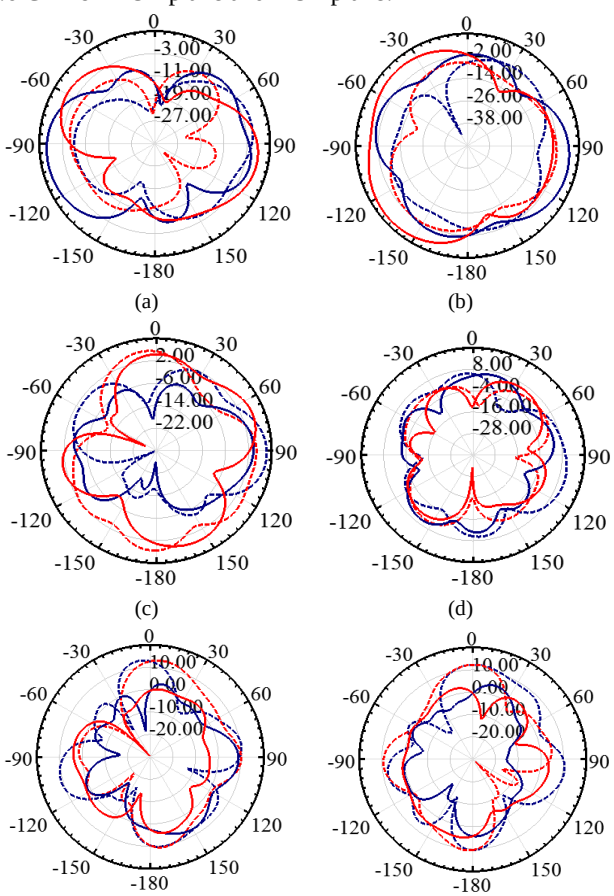

Fig.9. Measured and Simulated radiation patterns (a-b) at f=2.2GHz, (c-d) f=4.8GHz, and (e-f) f=6.6GHz. (Solid line is XOZ and dashed line is YOZ) (left-side and right-side results show LHCP and RHCP patterns, respectively), (red line belongs to measured results and blue one to simulated results).

VII. Comparison

Table II investigates the applicability and advantages of design in terms of size, gain, and polarization. Comparing the proposed antenna with the previous papers, simple and compact antenna fed by CPW and using a U-shaped element on the ground can cover better features, and higher gain at the same time.

TABLE II

COMPARISON OF THE PROPOSED ANTENNA AND SOME SIMILAR DESIGNS IN THE LITERATURE

Reference	Size (mm^3)	Gain (dB)	f (GHz)	Polarization
[2]	22×24×1.59	2.4 and 3.5	2.48 and 3.49	Liner
[3]	37.8×40.4×1.6	1.9 and 1.2	2.4 and 5.2	Circular
[4]	$0.42\lambda \times 0.8\ \lambda$	6.84	5.8	Circular
[5]	30×20×0.8	2	2.9	Liner
[6]	28 × 26×1.6	2.9,4.13, and 5.8	2.4,4.4, and 7.4	Liner
[7]	35×23	2	2.1 and 4.5	Circular
[23]	$0.58\lambda \times 0.58\ \lambda$	7.26	2.4	Circular
This work	25×20×0.8	3,6,and 10	2.2,4.8, and 6.6	Circular, liner

VIII. Conclusion

A third-band antenna with dual-polarized for wireless, Bluetooth application and mobile service has been simulated and tested. Bandwidth of 400 MHz at resonance frequency 2.2 GHz, 500 MHz at resonance frequency 4.8 GHz, and 1.3GHz at resonance frequency 6.6GHz is obtained, respectively. Also, the antenna has circular polarization at 2.2 GHz and 6.6GHz and linear polarization at 4.8GHz. The compact antenna with $25\times20mm^2$ sizes is fabricated and measured on an FR4 substrate with 0.8 mm thickness. A high gain of almost 7.5 dB and also circular polarization at two resonance frequencies have been earned by the simple structure. Suitable physical and electromagnetic properties are achieved in the mentioned frequency bands.

REFERENCES

[1] Kumar A, Sankhla V, Deegwal JK, Kumar A. An offset CPW-fed triple-band circularly polarized printed antenna for multiband wireless applications. AEU-International Journal of Electronics and Communications. 86:133-41,2018.

[2] Naik KK. Asymmetric CPW-fed SRR patch antenna for WLAN/WiMAX applications. AEU-International Journal of Electronics and Communications. 93:103-8, 2018.

[3] Kumar P, Dwari S, Saini RK, Mandal MK. Dual-band dual-sense polarization reconfigurable circularly polarized antenna. IEEE Antennas and Wireless Propagation Letters. 18(1):64-8,2018.

[4] Yang L, Yang L, Zhu Y, Yoshitomi K, Kanaya H. Polarization reconfigurable slot antenna for 5.8 GHz wireless applications. AEU-International Journal of Electronics and Communications. 101:27-32,2019.

[5] Fang X, Wen G, Inserra D, Huang Y, Li J. Compact wideband CPW-fed meandered-slot antenna with slotted Y-shaped central element for Wi-Fi, WiMAX, and 5G applications. IEEE Transactions on Antennas and Propagation. 66(12):7395-9,2018.

[6] Saadh AM, Poonkuzhali R. A compact CPW fed multiband antenna for WLAN/INSAT/WPAN applications. AEU-International Journal of Electronics and Communications.109:128-35,2019.

[7] Choudhary DK, Chaudhary RK. Compact filtering antenna using asymmetric CPW-fed based CRLH structure. AEU-International Journal of Electronics and Communications. 126:153462, 2020.

[8] Das S, Gupta A, Sahu S. Metamaterial based fractal-ground loaded frequency-reconfigurable monopole-antenna with gain-bandwidth enhancement. AEU-International Journal of Electronics and Communications.132:153593, 2021.

[9] A. Kumar, M. M. Sharma, and R. P. Yadav, "Dual wideband circular polarized CPW-fed strip and slots loaded compact square slot antenna for wireless and satellite applications," AEU-International Journal of Electronics and Communications, vol. 108, pp. 181-188, 2019.

[10] A. Y. Ashyap et al., "Highly efficient wearable CPW antenna enabled by EBG-FSS structure for medical body area network applications," IEEE Access, vol. 6, pp. 77529-77541, 2018.

[11] A. Goswami, A. Bhattacharya, and B. Dasgupta, "Reconfigurable hexagon shaped printed antenna for cognitive radio application," International Journal of RF and Microwave Computer-Aided Engineering, vol. 31, no. 2, p. e22514, 2021.

[12] J. Wang, J. Zhao, Y. Cheng, H. Luo, and F. Chen, "Dual-band high-gain microstrip antenna with a reflective focusing metasurface for linear and circular polarizations," AEU-International Journal of Electronics and Communications, vol. 157, p. 154413, 2022.

[13] W. Sun, Y. Li, Z. Zhang, and P.-Y. Chen, "Low-profile and wideband microstrip antenna using quasi-periodic aperture and slot-to-CPW transition," IEEE Transactions on Antennas and Propagation, vol. 67, no. 1, pp. 632-637, 2018.

[14] Z. Li, X. Zhu, and C. Yin, "CPW-fed ultra-wideband slot antenna with broadband dual circular polarization," AEU-International Journal of Electronics and Communications, vol. 98, pp. 191-198, 2019.

[15] S. M. H. Varkiani and M. Afsahi, "Compact and ultra-wideband CPW-fed square slot antenna for wearable applications," AEU-International Journal of Electronics and Communications, vol. 106, pp. 108-115, 2019.

[16] P. Chaudhary and A. Kumar, "Compact ultra-wideband circularly polarized CPW-fed monopole antenna," AEU-International Journal of Electronics and Communications, vol. 107, pp. 137-145, 2019.

[17] K. Pedram, M. Karamirad, and N. Pouyanfar, "Evolution and Move toward Fifth-Generation Antenna," in The Fifth Generation (5G) of Wireless Communication: IntechOpen, 2018.

[18] A. Kishk, The Fifth Generation (5G) of Wireless Communication. 2019.

[19] X. Jin, S. Liu, Y. Yang, and Y. Zhou, "A Frequency-Reconfigurable Planar Slot Antenna Using S-PIN Diode,"

IEEE Antennas and Wireless Propagation Letters, 2022.
[20] K. Ramahatla, M. Mosalaosi, A. Yahya, and B. Basutli, "Multi-Band Reconfigurable Antennas For 5G Wireless and CubeSat Applications: A Review," IEEE Access, 2022.
[21] R. Bhakkiyalakshmi and M. Vasanthi, "Novel Four-port Reconfigurable Filtering MIMO Antenna for Multi-standard Automotive Communications," AEU-International Journal of Electronics and Communications, p. 154108, 2022.
[22] Tang, H., et al. "Compact triple-band circularly polarized monopole antenna for WLAN and WiMAX applications." Microwave and Optical Technology Letters 59(8): 1901-1908,2017.
[23] S. Lee and Y. Sung, "Simple polarization-reconfigurable antenna with T-shaped feed," IEEE Antennas and Wireless Propagation Letters, vol. 15, pp. 114-117, 2015.

Fatemeh Kazemi was born in Zahedan, Iran. She received B.Sc. and M.sc. degrees in Electrical Engineering from University of Sistan and Baluchestan in 2005 and 2010 respectively and Ph.D. degree in communication system from the University of Sistan and Baluchestan. She is currently an assistant professor at the University of Zabol. Her research concerns include Microwave Imaging, analysis and design of near-field probes, antenna propagation, and antenna design for mobile and wireless communication systems.